Laser Micromachining of Active and Passive Photonic Integrated Circuits

by

Seong-Ho Cho

Submitted to the Department of Electrical Engineering and Computer Science
in partial fulfillment of the requirements for the degree of

Doctor of Philosophy in Electrical Engineering

at the

MASSACHUSETTS INSTITUTE OF TECHNOLOGY

[February 2004]
December 2003

©2003 Massachusetts Institute of Technology
All Rights Reserved.

Author . . . .
Department of Electrical Engineering and Computer Science
December, 2003

Certified by . . . .
Rajeev J. Ram
Professor, Electrical Engineering
Thesis supervisor

Accepted by . . . .
Arthur C. Smith
Chairman, Department Committee on Graduate Students

MASSACHUSETTS INSTITUTE
OF TECHNOLOGY
APR 1 5 2004
LIBRARIES

BARKER

Laser Micromachining of Active and Passive Photonic Integrated Circuits

by

Seong-Ho Cho

Submitted to the Department of Electrical Engineering and Computer Science
on December, 2003, in partial fulfillment of the requirements for the degree of
Doctor of Philosophy in Electrical Engineering

ABSTRACT

This thesis describes the development of advanced laser resonators and applications of laser-induced micromachining for photonic circuit fabrication. Two major advantages of laser-induced micromachining are direct patterning and writing on large areas of substrates at high speed following the exposure of laser light, without using complicated photomask steps. For passive photonic devices fabrication, a novel femtosecond laser with unprecedented low repetition rates of 4 MHz is demonstrated to generate high intensity pulses, as high as 1.25 MW with 100 nJ pulse energies and 80 fs pulse durations directly from this laser resonator, without using any active devices or amplifiers. These high intensity pulses are applied to transparent glass materials to demonstrate micromachining of waveguides, gratings, couplers, and three dimensional waveguides and their beam couplings.

Active and passive semiconductor devices can be monolithically integrated by employing high energy laser pulses to locally disorder quantum well regions. The 45 nm bandgap shifts at 1.55 μm with a standard Q-switched Nd:YAG laser at 535 nm are realized. Finally, unidirectional semiconductor ring lasers for high-density integration are developed as a potential application to photonic integrated circuits. Hybrid semiconductor S-crossover and retro-reflected ring lasers, as prototypes for unidirectional operation, are built and result in up to 21.5 dB and 24.5 dB of counter-mode suppression ratio, respectively, which is in good agreement with theoretical predictions.

Thesis Supervisor: Rajeev J. Ram
Title: Professor

Acknowledgments

I am deeply indebted to Professor Rajeev Ram for the amazing caliber of his mind, and for his consistent support and tutelage during my PhD work at M.I.T. I always enjoyed his timely mentorship, unique insight, and ceaseless enthusiasm, all of which have inspired and challenged me. His magnetic and sparkling character always cheers me up. It is particularly memorable to me that we once had a whole evening conversing about philosophy as well as our research.

I am very grateful to Professor James Fujimoto for his invaluable guidance in ultrafast lasers during my first years in the Ultrafast Optics Group. I respect his remarkable engineering sense, incredible passion for and continuous motivation in scientific research. I am also extremely grateful to the late Professor Hermann Haus for encouraging my pursuit of theoretical soliton theories and integrated optics by his virtuosity in science. I was fortunate to have been able to work with him and learn from his intuition, and wish him heavenly bliss. I am also grateful to Professor Franz Kärtner for his contribution to my work on various occasions and for serving as a thesis reader. It was my delight to participate in a breakthrough experiment in which we achieved two-cycle optical pulses, the shortest in the world. I am greatly thankful to Professor Hank Smith who readily served as a thesis reader and posed fascinating questions. To discuss scientific issues with Professor Erich Ippen was terrifically helpful, thanks to his insights into physical thinking, and as were stimulating discussions with Professor Leslie Kolodziejski.

There are precious friends who helped shape my experience and finish this thesis work: to Uwe Morgner who endeavored for two-cycle femtosecond lasers with Kant-wise punctuality, scientific zeal, and astonishing programming skills; to Wayne Knox, Lucent Technologies, whose saturable Bragg reflector was invaluable for building up low repetition rate lasers; to Richard Boggy, Spectra-physics, for the courtesy of his high reflectance mirrors; to Yu Han, the president of CVI, for the generous gift of his multipass cavity mirrors; to Daniel Byun, postdoctoral fellow in Chemistry, for allowing me to use his Nd:YAG lasers and lending me support in the process; to Ryan Thom, George Harrison Spectroscopy Laboratory, who initially helped my intermixing experiment; to Ryan Williams and Juliet Gopinath for their help in teaching me how to measure low temperature photoluminescence; to Jürgen Michel, Materials Processing Center, for training me in the use of low temperature scanning electron

microscopy and catholuminescence; and to Solomin Assefa, the Nanostructure Laboratory, who grew a sputtered Silicon oxide coating.

I give my gratitude to all my friends in the Physical Optics and Electronics Group, the Ultrafast Optics Group, and the Microsystems Technology Laboratory, for years of help and camaraderie: to Farhan Rana for a key comment on the coupled rate equation model; to Harry Lee for his critical comments and questions about my experiment; to Xiaoyun Guo for advice on semiconductor laser processing; to Kevin Pipe for helpful discussions especially at conference trips; to Woo-Hyung Choi for broad mentoring; to Matthew Abraham for his lovely smile and warm heart; to Peter Mayer, Tom Liptay, Tauhid Zaman, Dietrich Lueerssen, Andrew Kowalevicz, Hue Song, and Kurt Broderick. I would like to thank members of the First Korean Church in Cambridge for offering prayer and giving me so much joy.

I would like to give heartfelt thanks to Soonie for her consistent commitment and support as a wife as well as a Christian fellow in spite of being extremely busy on her own studies. Finally, I would like to dedicate this thesis to my parents, who have been a beacon in my life, patiently supported me and infinitely loved me. It is a glory of God who led me to this prestigious institution and allowed me to find a truth in life, which is summarized in His Scripture: "the mystery of God, Christ, in whom are hidden all the treasures of wisdom and knowledge [Colossians 2:3]."

Contents

Chapter 1. Motivation and Introduction **19**
1.1 Motivation and Objective 19
1.2 Advent of Photonic Integrated Circuits 20
1.3 Novel Ultrafast Laser Resonator for Passive Waveguide Micromachining . . 21
1.4 Pulsed Laser Absorption Induced Disordering for Active Device Integration 23
1.5 Microphotonic Ring Laser Resonator for Photonic Integrated Circuit 26
1.6 Overview of Chapters 27

Chapter 2. Novel High Intensity Ultrafast Laser Resonator **29**
2.1 Introduction 29
2.2 Extended Cavity and Novel Laser Design 31
2.3 15 MHz, High Intensity KLM Laser with Multiple Pass Cavity 33
2.4 7 MHz, High Intensity KLM Laser with Multiple Pass Cavity 36
2.5 4 MHz, High Intensity KLM Laser with Multiple Pass Cavity 40
2.6 Analytic Theory of Quintic Complex Master Equation 45
2.7 Conclusion 50

Chapter 3. Fabrication using High Intensity Ultrafast Lasers **53**
3.1 Introduction 53
3.2 Laser Induced Ablation Mechanisms 54
  3.2.1 Laser Induced Excitation and Relaxation 54
  3.2.2 Determination of Ablation Threshold 57
  3.2.3 Microexplosion in Transparent Dielectrics 61
3.3 Experimental Setup 63
3.4 Fabrication of Waveguides and Characterization 64
3.5 Fabrication of Gratings 67
3.6 Fabrication of Coupled Mode Devices 68
  3.6.1 Y-coupler 68
  3.6.2 X-coupler 69
3.7 Fabrication of Three Dimensional Waveguides 70
3.8 Conclusion 72

Chapter 4. Pulsed Laser Absorption Induced Quantum Well Intermixing . . 75
4.1 Introduction 75
4.2 Overview of Quantum Well Intermixing 76
  4.2.1 Advantages 77
  4.2.2 Limitations 78
  4.2.3 Solutions 78
4.3 Generic Mechanism of Quantum Well Intermixing 78
4.4 Pulsed Laser Absorption Induced Disordering 82
  4.4.1 Method of Pulsed Laser Absorption Induced Disordering 82
  4.4.2 Review of Previous Work 83
4.5 Experiment of Pulse Laser Absorption Induced Disordering 84
  4.5.1 Experimental Setup 84
  4.5.2 Photoluminescence Measurement 87
  4.5.3 Analysis of Photoluminescence Measurement 87
  4.5.4 Surface morphology 92
  4.5.5 Experimental Conclusions 92
4.6 Theory for Pulsed Laser Absorption Induced Disordering 94
  4.6.1 Overview of Theoretical Modeling 94
  4.6.2 Theoretical Modeling of Laser Induced Decomposition 96
4.7 Discussion 103

Chapter 5. Unidirectional Semiconductor Ring Lasers 105
5.1 Unidirectional Semiconductor Ring Lasers for High Density Circuit Integration 105
  5.1.1 Introduction 105
5.2 Theory of Integrated Unidirectional Ring Lasers 108
  5.2.1 Resonance Properties of Unidirectional Ring Lasers 108
  5.2.2 Coupled Rate Equations for Unidirectional Ring Lasers 111
  5.2.3 Coupled Equations for S-crossover Ring Lasers 113
  5.2.4 Coupled Equations for Retro-reflected Ring Lasers 115
5.3 Macroscopic Unidirectional Hybrid Ring Lasers 116
  5.3.1 Gain and Internal Parameter Measurement of SOA 116
  5.3.2 S-crossover Hybrid Ring Lasers 119
  5.3.3 Retro-reflected Hybrid Ring Lasers 124
5.4 Conclusion 128

Chapter 6. Conclusions 131

Appendix A. Appendix: Chapter 2 . . . . **137**
A.1 Quintic Complex Master Equation for Nonlinear Solitary Pulses 137

Appendix B. Appendix: Chapter 5 . . . . **139**
B.1 Scattering Matrix for Asymmetric Y-Branch 139

Appendix C. Appendix: Chapter 5 . . . . **145**
C.1 Derivation of Resonance Filter Properties using Diagrammatic Approach . . 145
  C.1.1 S-crossover ring resonator 145
  C.1.2 Retro-reflected ring resonator 147

Bibliography **149**

List of Figures

Figure 1.1 Full optoelectronic integration is used to create monolithic systems. Schematic view of multi-quantum well, electro-absorption modulator integrated DFB laser with semiconductor insulating buried heterostructures [4]. 20

Figure 1.2 Femtosecond micromachining has achieved to create (a) X-coupler [13] and (b) a three dimensional helical waveguide [17], within a glass substrate using localized changes of refractive index. 22

Figure 1.3 Schematic diagram of quantum well intermixing, SCH, separate confinement heterostructure: (a) the bandgap before intermixing, E_g and band structure (solid); (b) the bandgap after intermixing E_g' and band structure (dot). . . 24

Figure 1.4 Ring lasers that have different characteristics are densely integrated in two dimensions, and output laser beams are combined with a start coupler . . . 26

Figure 2.1 Ti:Sapphire laser schematic with a pair of multiple pass cavity mirrors: R_1, R_2, 10 cm radius of curvature mirrors (Spectra-physics); R_3, R_4, 2" diameter MPC mirrors with 2 m radius of curvature (CVI); L, 12.5 cm focal length pump beam focusing lens; OC, 10 % 3mm thick output coupler (CVI). 33

Figure 2.3 Mode-locked laser pulse train of 15 MHz repetition rate or 68 ns pulse separation at 50 ns/div. 34

Figure 2.2 5 reflections per each mirror in a 15 MHz laser are shown in a single path. 34

Figure 2.4 (a) Collinear interferometric autocorrelation trace showing a pulse duration of 16.5 fs assuming a $\mathrm{sech}^2(t)$ intensity profile, and (b) associated spectrum band width of 42 nm from the KLM Ti:Al_2O_3 laser. 35

Figure 2.5 Ti:Sapphire laser schematic with a pair of multiple pass cavity mirrors: R_1, R_2, 10 cm radius of curvature mirrors; R_3, R_4, 2" diameter MPC mirrors with 2 m radius of curvature (CVI); R_5, 20 cm radius of curvature; L, 12.5 cm focal length pump beam focusing lens; OC, 3.5 % 12.5mm thick output coupler. 36

Figure 2.6 (a) The low loss SBR structure is made with high and low index layers of AlAs/ AlGaAs reflector and GaAs quantum well where the electric field is shown in different positions. 37

Figure 2.7 Pump-probe trace for the SBR with 30 μm spot size, excited by a 10 fs, 806 nm Ti:Sapphire laser. 38

Figure 2.8 Mode-locked laser pulse train of 7.2 MHz repetition rate or 139 ns pulse separation. 38

Figure 2.9 For 7.2 MHz Ti:Sapphire laser: (a) Collinear interferometric autocorrelation trace showing a pulse duration of 23.5 fs assuming a $\mathrm{sech}^2(t)$ intensity profile; (b) associated spectrum band width of 31 nm. 39

Figure 2.10 8 reflections per each mirror in a 5 MHz laser are shown in a single path. . 39

Figure 2.11 Slope efficiency of a 5 MHz laser is measured: measurement (dot); linear fit (solid). 40

Figure 2.12 Ti:Al_2O_3 laser schematic with a pair of multiple pass cavity mirrors: R_1, R_2, 10 cm radius of curvature mirrors (Spectra-physics); R_3, R_4, 2" diameter MPC mirrors with 2 m radius of curvature (Spectra-physics); R_5, 50 cm radius of curvature mirrors (Newport); L, 6.3 cm focal length pump beam focusing lens; OC, 27% transmission, 1/2" thick output coupler (Spectra-Physics). 41

Figure 2.13 Group delay (dot) and group delay dispersion (solid) is measured with newly designed MPC mirrors. 42

Figure 2.14 (a) Intensity autocorrelation trace showing a pulse duration of 55 fs assuming a $\mathrm{sech}^2(t)$ intensity profile, (b) associated spectrum bandwidth of 14 nm from net negative dispersion KLM operation, (c) a pulse duration of 80 fs assuming a $\mathrm{sech}^2(t)$ intensity profile, (d) associated spectrum bandwidth of 19 nm from net positive dispersion KLM operation. 43

Figure 2.15 Oscilloscope trace of fast photodiode showing mode-locked laser pulse train of 4 MHz repetition rate or 250 ns pulse separation. 44

Figure 2.16 For constant pulse parameters of $g = 1$, $g = 1.15$, $l = 2.8$, $\Omega_g = 1$, $\mu = 2/3$, and the constant normalized energy of 1, with different 3th-order SPM d of zero (solid); 1 (dot), 2 (dash), 3 (dash-dot), 4 (dash-dot-dot), 5 (short-dash); (a) normalized pulse width (b) stability of pulses. 48

Figure 2.17 For constant pulse parameters of $d= 4$, $g = 1.15$, $l = 2.8$, $\Omega_g = 1$, $\mu = 2/3$, and the constant normalized energy of 1, with different 3thorder SAM m of zero (solid); 0.5 (dot), 1 (dash), 2 (dash-dot); (a) normalized pulse width (b) stability of pulses. 49

Figure 2.18 Different fitting functions to a measured autocorrelation function: autocorrelation (solid line); $\mathrm{sech}(t/t_p)^2$ (dash); Gaussian (dash-dot); modified sech (short dash). 49

Figure 3.1 Schematic diagram of various excitations and their relaxation mechanisms for electrons in a sold. The analogous diagram holds for holes. 55

Figure 3.2 Avalanche coefficients of b and g are determined from Eq. (3.14) and (3.15) for fused silica (solid) and BK7 (dot). 59

Figure 3.3 Electron density produced by avalanche ionization and multiphoton ionization (dot) is plotted with a sech-squared pulse (solid) that photoexcites fused silica. 60

Figure 3.4 Electron density produced by avalanche ionization and multiphoton ionization (dot) is plotted with a sech-squared pulse (solid) that photoexcites BK7 or Corning 2947 glass. 60

Figure 3.5 Schematics of waveguide fabrication with a Ti:Sapphire laser that incorporates a pair of multiple pass cavity mirrors; R_1, R_2, 10 cm radius of curvature (ROC) mirrors; R_3, R_4, 2" diameter MPC mirrors with 2 m ROC; R_5, 50 cm ROC; R_5, 20 cm ROC; L, 6.3 cm focal length pump beam focusing lens; OC, 27% transmission, 1/2" thick output coupler; external prism compressor that consists of a pair of SF10 prisms; Slide glass, Corning 2947. 63

Figure 3.6 Microscope images of different sizes of waveguides, depending on the scanning speed of Ti:Sapphire laser beams. 64

Figure 3.7 The scanning speed dependence of the size of waveguides fabricated: measurement (square-dot), fitting (solid); cumulative intensity dependence of the size of waveguides: measurement (circle-dot), fitting (dot). 65

Figure 3.8 Mode profiles measured with 544 nm He-Ne lasers: with the different radii of the core (a) 10 μm; (b) 7.5 μm; (c) 4 μm; (d) 2 μm. 66

Figure 3.9 Mode profiles measured with cw 800 nm Ti:Sapphire lasers: with the different radii of the core (a) 10 μm; (b) 7.5 μm; (c) 4 μm; (d) 2 μm. 67

Figure 3.11 A Y-coupler (a) Top view; (b) Front view; (c) Output mode shape launched with 800 nm laser beams at the output port. 68

Figure 3.10 A grating is fabricated by chopping incident Ti:Sapphire laser beams. . . . 68

Figure 3.12 An X-coupler (a) Side view shown at the input por; (b) Output mode profiles launched with 544 nm laser beams at the input port; (c) Side view of at the output port. (d) Output mode profiles launched with 544 nm laser beams at the output port. 70

Figure 3.13 (a) Side view of an X-coupler shown at the input port. (b) Top view of the X-coupler. (c) The power at the output of an X coupler with a 544 nm He-Ne laser beam coupled into the input of one of the waveguides; input into one of the waveguide (dot), input into the other (solid). The inset shows images of the far-field modes. 71

Figure 3.14 544 nm He-Ne laser beams are coming out through vertically separate waveguides that are 130 um apart; (a) from the bottom waveguide; (b) from the top waveguide. Laser beams are coming out through vertically and laterally stacked waveguides that are 20 μm apart vertically with (c) a 800 nm Ti:Sapphire laser; (d) 544nm He-Ne laser. 72

Figure 4.1 Schematic diagram of the lattice hops shows Ga out-diffusion from a QW and the QW interface crossings, carried out by group-III vacancies, during the random walks associated with their diffusion (adapted from [78]). 79

Figure 4.2 These diagrams illustrate the change of atomic compositions (a) before QWI, (b) during QWI, and (c) after QWI by the diffusion of vacancies, which help interdiffusion of group-III atoms of Ga and Al. 80

Figure 4.3 Schematic illustration of Frenkel defect pairs created in GaAs near the crystal surface. Interstitial defects can react with the As vapor at the crystal surface, thus determining equilibrium defect concentrations in GaAs bulk crystal. . 81

Figure 4.4 Layer structure of the sample: most of the point defects are mostly created in the absorptive quantum well layers (1064 nm) or the contact layer (532 nm), where pulsed light beams transmit through SiO2 antireflection coating or reflect from the Au coating (adapted from [28]). 82

Figure 4.5 Structure of epitaxial layers for the PLAID process. 85

Figure 4.6 Photon energy is absorbed and deposited on different layers from the top of the capping layer to the MQW regions. The dots indicate the interfaces of different layers. 86

Figure 4.7 Processing steps for oxide coating, PLAID, and etching 86

Figure 4.8 Schematic diagram for PL measurement: OSA, optical spectrum analyzer; MMC, multi-mode fiber coupler; Lens, 0.16NA 5 mm diameter, f = 15.36 mm. 88

Figure 4.9 The irradiated fluence is 300 mJ/cm^2. Photoluminescence spectra measured at room temperature, after 650 °C rapid thermal annealing for 2 min show a maximal peak shift of 33 nm, compared to the bandgap shift of the control (circle). 88

Figure 4.10 The blue-shift of photoluminescence is measured; the PLs of the InGaAsP/InGaAsP MQW sample after the RTA and laser irradiation with no irradiation (solid), the fluence of 65 mJ/cm^2(dash), and 125 mJ/cm^2(dot), respectively. . 89

Figure 4.11 The intensity changes of PLs are measured as the irradiation of 532 nm Nd:YAG laser beams on MQW samples increases with different fluences and fixed RTA at 675 °C for 3 min; 20 mJ/cm^2 (solid), 65 mJ/cm^2 (dash), 100 mJ/cm^2 (dot), and 125 mJ/cm^2 (dash-dot). 90

Figure 4.12 The bandgap shifts are represented by measuring the wavelength shifts of the peak value of each PL; the effect of laser irradiation at 532 nm with no irradiation (control), the fluence of 65 mJ/cm^2 and 125 mJ/cm^2. 90

Figure 4.13 The blue-shift of PLs is measured to observe the effect of RTA time with an InGaAsP/InGaAsP MQW sample after the 3 minutes irradiation of 535 nm, 20 Hz Nd:YAG laser beams with the fluence of 125 mJ/cm^2. These samples are annealed at 675 °C; the control sample after the RTA only and the MQW sample after PLAID and RTA. 91

Figure 4.14 The blueshift of PLs is measured to observe the effect of RTA with an InGaAsP/InGaAsP MQW sample after the 3 min irradiation of 20 Hz Nd:YAG laser beams with the fluence of 125 mJ/cm^2, annealed at 675 °C for 3 min; a control sample after the RTA only (solid); 532 nm excitation (dot); 1064 nm excitation (dash). 92

Figure 4.15 Microscope images of the surface (a) bare surface, (b) after 640 nm SiO_2 coating (c) After PLAID with 65 mJ/cm^2, (d) After wet etching of InGaAs/InP capping layers 93

Figure 4.16 Microscope images of the surface: (a) After PLAID with 125 mJ/cm^2, (d) After wet etching of InGaAs/InP capping layers. 93

Figure 4.17 Laser induced surface melting, ablation, and liquid phase expulsion; h is ablation depth. 96

Figure 4.18 Variation of temperature with time for a uniform heating around the surface bounding a semi-infinite half-space, launched with 3 ns, 532 nm wavelength, and 81 mJ/cm^2 fluence: surface (solid), 10 nm deep (dash), 20 nm deep (dot), 30 nm deep (dash-dot), 40 nm deep (dash-dot-dot), and 50 nm deep (short dash). 98

Figure 4.19 Variation of temperature with depth for a uniform heating over the surface bounding a semi-infinite half-space, launched with 3 ns, 81 mJ/cm^2: after 0 s (solid); t_p (dash); $3t_p$ (dot); $5t_p$ (dash-dot). 98

Figure 4.20 Temperature dependence of melting fluence with Nd:YAG lasers at 532 nm: InGaAs (Solid); InP (dash); GaAs (dot); Si (dash-dot). The dots at the kinks indicate the threshold fluence. 102

Figure 5.1 (a) An integrated triangular unidirectional ring laser; TIR, total internal reflecting mirror. (b) An integrated S-crossover unidirectional ring laser (adapted from [35] and [36]). 106

Figure 5.2 (a) A unidirectional ring laser resonator into which an S-crossover waveguide is incorporated; L_1, the length of right half segment; L_2, the length of left half segment; L_S, the length of the S-crossover segment; L_3, the length of a segment from CW output port to Y-branch on the bottom; r, bend transmission coefficient from the straight waveguide to the S-crossover waveguide; t, transmission coefficient from the straight waveguide to straight waveguide. (b) A unidirectional ring laser resonator into which a distributed Bragg reflector or an etched facet is incorporated; L_R, the length of the ring; L_b, the length of retro-arm; R, the radius of curvature. 107

Figure 5.3 Overall reflectivity of an S-crossover ring laser in wavelength domain is plotted with three different transmissions at Y-junctions, k = 0.8 and q = p, i = c1, c2, and o; $R_j = 0.2$, $T_j = 0.6$ (solid); $R_j = 0.15$, $T_j = 0.65$ (dash); $R_j = 0.1$, $T_j = 0.7$ (dot). 110

Figure 5.4 Overall reflectivity of a retro-reflected ring laser in wavelength domain is plotted with three different transmissions at an evanescent coupler, k = 0.98 and q = 0, and $R_b = 1$; $R_c = 0.08$, $T_c = 0.9$ (solid); $R_c = 0.48$, $T_c = 0.5$ (dash); $R_c = 0.88$, $T_c = 0.1$ (dot). 110

Figure 5.5 Conceptual diagram of unidirectional lasers with a directional coupling S_{couple}, where both CW and CCW resonators have identical carrier densities and photon lifetimes and dots represent photons. 112

Figure 5.6 (a) An S-crossover ring laser with two output arms. (b) A retro-reflected ring laser with two output arms. 114

Figure 5.7 Unidirectional macroscopic hybrid ring laser into which an S-crossover fiber is incorporated. The laser consists of an SOA and single mode fibers. The circulating beam is coupled out with a 90% evanescent fiber coupler; SMF28, Corning single mode fiber at 1.55 mm; PC, polarization controller. 116

Figure 5.8 Unidirectional macroscopic hybrid ring laser into which a variable retro-reflector of a fiber Bragg grating (FBG) is incorporated. The circulating beam is coupled out with a 10% evanescent fiber coupler. 117

Figure 5.9 Gain contours of current versus wavelength. The contours of a constant gain are separated by 3 dB. 119

Figure 5.10 Calculated L-I curves in an integrated S-crossover ring laser as the S currents are constant and the ring current increases; (a) CW direction (c) CCW direction. Measured L-I curves in an S-crossover hybrid semiconductor ring laser; (b) CW direction (d) CCW direction; 0 mA (solid); 100 mA (dash); 200 mA (dot); 300 mA (dash-dot); 400mA (dash-dot-dot). 121

Figure 5.11 (a) Calculated reciprocity breaking curves of the CW and CCW output power in an integrated S-crossover ring laser as the S current increases and the ring currents are constant. (b) Measured reciprocity breaking curves in an S-crossover hybrid semiconductor ring laser. 122

Figure 5.12 Calculated reciprocity breaking curves in an integrated S-crossover ring laser; (a) as the S currents are constant and the ring current increases (c) as the S current is fixed and the ring currents increase. Measured reciprocity breaking curves in an S-crossover hybrid semiconductor ring laser; (b) as the S currents are constant and the ring current increases (d) as the S current is fixed and the ring currents increase. 123

Figure 5.13 Calculated L-I curves in an integrated retro-reflected ring laser as the retro-reflectivity is constant and the ring current increases; (a) CW direction (c) CCW direction (e) retro-reflection output. Measured L-I curves in a retro-reflected hybrid semiconductor ring laser; (b) CW direction (d) CCW direction (f) retro-output; 100% (solid); 10% (dash); 1% (dot); 0.1% (dash-dot); 0% (dash-dot-dot). 125

Figure 5.14 (a) Calculated reciprocity breaking curves in an integrated retro-reflected ring laser as the retro-reflectivity increases and the ring currents are constant. (b) Measured reciprocity breaking curves in a retro-reflected hybrid semiconductor ring laser. 126

Figure 5.15 Calculated reciprocity breaking curves in an integrated retro-reflected ring laser; (a) as the retro-reflectivity is constant and the ring current increases (c) as the retro-reflectivity increases and the ring currents are constant. Measured reciprocity breaking curves in a retro-reflected hybrid semiconductor ring laser; (b) as the retro-reflectivity is constant and the ring current increases (d) as the retro-reflectivity increases and the ring currents are constant. 127

Figure B.1 Asymmetric Y-branch or fork; width of 2 μm, index of core of 3.5, and index of background of 3.3. 140

Figure B.2 Contour map of transverse electric field launched from each port; (a) $a_1 = 1$ (b) $a_2 = 1$ (c) $a_3 = 1$. 141

List of Tables

TABLE 2.1 Theoretical calculation shows the laser parameters which are associated with a unity q transformation produced by MPC mirrors with 100 cm focal length. . 33

TABLE 2.2 Comparisons of pulse widths that correspond to different pulse envelope functions. As a result, the pulse width is 60 fs instead of 55 fs. 50

TABLE 3.1 For 800 nm (1.55 eV) photoexcitation, the effective ionization energy D, the number of photons to exceed the bandgap, n_{photon}, avalanche coefficient g, multiphoton absorption cross-section s_k [66], and threshold intensity for material ablation I_{th}. 61

TABLE 4.1 Temperature independent parameters [1][94]. 100

TABLE 4.2 Temperature dependent parameters [95][96][97][98]. 101

TABLE 4.3 A comparison of threshold fluences for melting between theoretical calculation and experimental determination, with Nd:YAG lasers at 532 nm [99][100]. 102

TABLE 5.1 Parameter values used in rate equations. 118

TABLE B.1 Major parameter values of FullWAVE simulation; PML, perfectly matched layer. 142

TABLE C.1 Diagrams of different terms and corresponding features of an S-crossover resonator in Fig. 5.29(a). 146

Chapter 1

Motivation and Introduction

1.1 Motivation and Objective

The most developed applications of lasers are laser micromachining such as drilling, cutting, and shaping, and the material processing of annealing, recrystallization, and metallurgy. Laser induced chemical processing exposes materials with reactive or nonreactive media in order to achieve etching, material deposition, and chemical transformation. For electrical and photonic devices, lasers are irradiated to develop electronic circuits, optoelectronics, photonic integrated circuits, semiconductor manufacturing, and sensor technology [1]. Moreover, Laser ablation is applied to *in situ* repair optoelectronic devices [2]. Two major advantages of laser-induced micromachining are direct patterning and writing on large areas of substrates at high speed following the exposure of laser light, without using complicated photomask steps.

The objective of this thesis is to develop advanced laser resonators and applications for laser-induced micromachining for photonic circuit fabrication. A novel femtosecond laser resonator is developed to achieve micromachining of passive photonic devices using its high intensity pulses. Furthermore, active photonic devices of bandgap manipulated quantum well structures are fabricated with a standard nanosecond Nd:YAG laser. Finally, high-density integration of unidirectional semiconductor ring lasers is developed, for which hybrid semiconductor fiber ring lasers are developed to demonstrate their unidirectional operation.

1.2 Advent of Photonic Integrated Circuits

Most telecommunication components tend to be bulky and require complicated assembly and fiber management. As a result, the products demonstrated so far are not only expensive, but also consume excessive space and power. Next generation products will need to drive down both cost and space and improve performance. These requirements provide the motivation for high density-integration toward multiple functions on a single substrate that leads to an optical module in a single package. As photonic integration becomes increasingly important in the years to come, its development will focus primarily on planar lightwave integrated circuits on three primary materials, silica on silicon for passive devices and InP for active/passive devices, polymers/glass for hybrid integration [3].

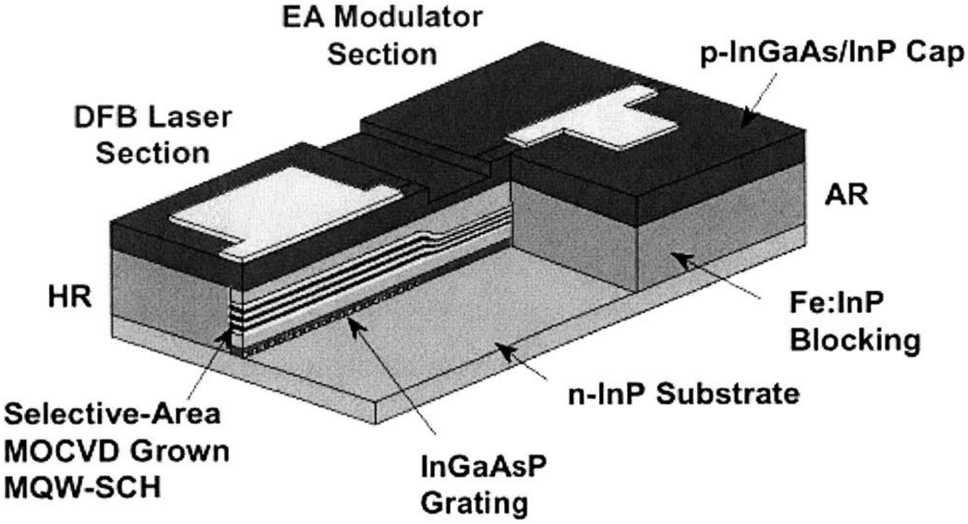

Figure 1.1: Full optoelectronic integration is used to create monolithic systems. Schematic view of multi-quantum well, electro-absorption modulator integrated DFB laser with semiconductor insulating buried heterostructures [4].

Monolithic integration of several photonic devices, so called photonic integrated circuits (PIC), was originated by Miller from Bell Labs in mid 1960s [4]. PICs are a subset of optoelectronic integrated circuits (OEIC) utilizing a single substrate for the monolithic integration of optically interconnected guided-wave optoelectronic devices [5]. In OEICs, the optical device functions only as a terminal device to convert a processed electrical signal into an encoded optical signal for fiber transmission, or vice versa [6]. In contrast, PICs contain optically interconnected devices that reroute, condition, or process the signal while still in its optical form of photons. PICs offer the promise of superior performance, compact size, reliability, cost reduction, low power consumption, and increased packaging robustness without the complicated fiber links [7]. The driving force for development of PICs is the expected complexity of next-generation optical communications links [8], networking architectures, and even integrated biosensors [9].

1.3 Novel Ultrafast Laser Resonator for Passive Waveguide Micromachining

Over the last couple of years, numerous groups have evaluated the use of ultrashort pulses of femtosecond duration for micromachined photonic devices [10][11][12][13][14]. Micromachining with laser pulses of a very short duration of a femtosecond scale essentially eliminates heat flow to a surrounding material. Thermally induced substrate degradations can be circumvented, as opposed to most standard machining techniques with long pulses of microsecond or nanosecond duration. One such application is glass machining, which is a much more subtle endeavor than machining of metals or semiconductors. Photonic devices fabricated by a high intensity pulsed laser are a way to develop cost effective and high capacity switching systems for optical communications. This intense pulsed laser helps to fabricate microphotonic devices, such as waveguides and three dimensional optical memories, by making permanent index changes at the focal point in glass, while leaving off-focal points with no effect.

Inherently, the intense laser light, which can efficiently penetrate into deep layers of transparent materials, is able to fabricate virtually any three dimensional passive photonic devices. With PICs that are packaged or contacted with bulk glass, any path of a permanent waveguide can be inscribed selectively by moving the focal point of high intensity femtosecond pulses. This micromachining system using nonlinear material processing based on femtosecond lasers, requires a laser source, optics for conditioning and focusing the beam, and a way to precisely control and point the beam.

In the last decade, significant advances have been made in the development of Kerr-lens mode-locked solid-state lasers utilizing the optical Kerr effect. Usually standard femtosecond lasers deliver typical pulse energies of several nJ and peak power of several hundreds of kW.

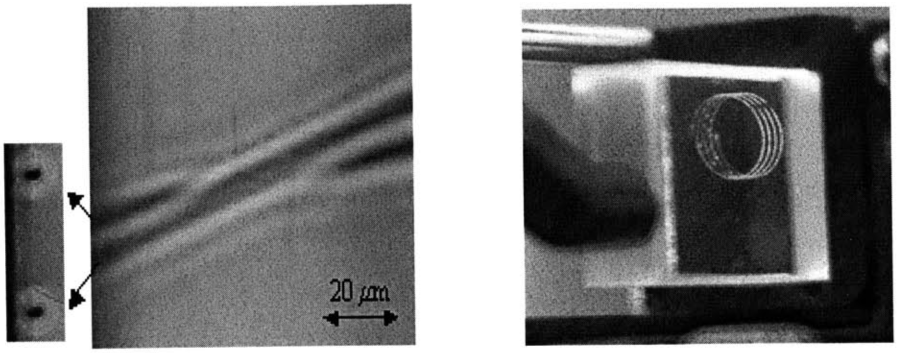

(a) (b)

Figure 1.2: Femtosecond micromachining has achieved to create (a) X-coupler [13] and (b) a three dimensional helical waveguide [17], within a glass substrate using localized changes of refractive index.

However, recent studies demonstrated the generation of sub-10 fs optical pulses with pulse energy of 13 nJ and peak power up to 1.5 MW at repetition rate of 100 MHz [15]. Although these Kerr-lens mode-locking (KLM) lasers can produce short pulse duration and high average powers, they typically have high repetition rates of 100 MHz. This can make ultrafast measurements, e.g. pump-probe measurements, difficult because the average power for a given pulse energy is high. In recent years, cavity dumping has been used to increase output pulse peak power from a KLM Ti:Sapphire lasers. Pulses of 13 fs with 5 MW peak intensities at repetition rates of 200 kHz have been directly generated from laser resonators [16]. Cavity dumping achieves increased pulse energies at lower costs than conventional resonator amplifiers, however, it is still a relatively complex technique because it requires the use of a high performance intracavity Bragg diffraction cell.

Although standard ultrafast processing needs complicated laser amplifiers that can produce pulse energies of μJ [10][11], recent progress has enabled micromachining with a few nano joule pulse energies and demonstrated waveguide fabrication [12][13][14]. Benefits of the femtosecond Ti:Sapphire laser resonator include compactness and the capability to be all solid state.

Hence, an important aim is to increase laser output pulse energies and intensities. Generation of femtosecond pulses with high intensities in the MW range is essential for a number of applications including laser micromachining and ultrafast nonlinear optical phenomena.

Since the average output power is constant from a fixed pump power, the pulse energy can be increased by reducing the laser repetition rates in mode-locked operation. The reduction of pulse repetition rate from a 100 MHz range to several MHz represents a significant advantage for nonlinear and ultrafast studies, because it reduces thermal parasitics, sample damage problems, and recovery time artifacts. Also, increasing pulse energies without using cavity dumpers or amplifiers yields a low cost and simple system. In this thesis, I demonstrate significant improvement in pulse energy and peak power from a KLM Ti:Sapphire laser using a multiple pass cavity as a novel long cavity geometry.

I demonstrate an X-coupler on soda lime glass (Corning 2947) using approximately 25 nJ pulse energies and 80 fs pulse durations from the novel high intensity laser resonator with a 0.6 numerical aperture (NA) microscope objective, as shown in Fig. 1.2(a) [13]. The far field pattern of coupled light of a He-Ne laser is measured for this device in Chap. 3. Researchers at Clark MXR inc. in collaboration with Winick of University of Michigan, use a femtosecond micromachining workstation based on a Ti:Sapphire laser amplifier to directly write localized index of refraction changes within a glass substrate. They create a three dimensional helical optical waveguides, as shown in Fig. 1.2(b) [17].

1.4 Pulsed Laser Absorption Induced Disordering for Active Device Integration

There are engineering challenges in PICs that should be overcome to combine active photonic sources, passive waveguides, and electronic control functions at micron dimensions. Obviously, the fabrication processing of bandgap engineering is critical to realizing the potential benefits of PIC, because the different active/passive devices need different band gaps within the epiwafer [18][19].

This thesis is about one key technological challenge in expanding the versatility, practicality, and functionality of optoelectronics: research aimed at the integration of multiple-function devices onto a single substrate. Practicality requires low manufacturing cost, high reliability, and low operating cost of commercial PIC devices. The primary requirement for waveguiding PICs is bandgap compatibility among the various optoelectronic devices.

Optimum performance demands that the bandgap energies of the various components be related to each other in a specific fashion. Conventionally, the process for fabricating PICs

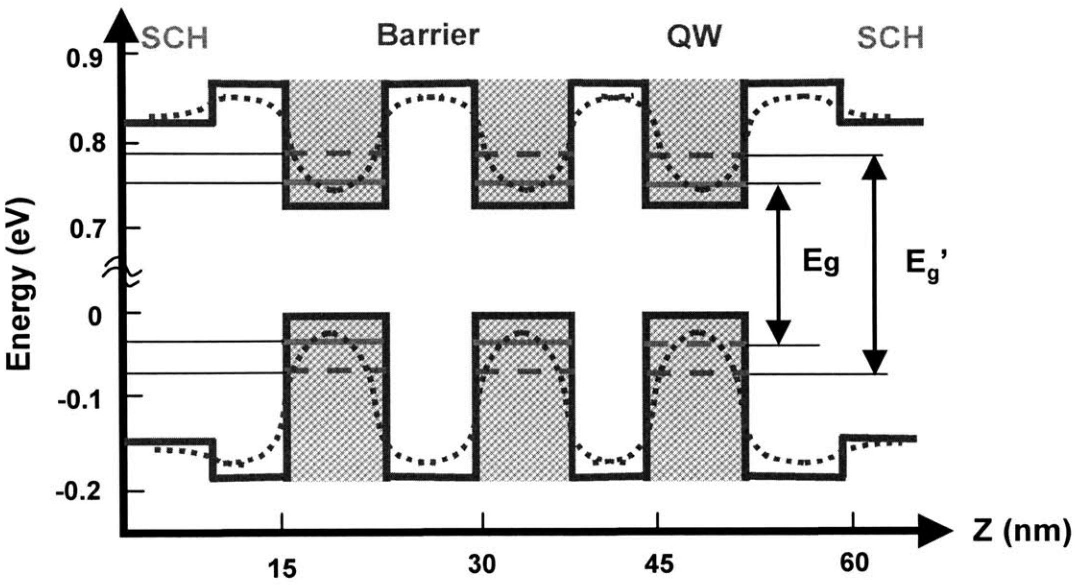

Figure 1.3: Schematic diagram of quantum well intermixing, SCH, separate confinement heterostructure: (a) the bandgap before intermixing, E_g and band structure (solid); (b) the bandgap after intermixing E_g' and band structure (dot).

with different bandgaps consists of three steps: patterning, etching out the unwanted epitaxial layers, and subsequent selective epitaxial regrowth over the entire wafer. Selective area regrowth is by far the most flexible and widely used method. It allows the growth of a sequence of epitaxial layers for one component on the chip and locally removes regions on the wafer for the next component by wet or dry etching. It then grows another sequence of epitaxial layers in a separate step. This procedure can be repeated as many times as needed. The butt-coupling efficiency, which means that at a certain location one guide is terminated and the other begins between components, of better than 90% is achieved by this technique. Since every component is manufactured independently, the material properties for each component, such as thickness and composition of the layers, doping profile, and concentration, can be designed to optimize performance without constraints imposed by the next component. However, regrowth is complex and cumbersome, requires a fair amount of finesse, and worst of all, is expensive, because the epitaxial growth with high quality is a complicated task.

As a promising approach to introducing different bandgaps on one wafer, quantum well intermixing (QWI) emerges as a powerful technique for fabricating PICs as well as generates considerable interest due to its simplicity [20]. This compact and simple method of fabricating optical integrated circuits enables the creation of different bandgap regions across an epiwafer without the need for complex, multiple growth steps, and it also provides a great deal of flexibility for design. Therefore, this technique has been used to fabricate multiple wavelength quantum well (QW) lasers without using the complicated processes of etching or epitaxial regrowth. Other advantages of using QWI technique are that it is simple and compatible with the existing fabrication technologies of semiconductor lasers.

The QWI is based on a fact that a QW is an inherently metastable system due to the large concentration gradient of atomic species across the interface between the QW and the barrier. At high temperatures, diffusion of atomic species will occur, resulting in an intermixing of the QW and adjacent barrier materials, as illustrated schematically in Fig 1.3. This intermixing process can be significantly enhanced by the presence of impurities or point defects in the vicinity of the interfaces of the QW. Due to hopping of individual atoms in point defects from one lattice site to another, the QW smears with adjacent barrier materials [20][21]. Essentially, three different QWI methods by which the defects are introduced have been developed, including impurity-induced disorder (IID) [21][22], impurity free vacancy disorder (IFVD) either by dielectric cap [23][24] or ion implantation [25][26][27], and laser or photoabsorption induced disorder (PAID) [28][29][30][31].

The absorption of high-energy photons from a laser causes bond breaking and lattice disruption in the sample, which lead to an increase in the point defect density. To achieve high spatial separation between intermixed and as-grown regions, pulsed laser beams are used, because continuous irradiation of laser beams heats a large lateral volume [30]. I coin them to be a pulsed-light absorption induced disordering (PLAID). It is especially interesting that frequency-doubled Nd:YAG lasers at 532 nm generate most defects in the capping layer rather than the defects that are generated in the separate confinement heterostructure and multi-QW/ barrier regions at 1064 nm [32]. Thus, the remnant defects excited by PLAID using 532 nm pulses can be easily etched away to maintain the good crystal quality of QWs after QWI. The capping layer can be regrown to provide metal contacts later on.

1.5 Microphotonic Ring Laser Resonator for Photonic Integrated Circuit

Integrated semiconductor lasers will be associated with various photonic circuits, e.g. semiconductor optical amplifiers, modulators, channel dropping filters, etc in a single optoelectronic chip [33]. However, state of the art optoelectronic integration techniques have not been developed for densely integrated multiplexing devices, mainly because of the fabrication limitations of cleaved-facet necessity of Fabry-Perot Laser (FPL) and vertical optic coupling of VCSEL [34]. In order to overcome this shortcoming of laser integration, a distributed feedback (DFB) or a distributed Bragg grating (DBR) of FPL and vertical packaging of VCSEL have been recently introduced. On the other hand, DFB and DBR lasers still suffer from one-dimensional integration due to inflexibility of e-beam lithography or laser micromachining for grating fabrications, and VCSEL requires elaborate horizontally-guided optical beam delivery system due to the vertical beam output. Since the ring sizes in ring lasers are determined by lithography, not like FPL with cleaved facets, the repetition rate in mode-locked operation is well controlled. Furthermore, the unidirectional lasers eliminate spatial hole burning due to traveling wave operation, which results in high side mode suppression ratio and reduced sensitivity to feedback. However, the operation with unidirectional and single transverse mode in previous scheme has not been demonstrated [35][36]. Therefore, I propose to achieve a single longitudinal and transverse mode at 1.55 μm with the unidirectional continuous wave operation toward the new generation PIC. The unidirectional operation with S-crossover or retro-

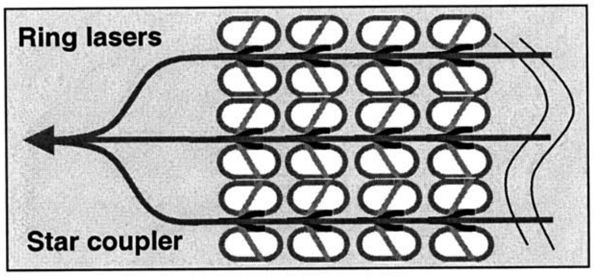

Figure 1.4: Ring lasers that have different characteristics are densely integrated in two dimensions, and output laser beams are combined with a start coupler

reflected ring lasers are suggested and demonstrated with their macroscopic, hybrid semiconductor-fiber rings.

1.6 Overview of Chapters

This thesis is devided into four main chapters and the first one for introduction and the last one for conclusions. Chap. 2 describes a novel high intensity Ti:Sapphire laser design for photonic circuit fabrication onto transparent dielectrics. In particular, Kerr-lens modelocking in long cavity geometry is carefully studied and demonstrated for low repetition rates of 15 to 4 MHz, based on unity q parameter transformation of Gaussian modes. Chap. 3 is intended to explain material decomposition or ablation mechanism by photo-excitation using highly intense femtosecond pulses, and index changes of glass materials by microexplosion. Then, the fabrication of several, two-dimensional and three dimensional, passive photonic devices are demonstrated. Chap 4. gives a comprehensive overview and methodology of quantum well intermixing and focuses on the pulsed laser absorption induced disordering using Q-switched Nd:YAG lasers. An intuitive theoretical model is set up to determine the threshold laser fluence for point defect generation related to lattice melting. Chap. 5 introduces two different designs of semiconductor ring lasers for unidirectional operation. A coupled rate equation model is developed to unravel unidirectionality of laser operation that is demonstrated with macroscopic, hybrid semiconductor-fiber ring lasers. Chap. 6 summarizes all results and envisions high density laser integration using the technology of pulsed laser absorption induced quantum well intermixing. Appendix A gives a quick derivation of laser parameters of a quintic order nonlinear Schrödinger equation for solitary pulses formation. Appendix B describes the method of obtaining the coefficients of Scattering matrix in an asymmetric Y-branch using finite difference time-domain simulation. In Appendix C, the resonance filter properties of the unidirectional ring lasers are derived using diagrammatic path integrations.

Chapter 2

Novel High Intensity Ultrafast Laser Resonator

2.1 Introduction

Reliable ultrashort laser systems open up micromachining of materials which is impossible with very high precision using standard long pulse, nanosecond, laser systems. Femtosecond (fs) laser pulses for nonlinear micromachining have received much attention, because nonlinear optical breakdown induces permanent structural changes without transferring photoexcitation energy to the lattice. Until now, most fs-micromachining requires the pulse energies of μJ and the pulse durations of 100 fs from amplified laser systems [10][11]. However, these complicated and costly laser amplifiers operate at kHz, highly limiting the processing speed in many applications. Near-infrared fs-pulses are especially useful because these laser beams transmit transparent dielectric material, generating three-dimensional (3D) structures in wide bandgap glasses. With fs-pulse excitation with narrow bandgap materials of semiconductors, no vapor or plasma plume after the linear absorption can develop, leaving the clear-cut microstructuring.

Standard femtosecond lasers deliver pulse durations of 50 fs, pulse energies of several nJ, and peak powers of several hundreds of kW. The peak power directly generated by these mode-locked laser sources is often insufficient for studies of nonlinear phenomena. Several amplification techniques have recently been developed to extend the available pulse energies in the microjoule to millijoule range. However, the requirement of multiple stages of lasers makes these oscillator-plus-amplifier systems complex and expensive. Further, the repetition rate in kHz range from many of these sources is low enough to limit detection sensitivity for ultrafast measurements.

I demonstrate that laser repetition rates decrease further to lower than 5MHz and pulse energies increase to more than 100nJ, using extended cavity schemes for generating high intensity femtosecond pulses. I focus on techniques which will generate high intensity pulses directly from a mode-locked laser oscillator without using additional active devices such as amplifiers or cavity dumpers. Although these methods will not achieve as high pulse energies as traditional short pulse amplifiers, they offer a significant advantage in cost and system complexity, which enables fs-micromachining at ultrahigh speed as well as with a compact and cost-effective system.

The high pulse energy can be applied to generate continuum by focusing it on a short length of single-mode optical fiber. This continuum source can be applied for ultrahigh resolution imaging in optical coherence tomography [37], for a tunable laser source in a pump-probe time-resolved spectroscopy, and for direct pulse compression. Waveguide fabrication using micromachining or microstructuring on transparent glass material with fs-pulses will be also one of the most interesting applications of the high intensity laser beam. Hence, the development of low cost and high intensity laser sources will enable a wider range of femtosecond measurement applications, making this technology more available to both the research and the development community.

State of the art KLM Ti:Al_2O_3 (Ti:Sapphire) lasers have achieved pulse durations as short as 5.5 fs directly from a laser resonator using double chirped mirrors in combination with a CaF_2 prism pair [38] or a fused silica prism pair [39]. After externally spectral broadenig, pulses are compressed down to 4.5 fs [40][41]. Recent studies demonstrated the generation of sub-10 fs optical pulse with pulse energy of 13 nJ and peak power up to 1.5 MW at repetition rate of 100 MHz [12]. Other studies have changed the standard resonator design for these lasers to create compact laser resonators at repetition rates of 1 GHz by exploiting novel dispersion compensation technique [42]. Although these KLM lasers can produce short pulse duration and high average powers, they typically have high repetition rates of 100 MHz. This can make experimental measurements difficult because the average power for a given pulse energy is high. In recent years, cavity dumping has been used to increase output pulse peak power from a KLM Ti:Sapphire lasers [43]. Pulses of 13 fs with 5 MW peak intensities at repetition rates of 200 kHz [16] have been directly generated from laser resonators. Cavity dumping achieves increased pulse energies at lower costs than conventional resonator amplifiers, however, it is still a relatively complex technique because it requires the use of a high performance intracavity Bragg diffraction cell.

2.2 Extended Cavity and Novel Laser Design

In fs-lasers, the objective is to increase the laser output pulse energies and intensities by increasing cavity lengths [44]. Since the total average output power of the laser cannot be increased, the pulse energy is increased by reducing the repetition rate. Researchers have developed long lasers by simply increasing cavity lengths in spontaneously mode-locked xenon lasers [45] as well as by implementing an intracavity White cell in mode-locked Nd:YAG lasers [46]. The development of a long cavity femtosecond laser requires careful design because the laser cavity must be operated in a particular subset of its stability region for optimum KLM performance.

The cavity length is extended by a Herriott style multiple pass cavity (MPC) [47], which has been used for optical delay lines as well as Raman gas cells [48]. The MPC is designed for a unity q parameter transformation [49] that is very important for maintaining laser mode properties that are the same as a standard laser resonator. The MPC is constructed by a pair of curved mirrors separated by a given distance. Both mirrors have notches cut in them in order to introduce and extract the optical beam. The optical beam is introduced into the MPC so that it strikes the first mirror off center and subsequently bounces between the two mirrors in a circular pattern, and it can be extracted after a given number of passes. The beam is also focused on subsequent bounces so that its propagation resembles propagation through a periodic lens array. This device is designed such that it provides a unity transformation of the q parameter of the laser beam after a given number of transits. Thus, if this device is inserted into the KLM laser, it can have a zero effective length and leaves the laser cavity mode and nonlinear focusing behavior invariant.

The angular rotation of the elliptical spot pattern produced on each pass in Herriott style MPC is given by [47]

$$\theta = \cos\left(1 - \frac{d}{2f}\right)^{-1} \tag{2.1}$$

where θ is the rotation angle, d is the separation between two curved mirrors, and f is their focal length. The re-entrant or closure condition in MPC requires that

$$2\nu \cdot \theta = \mu \cdot 2\pi \tag{2.2}$$

where 2ν is the total number of passes to closed ray paths and μ is an integral number of azimuthal revolutions such that the propagation beam makes around the MPC optics axis [48]. To describe the unity transformation of the q parameter in MPC, I introduce an ABCD matrix that is composed of one free space propagation followed by one mirror reflection. That is

$$ABCD = \begin{bmatrix} 1 - \frac{d}{f} & d \\ -\frac{1}{f} & 1 \end{bmatrix} \tag{2.3}$$

One can simply derive the re-entrant condition by solving an eigenvalue Eq. (2.3). Since that condition determines ray paths to be closed, it should not be changed whether there is a single notch in one of mirrors or a pair of notches in the MPC. It is crucial to note that a negative unity q transformation is apparently achieved by ν reflections that are the half of the total number of passes because the final reflection, $2\nu^{th}$, is lost by the inlet notch. In this case, the overall ABCD matrix in one way trip is equivalent to a negative unit matrix. Thus the unity q transformation can be performed in round trip, i.e.,

$$ABCD^{2\nu} = \tilde{1} \tag{2.4}$$

For a fixed focal length f, the number of passes ν through the MPC and the mirror separation d can be determined by the condition on that the overall ABCD matrix in one way should be negative unit matrix to achieve a unity q transformation in round trip. This analysis can be accomplished by a computational algorithm that iteratively varies both ν and d. Some of the numerical results are given in Table 2.1. When the number of passes ν is over 20, the cavity becomes too lossy because the reflectance of MPC mirrors is approximately 99.8% including scattering loss. Thus designs with large number of passes are not experimentally viable unless extremely low loss mirrors are used.

TABLE 2.1: Theoretical calculation shows the laser parameters which are associated with a unity q transformation produced by MPC mirrors with 100 cm focal length.

Repetition rates [MHz]	15	13	11	10	7.8	5.5	3.8
Number of passes, ν	10	8	18	16	12	6	6
Mirror separation, d [cm]	82.44	23.5	71.44	88.89	148.24	123.46	239.02

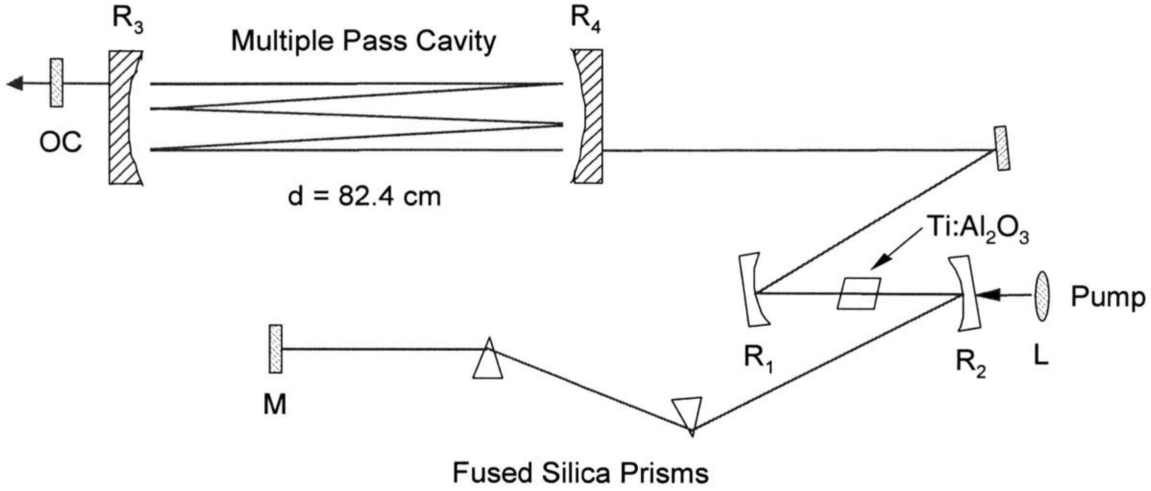

Figure 2.1: Ti:Sapphire laser schematic with a pair of multiple pass cavity mirrors: R_1, R_2, 10 cm radius of curvature mirrors (Spectra-physics); R_3, R_4, 2" diameter MPC mirrors with 2 m radius of curvature (CVI); L, 12.5 cm focal length pump beam focusing lens; OC, 10 % 3mm thick output coupler (CVI).

2.3 15 MHz, High Intensity KLM Laser with Multiple Pass Cavity

The laser consists of a standard, dispersion compensated KLM Ti:Al_2O_3 with a MPC incorporated into the nondispersive arm as shown in Fig. 2.1. The MPC mirrors have 100 cm focal length and 6 mm notch cut to introduce and extract laser beams. They are aligned using an output beam of a 100 MHz laser. The crystal is 3mm long and Brewster cut. Focusing mirrors with 10 cm radius of curvature are used in a folded Z-configuration. The physical lengths of both arms of the cavity are nearly 115 cm. Dispersion is compensated by a pair of fused silica prisms separated by a distance 75 cm. Mode-locking is achieved at 15 MHz repetition rate where the two MPC mirrors M1 and M2 are separated by 82.4 cm. The circular pattern of equally spaced five beam spots on each mirror is observed where the beam makes 20 round trip passes between the mirrors (Fig. 2.2). I choose these parameters because the self-amplitude modulation (SAM) associated with KLM is maximized when the effective lengths of the

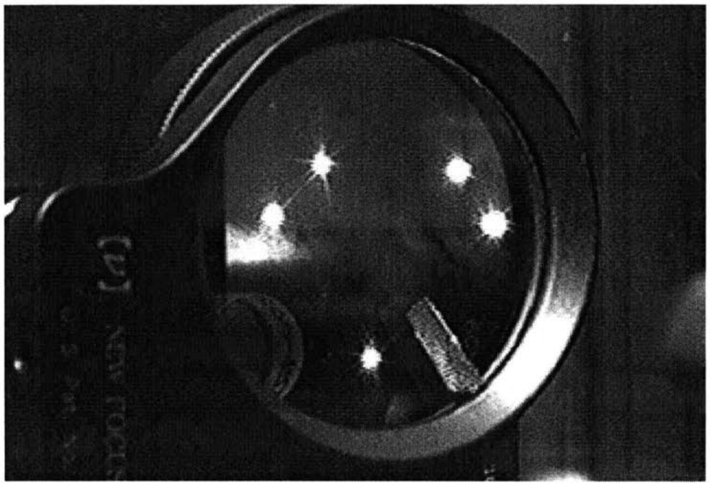

Figure 2.2: 5 reflections per each mirror in a 15 MHz laser are shown in a single path.

two cavity arms are approximately equal. At the same time, an intermediate number of passes is chosen so that reflection losses would not be excessive. In long lasers, dispersion from air can be significant and should be compensated to generate fs pulses. I calculate the dispersion of air at 800 nm to be 18 fs^2/m so that the round trip dispersion from air is 360 fs^2 [50]. The dispersion is compensated by increasing the prism separation 18 cm longer than would be used in a standard KLM laser with this crystal length.

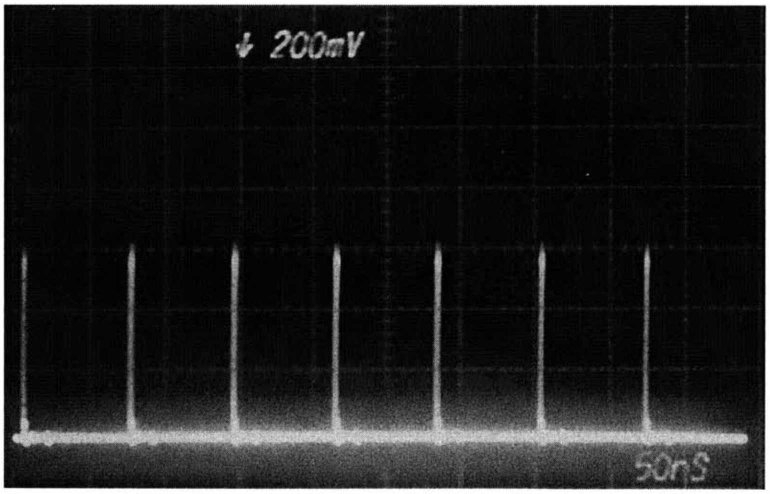

Figure 2.3: Mode-locked laser pulse train of 15 MHz repetition rate or 68 ns pulse separation at 50 ns/div.

Figure 2.3 shows a fast-photodiode trace of the mode-locked laser pulse train of 15 MHz repetition rate or 68 ns pulse separation. Pulse duration is measured by a collinear interferometric autocorrelator that has 200 μm thick KDP crystal. At 4.8 W pump power, I obtain 170 mW average output power and 16.5 fs (Fig 2.4(a)) nearly transform limited pulse duration centered at 806 nm by external prism compensation. The corresponding bandwidth of the pulse is 42 nm (Fig 2.4(b)), and is measured by optical multichannel analyzer (EG&G Princeton Research). The peak power of the pulses is approximately 0.7 MW out of an 11m long laser. It is interesting to note that the starting behavior of KLM and the stable KLM region of the long resonator laser slightly changes from the 100 MHz laser even though a unity q transformation is achieved. This can be explained by the strong self-phase modulation (SPM) and self-focusing effects resulting from high intensity pulses. To increase peak power or reduce pulse duration without generating multiple pulse instabilities, I concentrate on cavity alignment to avoid the saturation of SAM by optimizing the position of a gain medium theoretically and experimentally. Multiple pulse instabilities can be strongly quenched further by setting the laser cavity so that it has a reduced SAM for a given intensity or by decreasing intracavity peak power, however this makes starting KLM more difficult. Hence without separating the starting mechanism from continuously mode-locked operation, a several MW pulse peak power would not be obtained.

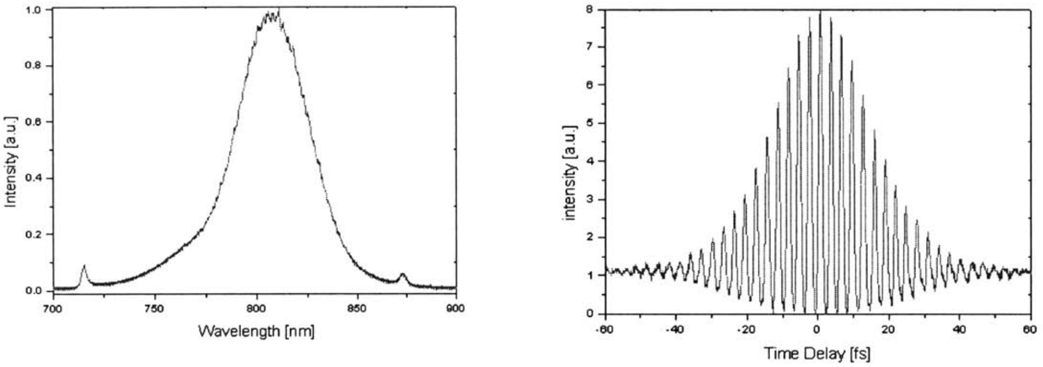

Figure 2.4: (a) Collinear interferometric autocorrelation trace showing a pulse duration of 16.5 fs assuming a sech^2(t) intensity profile, and (b) associated spectrum band width of 42 nm from the KLM Ti:Al_2O_3 laser.

2.4 7 MHz, High Intensity KLM Laser with Multiple Pass Cavity

Mode-locking is achieved at 7 MHz repetition rate where the two MPC mirrors M1 and M2 are separated by 148.2 cm. The circular pattern of equally spaced six beam spots on each mirror is observed where the beam makes 24 round trip passes between the mirrors.

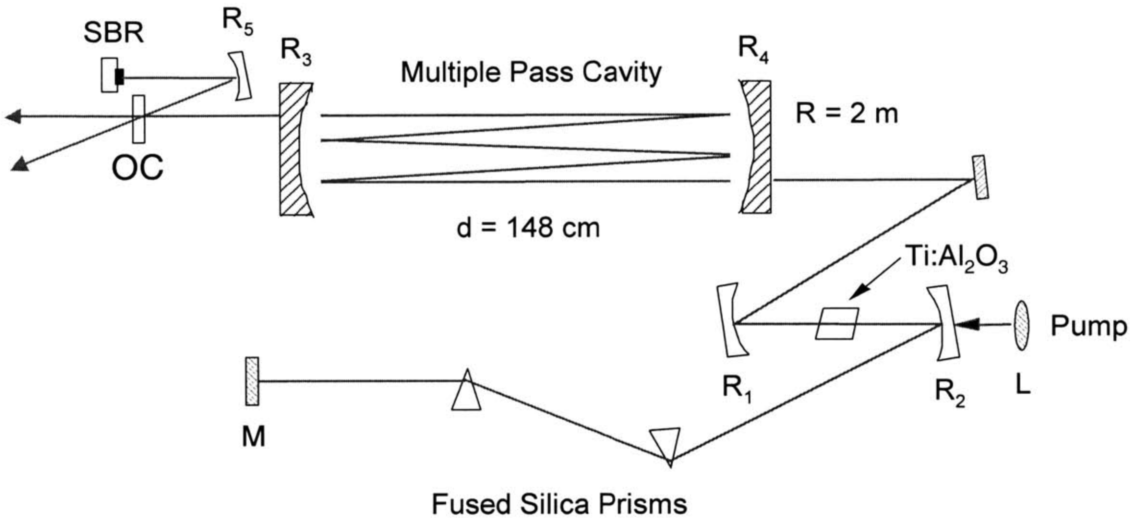

Figure 2.5: Ti:Sapphire laser schematic with a pair of multiple pass cavity mirrors: R_1, R_2, 10 cm radius of curvature mirrors; R_3, R_4, 2" diameter MPC mirrors with 2 m radius of curvature (CVI); R_5, 20 cm radius of curvature; L, 12.5 cm focal length pump beam focusing lens; OC, 3.5 % 12.5mm thick output coupler.

The dispersion of 3 mm long Ti:Sapphire crystal and 21 m long resonator which has around 400 fs^2 air dispersion is compensated by fused silica prism pair separated by the distance 75 cm. The output coupler is positioned next to a saturable Bragg reflector (SBR), which has two output beams from the output coupler of 2×3.5%, as shown in Fig. 2.4.

The difficulty in operating the laser at low repetition rates comes from the high intracavity pulse energies which overdrive the nonlinearities and lead to multiple pulsing instabilities. In order to reduce multiple pulse instabilities, the laser must be operated in a regime with a lower SAM nonlinearity, which makes the mode locking more difficult to start. This problem can be addressed by decoupling the starting mechanism for KLM for steady state mode-locked operation. Thus, to assist starting and stabilize the laser against multiple pulsing, the SBR is incorporated in the laser. The structure of the SBR consists of 30 high-low pairs of AlAs/

$Al_{0.15}Ga_{0.85}As$ quarter-wave dielectric stack grown by molecular beam epitaxy and a single GaAs quantum well. The single 10 nm QW contributes saturable absorption between 0 and 2%, and the saturation intensity depends on the position of the SBR. The SBR is essential to obtain stable mode locking operation with these long cavity lengths. The reflectivity is 99.5% over 80 nm stop bandwidth centered at 800 nm, and the SBR is designed and fabricated by Wayne Knox in Lucent Technologies [51].

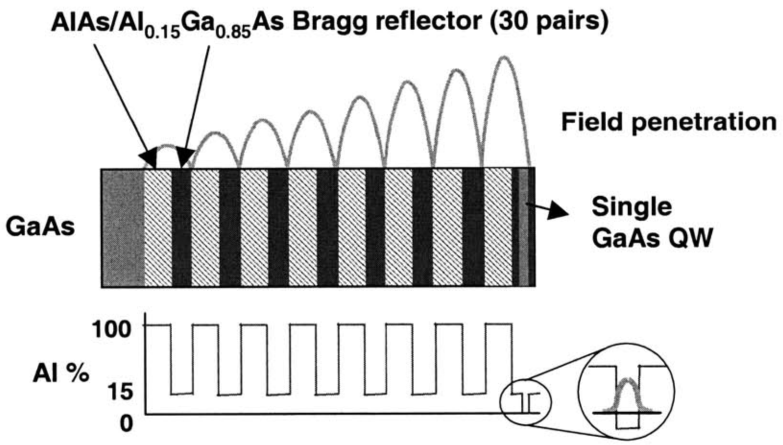

Figure 2.6: (a) The low loss SBR structure is made with high and low index layers of AlAs/AlGaAs reflector and GaAs quantum well where the electric field is shown in different positions.

Femtosecond pump-probe measurements are performed at 806 nm center wavelength and 41 nm bandwidth with ~ 10 fs pulse excitation to characterize the SBR, with the pump power of 110 mW and probe power of 100 mW. From the trace shown in Fig 2.7, I obtain the phase relaxation time of 50 fs and the energy relaxation time of 533 fs. Figure 2.8 shows a fast-photodiode trace of the mode-locked laser pulse train of 7.2 MHz repetition rate or 139 ns pulse separation.

At 6.5 W pump power, I obtain 150 mW total output power from two output couplings and 21 nJ total energy. Output power splitting ratio before and after the output coupler is almost 1:1. I measure 23.5 fs nearly transform limited pulse duration centered at 821 nm with the bandwidth of 31 nm, as shown in Fig. 2.9. Thus, the peak power would be 0.9 MW, if there were a single beam-out through the output coupler.

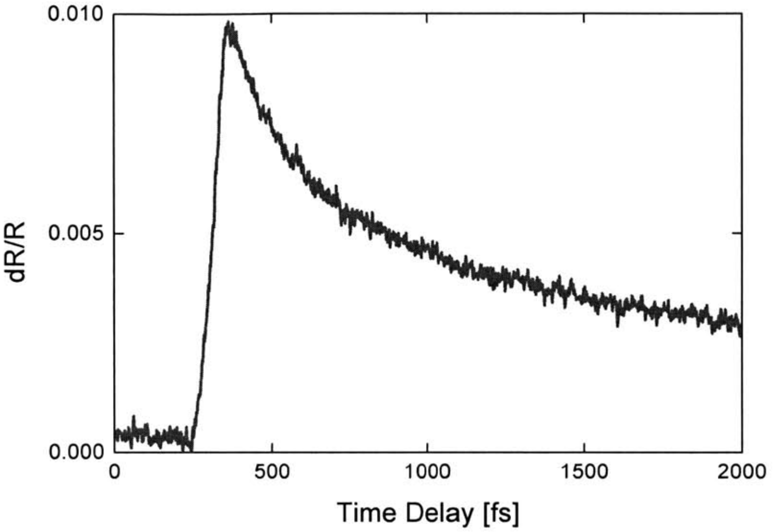

Figure 2.7: Pump-probe trace for the SBR with 30 μm spot size, excited by a 10 fs, 806 nm Ti:Sapphire laser.

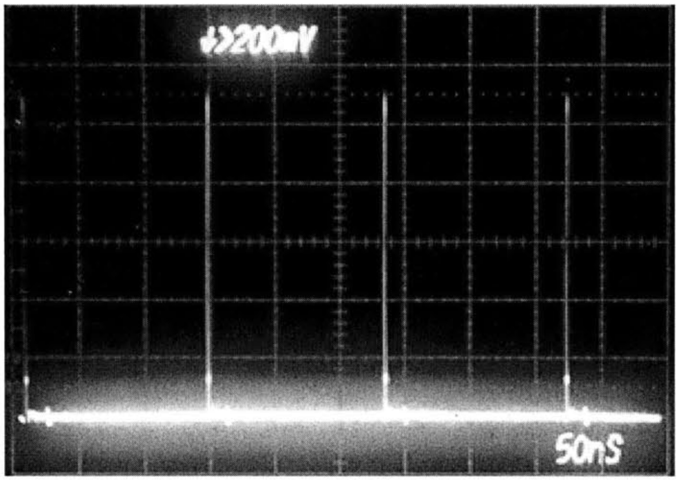

Figure 2.8: Mode-locked laser pulse train of 7.2 MHz repetition rate or 139 ns pulse separation.

A 5 MHz repetition rate laser is made with more reflections on the MPC mirrors, 1.61 m separation of MPC, and 110 cm separation of prisms, using the same schematics of Fig. 2.5. The picture in Fig. 2.10 shows a circular beam spot pattern at a 5 MHz laser which has 8 reflections per mirror single pass instead of six reflections per mirror in the 7 MHz laser. Hence, there are 32 reflections per round trip. Further investigation enables the use of a

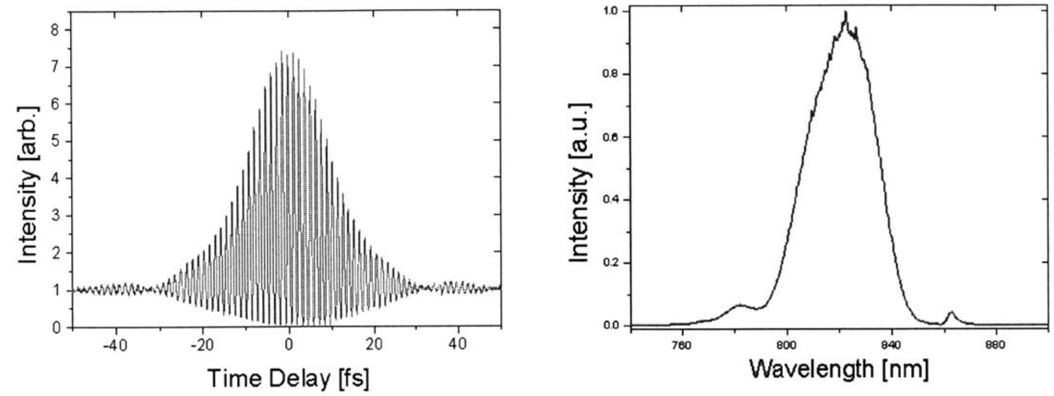

(a) (b)

Figure 2.9: For 7.2 MHz Ti:Sapphire laser; (a) Collinear interferometric autocorrelation trace showing a pulse duration of 23.5 fs assuming a $\mathrm{sech}^2(t)$ intensity profile; (b) associated spectrum band width of 31 nm.

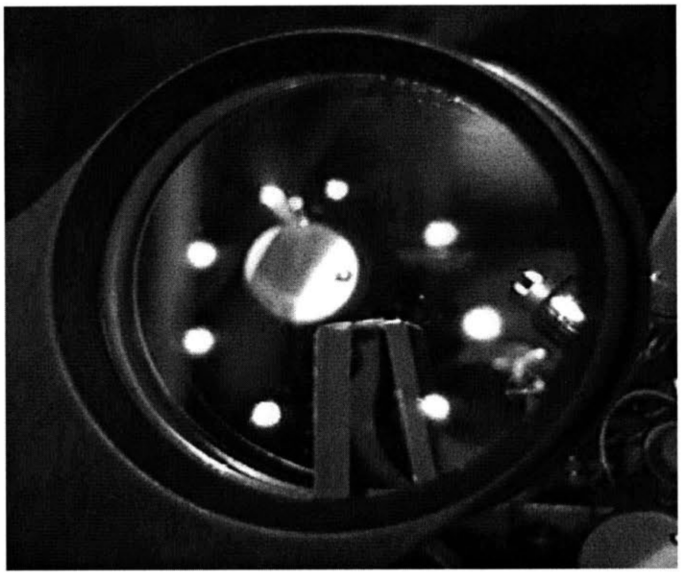

Figure 2.10: 8 reflections per each mirror in a 5 MHz laser are shown in a single path.

2×14% output coupling mirror, which can provide high slope efficiency 16.7 % of the laser, shown in Fig. 2.11.

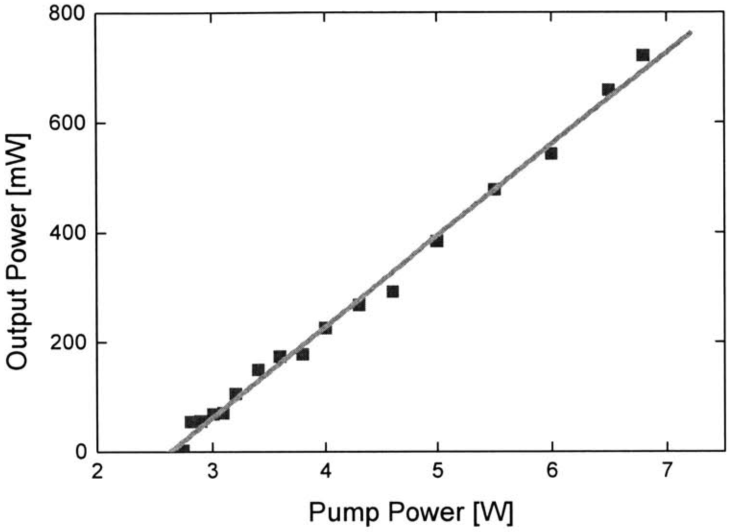

Figure 2.11: Slope efficiency of a 5 MHz laser is measured: measurement (dot); linear fit (solid).

2.5 4 MHz, High Intensity KLM Laser with Multiple Pass Cavity

A novel MPC is designed to further decrease the laser repetition rate using half-degenerate optical cavity where the incident beam to MPC exits through the same spot at the front MPC mirror, as shown in Fig. 2.12. This new scheme is especially useful, because a laser beam alignment very flexible and reliable, without aligning the second MPC mirror that is very time-consuming and cumbersome. As a result, the laser repetition rate is successfully reduced to as low as 4 MHz by a unity q parameter transformation of a Gaussian beam by use of the half-degenerate MPC [52].

Figure 2.12 shows a schematic diagram of the long cavity laser. The Ti:Sapphire crystal is a 3 mm long, Brewster-cut crystal with high Ti doping of $\alpha = 3.87\ \mathrm{cm}^{-1}$. Focusing mirrors with a 10 cm radius of curvature are used. Dispersion from all of the intracavity elements is compensated by a pair of fused silica prisms separated by a distance of 145 cm, producing a negative dispersion of up to - 3200 fs^2. Mode-locking was achieved at 4 MHz repetition rate where the two MPC mirrors M_1 and M_2 are separated by 129.08 cm. The beam bounces in a circular pattern of equally spaced 13 spots on one mirror, M_1, and of 12 spots on the other mirror, M_2, corresponding to 50 round trips in the MPCs within one cavity roundtrip. The overall ABCD matrix, defined from a reference plane at the input mirror M_2 of the MPC, is

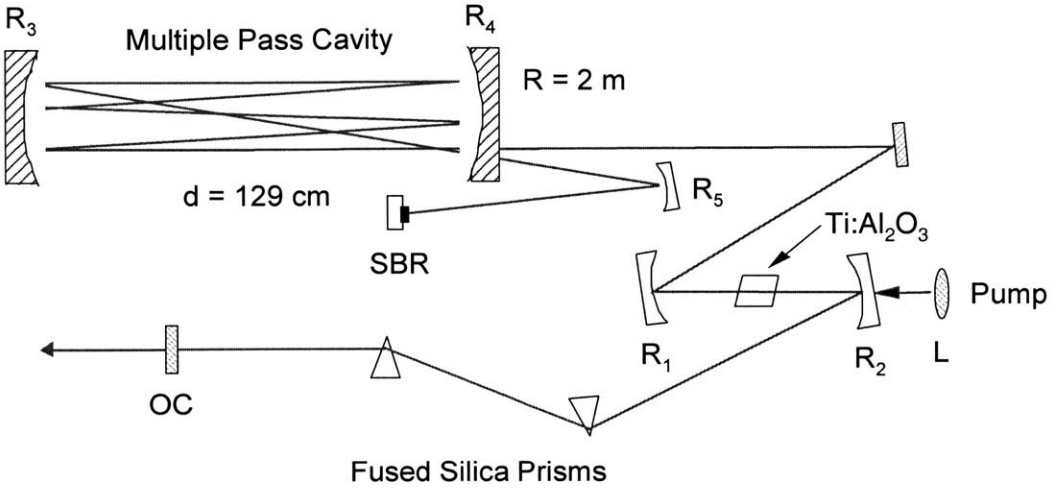

Figure 2.12: $Ti:Al_2O_3$ laser schematic with a pair of multiple pass cavity mirrors: R_1, R_2, 10 cm radius of curvature mirrors (Spectra-physics); R_3, R_4, 2" diameter MPC mirrors with 2 m radius of curvature (Spectra-physics); R_5, 50 cm radius of curvature mirrors (Newport); L, 6.3 cm focal length pump beam focusing lens; OC, 27% transmission, 1/2" thick output coupler (Spectra-Physics).

equivalent to one free space propagation, to the mirror M_1, followed by one mirror reflection from M_1, and one free space propagation, from M_1 back to the reference plane. The output beam from the MPC is focused by a mirror with a 50 cm radius of curvature, R_2, onto the SBR, which retro-reflects the beam. The separation between the focusing mirror and the SBR can be adjusted to cancel the propagation effects in the MPC, achieving an overall unity transformation of the Gaussian beam.

Commercially available, typical mirrors can produce high total losses from the large numbers of reflections in the MPC. In order to reduce the total loss of the MPC, low loss TaO_2/ SiO_2 quarter-wave mirrors are designed by Franz X. Kärtner and manufactured by Richard Boggy in Spectra Physics. The reflectance of each MPC mirror is approximately 99.95%, resulting in an overall parasitic loss of less than 3% in the 4 MHz MPC. Using a white light interferometer, the group delay dispersion in these mirrors is measured to be less than 5 fs^2 per bounce at 800 nm, as shown in Fig 2.13. The round trip dispersion of 50 bounces from the MPC mirrors and 75 m of air are compensated by a prism pair with large intracavity prism separation. The high output coupling of 27 % lowers the intracavity pulse energy, while achieving high output pulse energy.

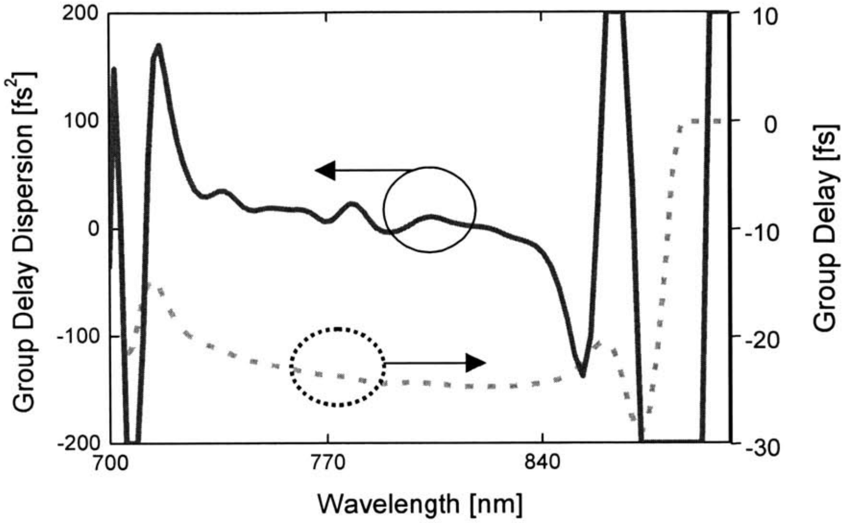

Figure 2.13: Group delay (dot) and group delay dispersion (solid) is measured with newly designed MPC mirrors.

The SBR is essential to obtain stable mode locking operation in this very low repetition rate, as explained in Sec. 2.4. Mode locking is initiated by slightly moving the curved mirror R_2 which focuses the beam on the SBR or by translating one of the intracavity prisms. Stable pulses are obtained at 4 MHz repetition rate and the KLM operating region changes only slightly from the equivalent 100 MHz laser. The cavity alignment is relatively insensitive to changes in the separation of the MPC mirrors. By mode-locking in the standard regime, with a net negative intracavity dispersion of approximately -340 fs^2, I obtain stable 55 fs pulses centered at 790 nm with an average power of 192 mW at 4.9 W pump power (Fig. 2.14(a), 2.14(b)). This corresponds to pulse energies of 48 nJ and peak powers of 0.9 MW. The mode-locked laser pulse train has a period of 250 ns between pulses as shown a fast photodiode oscilloscope trace (Fig. 2.15).

Using positive dispersion mode-locking with a net intracavity dispersion of approximately +390 fs^2, I obtain 435 mW average output power or pulse energies of 120 nJ at 6.2 W pump power. The pulses are stable but highly chirped with a pulse duration of 0.8 ps and wavelengths centered at 777 nm (Fig. 2.14(d)). These chirped pulses are compressed using an

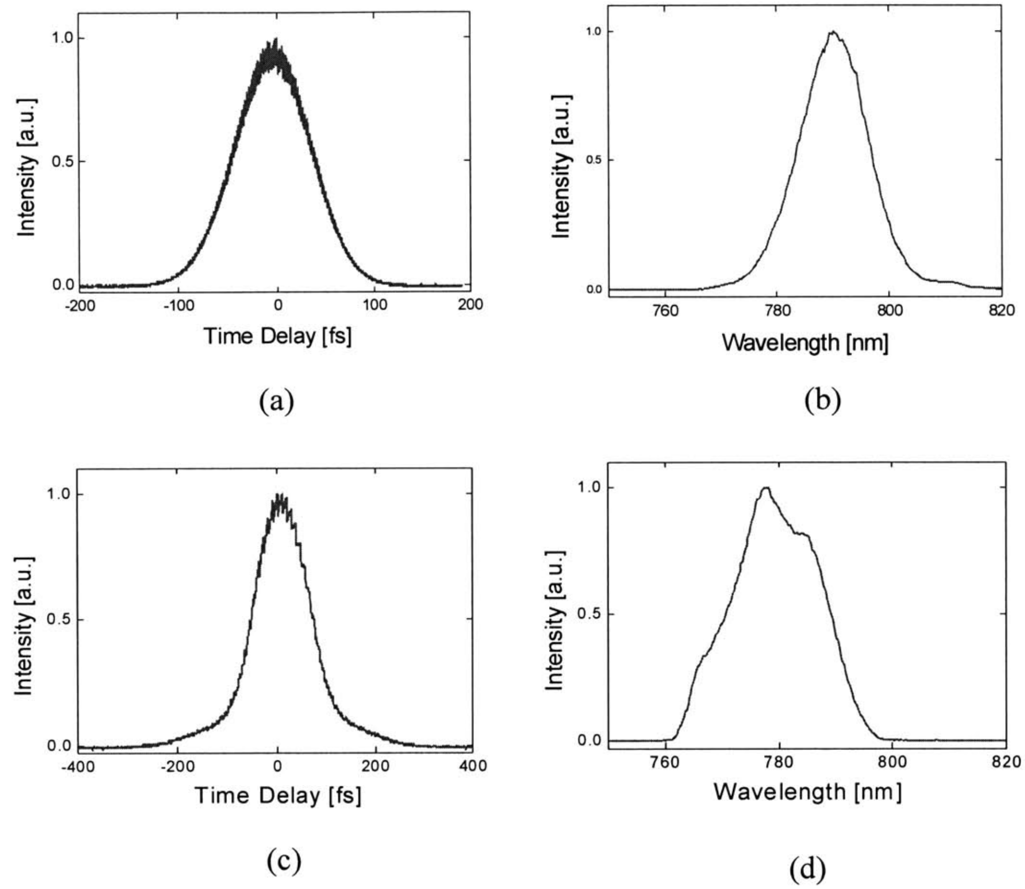

(a) (b)

(c) (d)

Figure 2.14: (a) Intensity autocorrelation trace showing a pulse duration of 55 fs assuming a sech^2(t) intensity profile, (b) associated spectrum bandwidth of 14 nm from net negative dispersion KLM operation, (c) a pulse duration of 80 fs assuming a sech^2(t) intensity profile, (d) associated spectrum bandwidth of 19 nm from net positive dispersion KLM operation.

external prism pair compressor with two SF10 prisms separated by 145 cm in a double pass configuration. The compressed pulse duration is 80 fs, and after losses in the prism compressor, the pulse energy is 100 nJ, corresponding to a peak power of 1.25 MW (Fig 2.14(c)). The bandwidth of the pulses is 19 nm, so there is residual uncompensated chirp and the pulses are 2.4 times transform-limit, assuming a sech^2(t) pulse shape (Fig. 2.14(d)). The stability of positive dispersion modelocking is comparable to negative dispersion modelocking in terms of the ability to start and sustain short pulse operation. For high energy pulses, positive dispersion modelocking is more stable against the formation of multiple pulses.

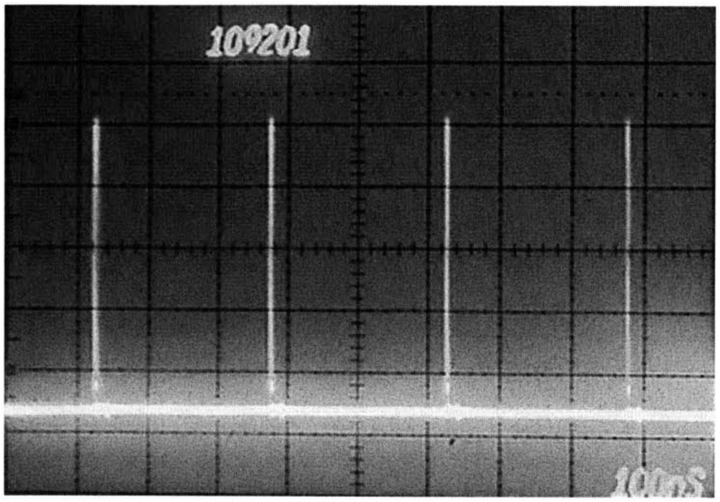

Figure 2.15: Oscilloscope trace of fast photodiode showing mode-locked laser pulse train of 4 MHz repetition rate or 250 ns pulse separation.

Negative dispersion mode-locking, in general, generates nearly transform-limited pulses with good stability. SPM and negative dispersion produce a soliton-like pulse shaping mechanism. However, these short pulses have high pulse intensities, which produce high nonlinearities causing instabilities and multiple pulse operation. Above 4.9 W pump power, the laser starts to generate excess amplitude noise of ~ 15 dB as measured by an RF spectrum analyzer (Advantest R3265). There is a significant increase in the pulse pedestal measured using background free intensity autocorrelation. With increasing pump power, the height of the autocorrelation pedestal increases. The pulse duration and the associated spectrum do not depend on whether the laser generates single pulses or multiple pulses. The time-bandwidth product of the pulses in the net negative dispersion regime is approximately 1.2 times the transform-limit of a $\text{sech}^2(t)$ intensity profile. This phenomenon may suggest a Gaussian temporal profile predicted for passive mode-locking with two saturable absorbers (KLM and the SBR) [53]. Or a higher order nonlinear effect may explain a pulse shaping mechanism of dispersion-managed solitons [54], as comes next.

If KLM lasers are operated with net positive intracavity dispersion, the pulses become positively chirped and long. These long pulse durations can support higher pulse energies with correspondingly lower intensities and nonlinearities. Although the chirped pulses have durations of several picoseconds, femtosecond pulses can be obtained using an external prism compressor. In positive dispersion operation, gain bandwidth limits pulse shortening by attenuating the wings of the chirped pulse. Thus the pulse can have a nonlinear chirp. In addition, the higher order dispersion produced by the SF10 prisms can limit pulse compression. For these reasons transform limited pulses could not be achieved using the prism compressor alone. Positive dispersion KLM will be able to generate transform-limited pulses if chirped mirrors, prism compressors, or better methods of controlling group delay dispersion are designed to precisely compensate for the complicated nonlinear chirp.

2.6 Analytic Theory of Quintic Complex Master Equation

I develop a new soliton theory for high intensity fs pulses, because a standard soliton theory does not explain appropriately pulses with high intensities. In this new formulation, I focus on extending a fast saturable absorption in a complex domain to the quintic order, so as to include high order saturable nonlinearities. The periodic evolution of SAM, SPM, and dispersion influences ultrashort pulse shaping, and gain and loss affect stablity of such short pulses, which is, i.e., dispersion managed-modelocking [54][55]. The exact solution of optical solitons from the high intensity laser resonator is derived from the quintic approximation of the fast saturable absorber or SAM in the master equation of Ginzburg-Landau equation. The pulse amplitude is denoted by a(T, t), and $|a(T, t)|^2$ is the instantaneous or peak power in the pulse, where T is the macroscopic time parameter for a pulse traveling in a resonator, and t is the instantaneous, microscopic time paramter within a pulse. The ultrashort pulses are generated by the periodic evolution per pass of pulse shaping mechanisms enumerated in Eq. (2.5) [56].

$$(\text{Gain - Loss - SAM + GDD- SPM})\ a(T, t) = 0 \tag{2.5}$$

In this formulation, SPM expands to the quintic order as

$$SPM \equiv j\frac{2\pi d}{\lambda}\sum_{k=0}^{\infty} n_{2k}\frac{|a(T,t)|^{2k}}{A_{eff}^{k}} \approx j\Psi + j\delta|a(T,t)|^2 + j\nu|a(T,t)|^4 \tag{2.6}$$

where d is the length of a Kerr or gain medium, λ is the wavelength of the light, Ψ is the linear phase shift, $\delta|a|^2$ and $\nu|a|^4$ are the equivalent 3th-order and 5th-order SPM, respectively. SAM expands to the quintic order as

$$SAM \equiv \frac{S_o}{1+\frac{|a(T,t)|^2}{P_s}} = S_o \sum_{k=0}^{\infty} (-1)^k \frac{|a(T,t)|^{2k}}{P_s^k} \approx S_o(1-\gamma|a(T,t)|^2+\mu|a(T,t)|^4) \quad (2.7)$$

where S_o is the unsaturable loss, P_s is the saturation power, $\gamma|a|^2$ and $\mu|a|^4$ are the equivalent 3th-order and 5th-order saturable absorber, respectively. The GDD is group delay dispersion D, gain per pass is g, and the linear loss is l_o. Summaring all terms using Eq. (2.5) through Eq. (2.7) lead to the quintic complex master equation for steady state mode-locking that is written as

$$\left[\left(\frac{g}{\Omega_g^2}+jD\right)\frac{\partial^2}{\partial t^2}-(l-g)+(\gamma-i\delta)|a(T,t)|^2-(\mu+i\nu)|a(T,t)|^4\right]a(T,t) \quad (2.8)$$

$$= T_R\frac{\partial}{\partial T}a(T,t) = j\Psi a(T,t)$$

where l represents the total linear loss per pass, Ω_g is the gain bandwidth, and T_R is the cavity roundtrip time.

The t dependent nonlinear differential equation is symbolized as a different operator L, so the Eq. (2.8) can be simply expressed as

$$La(T,t) = T_R\frac{\partial}{\partial T}a(T,t) = j\Psi a(T,t) \quad (2.9)$$

where

$$L = \left(\frac{g}{\Omega_g^2}+jD\right)\frac{\partial^2}{\partial t^2}-(l-g)+(\gamma-i\delta)|a(T,t)|^2-(\mu+i\nu)|a(T,t)|^4 \quad (2.10)$$

Using the separation of variables of T and t,

$$a(T,t) = f(t)h(T) \quad (2.11)$$

The Eq. (2.9) reduces to

$$\frac{Lf(t)}{f(t)} = \frac{T_R\frac{\partial}{\partial T}a(T,t)}{h(T)} = j\Psi \quad (2.12)$$

The real part of Eq. (2.10) is represented by, when a substitution is made with $\dot{a}(t) = b(t)$ and so ä(t) = $\dot{b}(t) = \frac{1}{2}\frac{d}{da(t)}b(t)^2$

$$\frac{g}{2\Omega_g^{\,2}}\frac{d}{da(t)}b(t)^2 = (l-g)a(t)+\gamma a(t)^3-\mu a(t)^5 \tag{2.13}$$

By taking the explicit integration of a(t) in time t, Eq. (2.13) equals to

$$\frac{g}{\Omega_g^{\,2}}\frac{d}{dt}a(t)^2 = (l-g)a(t)^2+\frac{\gamma}{2}a(t)^4-\frac{\mu}{3}a(t)^6 \tag{2.14}$$

And taking the implicit integration of a(t) leads Eq. (2.14) to

$$t-t_o = \frac{\sqrt{g}}{\Omega_g}\int_{a_o}^{a(t)}\frac{da(t)}{\sqrt{(l-g)a(t)^2+\frac{\gamma}{2}a(t)^4-\frac{\mu}{3}a(t)^6}} \tag{2.15}$$

Since the right hand side of Eq. (2.15) is integrable, the analytical solution is given by changing the representation of the integration into the explicit form, using the initial condition of $\lim_{t_o\to\pm\infty} a(t) = 0$.

$$a(t) = A\frac{1}{\sqrt{\cosh(t/\tau_p)+B}} \tag{2.16}$$

where $A = \frac{(g-l)^{1/2}}{\left(\frac{1}{16}\gamma^2+\frac{1}{3}(g-l)\mu\right)^{1/4}}$, $B = \frac{1}{\sqrt{1+\frac{16}{3}\frac{\mu}{\gamma^2}(g-l)}}$, and $\tau_p = \frac{1}{2\Omega}\sqrt{\frac{g}{l-g}}$.

The t dependent part of the complex Eq. (2.6) is solved, based on Eq. (2.13) as

$$f(t) = A\left(\frac{1}{\sqrt{\cosh(2t/\tau_p)+B}}\right)^{1+j\beta} \tag{2.17}$$

which is close to the 3th-order solution of the $sech(t/\tau_p)^{1+j\beta}$ that is the temporal shape of low intensity soliton pulses. I solve Eq. (2.8) independently of the previous work on a quintic order Ginzbug-Landau equation by Marcq, et al [57]. One group solved this equation to derive a solution with pulse like solitons [58]. The T dependent part with unit amplitude is solved as

$$h(T) = e^{j\Psi T_R} \tag{2.18}$$

Hence, the amplitude of high intensity solitary pulses is given by

$$a(t) = Ae^{j\Psi T_R \cdot \left(\frac{1+j\beta}{2}\right)\ln(\cosh(2t/\tau_p) + B)} \tag{2.19}$$

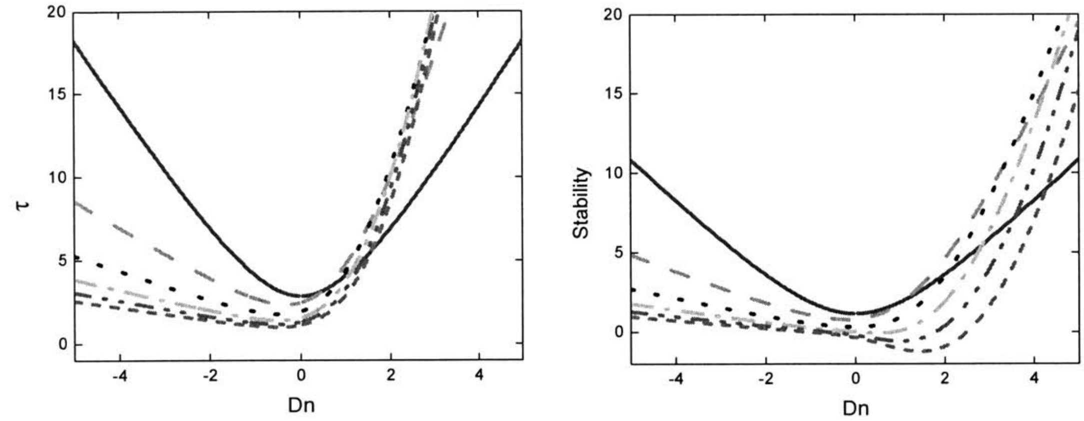

(a) (b)

Figure 2.16: For constant pulse parameters of $\gamma = 1$, $g = 1.15$, $l = 2.8$, $\Omega_g = 1$, $\mu = 2/3$, and the constant normalized energy of 1, with different 3th-order SPM δ of zero (solid); 1 (dot), 2 (dash), 3 (dash-dot), 4 (dash-dot-dot), 5 (short-dash); (a) normalized pulse width (b) stability of pulses.

Based on the derivation in Appendix A and Eq (2.17), various normalized parameters can be analyzed including bandwidth, pulse width, chirp, stability, 5th-order SPM and SAM papameters. For the constant 3th-order SAM γ, constant loss l, gain g, and the 5th-order SAM μ, Fig. 2.16(a) plots the normalized pulse width τ_p versus the normalized dispersion $D_n = (\Omega_g^2/g)\,D$, similar to the study for the 3th-order in [56]. Fig 2.16(b) plots the stability parameter $(l-g)\tau^2\Omega_g^2$. As the SPM ν increases, the pulses are not only driven shorter in the negative dispersion regime, but also more stable in the wide range of dispersion except in some positive dispersion.

For the constant 3th-order SPM ν, Fig. 2.17(a) plots the normalized pulse width τ_p versus the normalized dispersion, and Fig 2.17(b) plots the stability parameter. As the SAM μ

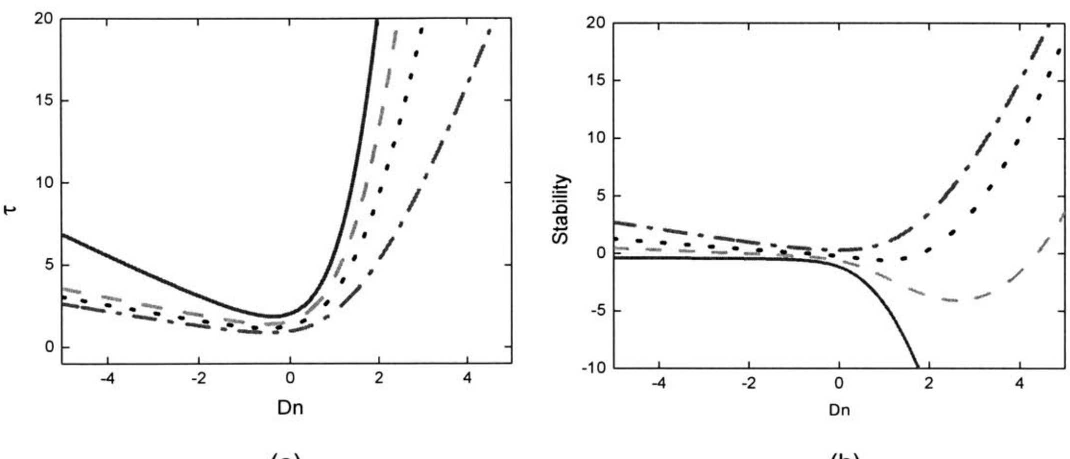

(a) (b)

Figure 2.17: For constant pulse parameters of $\delta = 4$, $g = 1.15$, $l = 2.8$, $\Omega_g = 1$, $\mu = 2/3$, and the constant normalized energy of 1, with different 3thorder SAM μ of zero (solid); 0.5 (dot), 1 (dash), 2 (dash-dot); (a) normalized pulse width (b) stability of pulses.

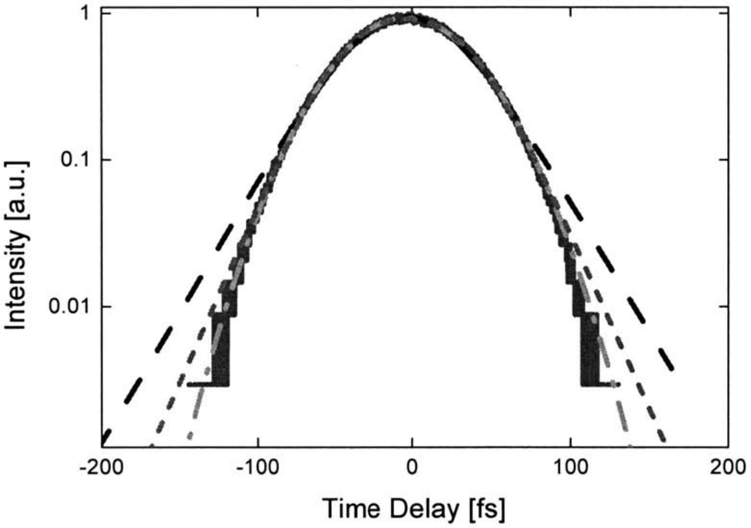

Figure 2.18: Different fitting functions to a measured autocorrelation function: autocorrelation (solid line); $\mathrm{sech}(t/\tau_p)^2$ (dash); Gaussian (dash-dot); modified sech (short dash).

increases, the pulse becomes shorter in time and more stable, because the saturable loss of SAM reduces low intensity wings in pulses and balances the effect of spectral broadening of SPM.

This new extended solution of a modified-sech is better fitted to autocorrelation measurements of high intensity pulses from a low repetition rate Kerr lens mode-locked laser than the sech-shape or Gaussian pulse (Fig 2.18). By comparisons with three different fittings to pulse envelope functions, more exact pulse width is determined to be 60 fs, which is wider than the sech-fit of 55 fs, as summarized in Table 2.2.

TABLE 2.2: Comparisons of pulse widths that correspond to different pulse envelope functions. As a result, the pulse width is 60 fs instead of 55 fs.

Field envelope	Intensity profile	τ_{FHWM}	τ_{ac}/τ_p	τ_p [fs]
Gaussian	$\mathrm{Exp}(-2t^2/\tau_G^2)$	$1.177\ \tau_G$	1.414	60.2
Sech	$\mathrm{sech}(t/\tau_s)^2$	$1.763\ \tau_s$	1.543	55
Modified Sech	$1/[\cosh(2t/\tau_m)+B]$	$\cosh^{-1}[2+B]\tau_m$	1.403	60.6

2.7 Conclusion

Mode-locked operation of a KLM $Ti:Al_2O_3$ laser is demonstrated at repetition rates of 15 to 4 MHz using a novel MPC and an SBR. For 15 MHz lasers, I obtain 170 mW average output power and 11.3 nJ pulse energy at 4.8 W pump power, with 16.5 fs nearly transform limited pulse duration centered at 806 nm and the bandwidth of 42 nm. The peak power of the pulses is approximately 0.7 MW out of a 10 m long cavity. For 7 MHz lasers, I obtain 150 mW total output power from two output couplings and 21 nJ total energy at 6.5 W pump power with 23.5 fs nearly transform limited pulse duration centered at 821 nm and the bandwidth of 31 nm. The peak power would be 0.9 MW from a 21 m long cavity, if there were a single beam-out through the output coupler instead two outputs. For 4 MHz lasers, I obtain 55 fs pulses with 48 nJ pulse energy when operating in the net negative dispersion regime and 80 fs pulses with 100 nJ pulse energy when operating in the net positive dispersion regime. Without compensating the positive chirp, the pulse energy is 120 nJ, and the pulse duration is 0.8 ps.

This unprecedented low repetition rate of femtosecond lasers suggests new approaches for achieving several MHz repetition rates and MW level peak powers. The reduction in pulse repetition rate for a given pulse peak intensity should make it possible to study ultrafast nonlinear phenomena more easily by reducing parasitic thermal and excitation effects. The low repetition rate laser is also a cost effective approach for generating high pulse energies useful for materials processing and nonlinear studies. In other work, 36 nJ pulses at a 15.5 MHz repetition rate have been generated using a 1:1 telescope as an optical delay line to extend the cavity; with a similar scheme, 23 nJ pulses at a 30 MHz repetition rate and pulse duration of 7 fs have been recently demonstrated [59]. I analytically solve a higher order nonlinear Schrödinger equation to analyze the higher order effect of saturable loss, SAM and spectral broadening of SPM, where I show that the modified Sech is better fit to autocorrelation than conventional Sech or Gaussian fits. The new pulse shape of the modified sech might contribute to the further study of solition propagation in lasers and long haul communications using dispersion-managed solitons [60].

In further studies I will investigate the possibility of extending MPC laser designs to operate with repetition rates of less than 4 MHz. In this case, higher peak pulse intensities are expected and the laser cavity will have to operate with a reduced SAM nonlinearity in order to avoid multiple pulsing instability. Thus, the starting mechanism for KLM should be decoupled from steady state modelocked operation. Approaches such as saturable Bragg reflectors, semiconductor saturable absorber mirrors, or acousto-optic modulators will be investigated for starting modelocking. If higher pulse energies can be generated directly from the laser, then direct pulse compression after spectral broadening may become possible. In addition, it is interesting to consider reducing air dispersion in long cavity lengths by purging with an inert gas of He or Ne.

Chapter 3

Fabrication using High Intensity Ultrafast Lasers

3.1 Introduction

Femtosecond laser systems open up nonlinear micromachining of materials with a higher precision than using standard long pulse, nanosecond laser systems. The time scale of ultrashort laser pulses less than 1 ps is shorter than the relaxation time of electrons with the lattice. By using such ultrashort laser pulses, collateral damage to any type of material can be minimized so that micromachining is achieved by removing material faster than heat transfer into the surrounding material. The main mechanism of material removal is due to thermal/nonthermal ablation where the material is locally excited to near decomposition or melting/boiling. This ablation process is accompanied by softening, a strong thermal shock, or the breakdown of the material which results from the generation of very dense e-h plasmas. The advantages of using fs-laser pulses are:

(1) Less energy compared to ns-excitation while maintaining the same intensity is required to achieve the same amount of material removal.

(2) Multiphoton absorption enables small volume of structures to be excited.

(3) Thermal shock or damage to surrounding material is negligible.

(4) Nonlinear material processing can lead to novel device structures

The most commonly available laser systems for this process needs very intense, amplified femtosecond pulses from chirped-pulse amplifiers or regenerated amplifiers of which intensities are relevant for optical damage or ablation. Often the limiting factor of damage threshold for dielectrics is approximately a few TW/cm^2, with μJ pulse energies. It is interesting to note that the novel laser resonator without using amplifiers or any active devices, as explained in Chap. 2, can generate high enough intensities of several TW/cm^2. Hence, one of the most interesting applications of the high intensity laser beams from this novel resonator would be micromachining or microstructuring. Furthermore, three-dimensional optical memories using microexplosion with fs-pulses inside transparent dielectrics could replace a single layer of compact disks or digital versatile disks with high-capacity multi-layer format.

3.2 Laser Induced Ablation Mechanisms

3.2.1 Laser Induced Excitation and Relaxation

In a solid, optical excitations include the free-carrier generating processes of interband and intraband absorption, multi-photon absorption, free carrier absorption, impurity absorption, and avalanche ionization [61]. Relaxation processes that loose carrier energy and the number of carriers are Auger recombination, carrier-lattice collision, radiative/nonradiative carrier recombination, carrier diffusion, and heat conduction. In addition, localized states such as defects, impurities, and surface states would exist. Some of these excitations are schematically shown in Fig. 3.1.

The high intensity photons from femtosecond lasers on a solid target can induce direct bond breaking by nonthermal electronic excitation, resulting in surface material removal or ablation. The most common experiment has been done on transparent dielectric materials that have the wide bandgap of $h\nu < E_g$, using the generation of free electrons due to avalanche ionization or multi-photon ionization with the intensity above a few TW/cm^2.

Due to thermal excitation, the free carrier density N_o in intrinsic semiconductors at thermal equilibrium temperature T is given by

$$N_o(T) = 2\left(\frac{2\pi kT}{h^2}\right)^{3/2}(m_e{*}m_h{*})^{3/4}\exp\left(-\frac{E_g}{2kT}\right) \tag{3.1}$$

in which the temperature dependence of the bandgap needs to be considered.

For a solid state material, the carrier density after the laser irradiation can be described by

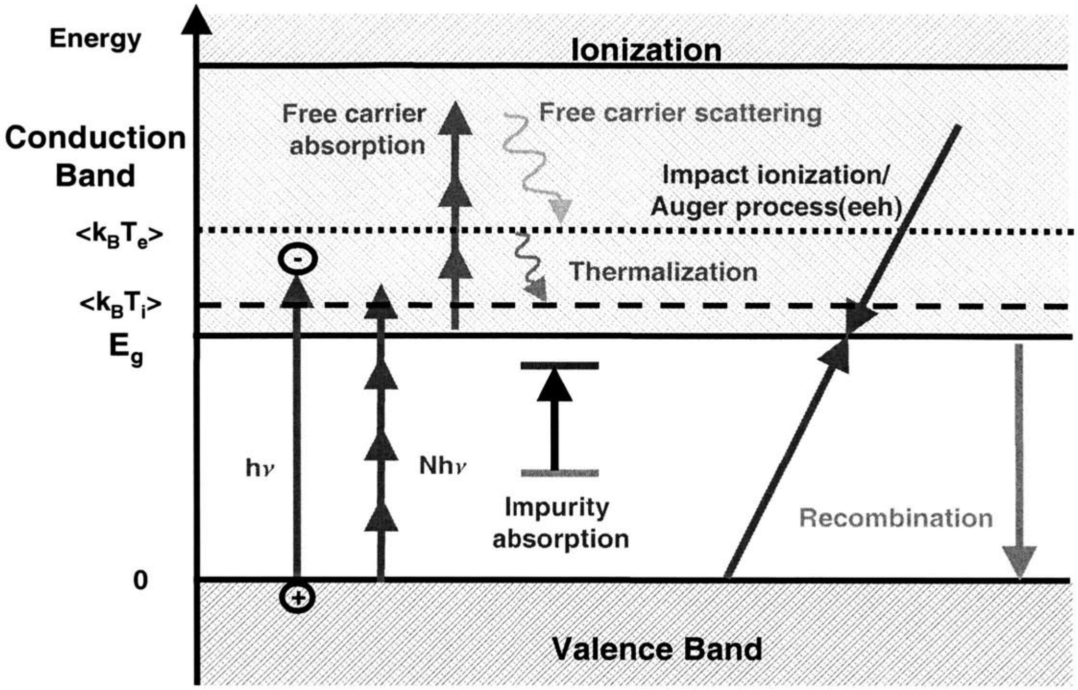
Energy
Ionization
Conduction Band
Free carrier absorption
Free carrier scattering
Impact ionization/ Auger process(eeh)
$<k_B T_e>$
Thermalization
$<k_B T_i>$
E_g
hν
Nhν
Impurity absorption
Recombination
0
Valence Band

Figure 3.1: Schematic diagram of various excitations and their relaxation mechanisms for electrons in a sold. The analogous diagram holds for holes.

$$R \equiv G - L \tag{3.2}$$

where R is the net carrier generation rate, G is the generation rate of carriers, and L is the loss rate of carriers.

The net rate of carrier generation is

$$R = \frac{\partial}{\partial t} N_c(\vec{r}, t) \tag{3.3}$$

The generation rate of carriers is described by interband absorption, avalanche ionization, and multiphoton absorption as [61]

$$G = \alpha(\nu)\frac{I(\vec{r}, t)}{h\nu} + \beta(\nu)N_c(\vec{r}, t) + \sigma_n(\nu)I(\vec{r}, t)^n \tag{3.4}$$

where $\alpha(\nu)$ is the linear absorption coefficient [cm^{-1}], $\beta(\nu)$ is the avalanche or impact ionization coefficient [cm^2/J], and $\sigma_n(\nu)$ is the multiphoton absorption coefficient in n^{th} order. The loss rate of carriers is represented by recombination and carrier diffusion as

$$L = \frac{N_c(\vec{r}, t) - N_o(T)}{\tau_{rec}} - \nabla D_c(\vec{r}, t)\nabla_c N(\vec{r}, t) \tag{3.5}$$

where τ_{rec} is relaxation time for recombination, D_c is carrier diffusion constant, and at room temperature, the carrier density is $N_o(\vec{r}, t)$ in Eq. (3.1). The τ_r is the relaxation time for radiative recombination which can be related to B by

$$\frac{1}{\tau_r} = B(N_c(\vec{r}, t) - N_o(T)) \tag{3.6}$$

The relaxation time for nonradiative recombination τ_{nr} is represented by the Auger recombination constant C which is dominant in most semiconductors. The relaxation times have the relation of $\frac{1}{\tau_{rec}} = \frac{1}{\tau_r} + \frac{1}{\tau_{nr}}$. The Auger recombination is a three-body process that needs a third carrier of electron or hole by

$$\frac{1}{\tau_{nr}} = C(N_c(\vec{r}, t) - N_o(T))^2 \tag{3.7}$$

In this carrier balance equation, free carrier absorption and carrier-lattice heating are not included because these two effects only change carrier energy. However, should the carrier energy be considered, these two effects will be included in Eq. (3.4) through Eq. (3.7). Thus, the resulting net carrier density follows

$$\begin{aligned} \frac{\partial}{\partial t}N_c(\vec{r}, t) = {} & \alpha(\nu)\frac{I(\vec{r}, t)}{h\nu} + \beta(\nu)N_c(\vec{r}, t) + \sigma_n(\nu)I(\vec{r}, t)^n + \nabla D_c(\vec{r}, t)\nabla_c N_c(\vec{r}, t) \\ & -(N_c(\vec{r}, t) - N_o(T))\left(\frac{1}{\tau_r} + \frac{1}{\tau_{nr}}\right) \end{aligned} \tag{3.8}$$

For dielectrics of wide bandgaps with $h\nu < E_g$, the first term of linear absorption in Eq. (3.8) goes to zero. For photo-excitation with less than 100 fs pulses, interactions except electron-electron collisions (10 fs) are too slow to alter the electron density N_c. This is, so called, nonthermal excitation. As a result, the fourth term of carrier diffusion in Eq. (3.8), due to slow interactions of electron-LO phonon (100 fs - 1 ps) and LO-LA phonon (10 ps - 1 ns), is neglected. In addition, the last term of radiative recombination (1 ns - 1 μs) and Auger recombination (1 ns) go to zero. Thus in fs-excitation, only avalanche ionization and multiphoton absorption can contribute to carrier generation but not to carrier loss. In such an ultrashort time, since massive ions or phonons cannot respond to the electric field of the incident light, the electron density is only considered [62]. Hence, the net carrier density change in time at fs-excitation reduces to

$$\frac{\partial}{\partial t}N_c(\vec{r}, t) = \beta(\nu, I(\vec{r}, t))N_c(\vec{r}, t) + \sigma_n(\nu)I(\vec{r}, t)^n \tag{3.9}$$

Furthermore, if the intensity of impinging photons is not high enough ($I <$ TW/cm^2), the second term of multiphoton absorption in Eq. (3.9) will be negligible.

3.2.2 Determination of Ablation Threshold

In optically transparent dielectrics, such as glasses, there is no linear absorption, as prescribed in Eq. (3.4). However, there are two nonlinear processes of avalanche ionization and multiphoton ionization if the laser intensity is high enough, which deposit enough light energy into the medium and produces permanent damage. The main mechanism of the carrier generation with relatively low intensity laser beams is avalanche ionization. This process involves: (1) the acceleration of conduction electrons by the laser field; (2) the generation of a second electron accompanied by a loss of kinetic energy of the first electron (3) the repetition of the process until the electron concentration is sufficient to damage the crystal structure.

At fixed wavelength and uniform illumination of laser pulses, Eq. (3.9) becomes

$$\frac{\partial}{\partial t}N(t) = \gamma(I)I(t)N(t) + \sigma_n I(t)^n \tag{3.10}$$

where the avalanche coefficient, β [1/ps], $\beta = \gamma I(t)$, and γ has units of [cm^2/(psTW)], and σ_n multiphoton absorption cross-section [cm^{-3}ps^{-1}(cm^{2}Tw^{-1})^n]. The analytic solution to Eq. (3.10) is given by

$$N(t) = \exp\left(\gamma \int^{t} I(t')dt'\right) \cdot \left\{ \int_{-\infty}^{t} \sigma_n I(t')^n (t') \exp\left(-\gamma \int^{t'} I(t'')dt''\right) dt' + N_o \right\} \tag{3.11}$$

where N_o is free carrier densities of $10^8/\mathrm{cm}^3$ at room temperature [62]. If the temporal profile of pulses is assumed to be

$$I(t) = I_o \mathrm{sech}\left(\frac{2t}{\tau_p}\right)^2 \tag{3.12}$$

where I_o is the peak intensity and τ_p is the pulse width. Inserting Eq. (3.12) into Eq. (3.11) yields

$$N(t) = \exp\left(\frac{\gamma I_o \tau_p}{2} \cdot \tanh\left(\frac{2t}{\tau_p}\right)\right)\left\{ \int_{-\infty}^{t} \sigma_n I(t')^n \exp\left\{-\frac{\gamma I_o \tau_p}{2} \cdot \tanh\left(\frac{2t}{\tau_p}\right)\right\} dt' + N_o \right\} \tag{3.13}$$

This analytic solution can predict the time-dependent electron density from both avalanche ionization and multiphoton absorption. For fused silica and BK7, the electron density is calculated based on the laser parameters and material parameters. Thornber has derived an expression for avalanche rate β as a function of electric field [63][64].

$$\beta(E) = \frac{v_d e E}{\Delta} P(E) \tag{3.14}$$

where the saturation drift velocity is v_d (~ 2×10^7 cm/s), the effective ionization energy is Δ, and e is the electron charge, and

$$P(E) = \exp\left(-\frac{E_i}{E(1 + E/E_{ph}) + E_{kT}}\right) \tag{3.15}$$

where E_i, E_{ph}, and E_{kT} ($E_i kT/\Delta$) are the threshold electric fields for carriers to overcome the decelerating effects of ionization scattering, optical phonon scattering, and quasielastic thermal-scattering in one mean free path, respectively. The Δ is 75 eV for BK7 and 18 eV for fused silica, fitted from [65]. The avalanche coefficient is calculated using E_i = 30 MV/cm, E_{ph} =3.2 MV/cm, and E_{kT} = 0.01 MV/cm refer to [66], which is plotted in Fig. 3.2.

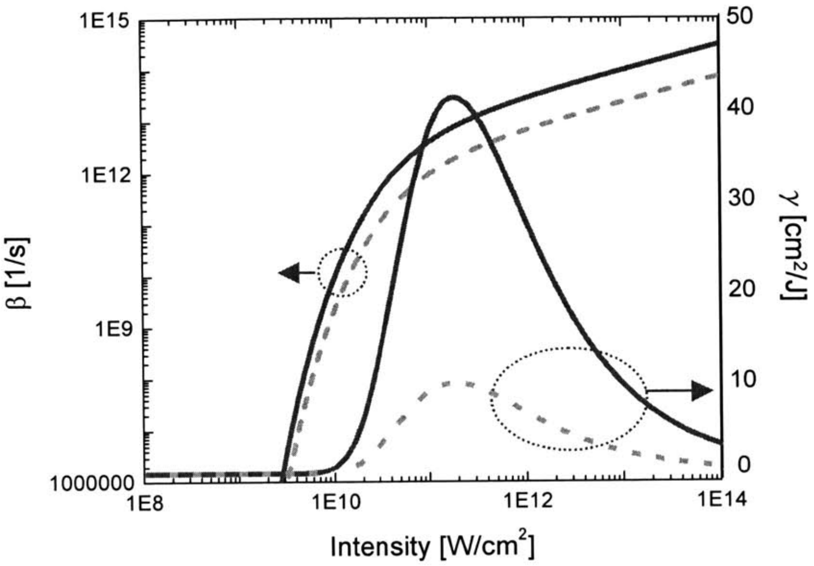

Figure 3.2: Avalanche coefficients of β and γ are determined from Eq. (3.14) and (3.15) for fused silica (solid) and BK7 (dot).

When the seed electrons are produced by multiphoton ionization, the electron density is increased by electron avalanche and reaches the maximal plasma density. Around the plasma frequency of ω_p in Eq. (3.16), two regimes of different optical properties are seen: large reflectivity and absorption coefficient for $\omega < \omega_p$, and small reflectivity and absorption coefficient for $\omega > \omega_p$. When the electron density increases dramatically, the material of a dielectric behaves like a conductor, which absorbs the laser energy via Joule heating similar to a metal. Now, the maximal or critical electron density is reached at the frequency of the incident light to the material, $\omega = \omega_p$, which is calculated in Table 3.1. At this plasma frequency, the light beams are no longer absorbed to the electrons but reflected instead.

$$\omega_p = \sqrt{\frac{Ne^2}{\varepsilon_o m_e}} \tag{3.16}$$

where N is the electron density, ε_o is dielectric permittivity, m_e is the electron mass. The highest possible electron density is set at $\omega = \omega_p$ by

$$N_{max} \approx \left(\frac{\omega}{e}\right)^2 \sqrt{\varepsilon_o m_e} \tag{3.17}$$

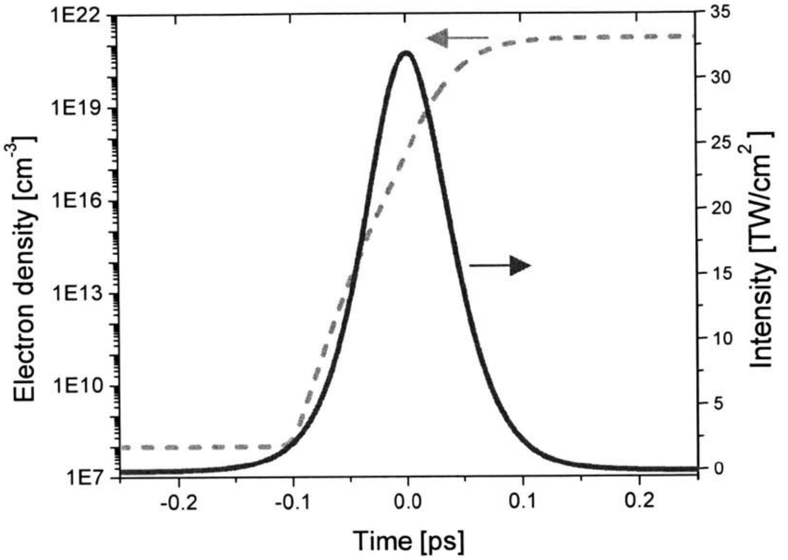

Figure 3.3: Electron density produced by avalanche ionization and multiphoton ionization (dot) is plotted with a sech-squared pulse (solid) that photoexcites fused silica.

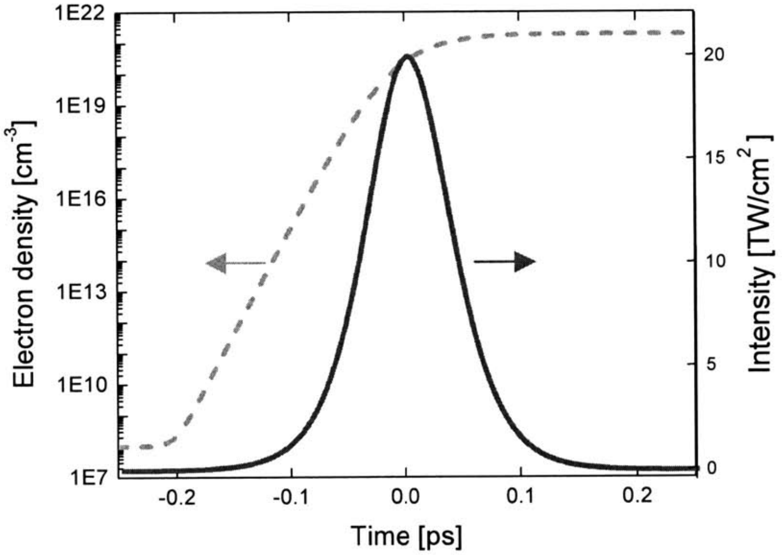

Figure 3.4: Electron density produced by avalanche ionization and multiphoton ionization (dot) is plotted with a sech-squared pulse (solid) that photoexcites BK7 or Corning 2947 glass.

If the intensity of incident laser beams is high enough, the high electron density causes explosive material damage or decomposition of the material, so called ablation. The decomposition density of electrons of N_{decomp} is defined to be a fraction of the total number of compositional valence electrons of materials for fused silica and BK7 as shown in Table 3.1.

$$N_{decomp} \approx f \cdot N_a \cdot n_{ve} \tag{3.18}$$

where there are the fraction of total number of bonds f, the atomic density of the material N_a, and the number of covalent bonding n_b. For fused silica and BK7, $N_a = 2.65\times10^{22}$, and $n_b = 4$. An assumption is made for the fraction f to be approximately 1% to decompose or ablate the material. Ablation is only possible when the electron density satisfies a criterion of

$$N_{decomp} \le N_{max} \tag{3.19}$$

Since this criterion is satisfied with the densities of $N_{decomp} = 1.06\times10^{21}$ and $N_{max} = 1.7\times10^{21}$ at 800 nm excitation and Eq. (3.19), these materials can be decomposed to make ablation. The electron density of Eq. (3.13) is plotted as a function of incident laser intensities in Fig. 3.3 for fused silica and in Fig. 3.4 for BK7. Consequently, the threshold ablation intensity of the laser light is determined to be $N(t) = N_{decomp}$, as shown in Table 3.1. This calculation well corresponds to the experimental result of damage threshold of 32 TW/cm^2 for fused silica and 28 TW/cm^2 for BK7 [67][68].

TABLE 3.1 For 800 nm (1.55 eV) photoexcitation, the effective ionization energy Δ, the number of photons to exceed the bandgap, n_{photon}, avalanche coefficient γ, multiphoton absorption cross-section σ_k [66], and threshold intensity for material ablation I_{th}.

Material	Δ (eV)	n_{photon}	γ [cm^2/J]	$\sigma_n$cm^{-3}ps^{-1}(cm^{2}Tw^{-1})^n	I_{th} [TW/cm^2]
Fused silica	18	6	5.4	$\sigma_6=6\times10^8$	32
BK7	75	3	1.62	$\sigma_3=7\times10^{17}$	20

3.2.3 Microexplosion in Transparent Dielectrics

When the intensity $I < I_{th}$, self-focusing of the laser beams due to the Kerr effect can occur in transparent dielectric materials. In this regime of the pulse intensity, focusing the fs-laser pulses into the transparent dielectrics leaves the front surface intact without occurring ablation, but produces modification or microexplosion in the inner medium. Self-focusing occurs if the laser intensity is high enough to produce a noticeable positive nonlinear contribution of n_2 to the refractive index n,

$$n = n_o + n_2 I \tag{3.20}$$

The peak power of the laser pulse exceeds the critical power for self-focusing P_{cr} is calculated by [69]

$$P_{cr} = \frac{3.77\lambda^2}{8\pi n_o n_2} \tag{3.21}$$

Beyond this power, catastrophic collapse of the laser beam to a singularity will take place. The critical power for BK7 and borosilicate glass (Corning 0211, bandgap of 4.4 eV), a glass with its property close to the soda lime glass (Corning 2947) used in the experiment, is 1.5 MW at 800 nm. In fused silica, the critical power is 4.3 MW at 800nm [67]. In the weak self-focusing and diffraction-limited focusing using a lens, the energy required to reach the break-down intensity is related to [70]

$$I_{sf} = \frac{I}{1 - P/P_{cr}} \tag{3.22}$$

In the experiment, the power varies from 0.5 MW through 1.25 MW with the intensity from 0.15 TW/cm^2 to 25 TW/cm^2, depending on focused spot sizes. According to Eq. (3.22) for BK7 at 800 nm, the self focusing power I_{sf} at the focal point can be larger than the damage threshold of I_{th} with the intensity of approximately ~ 7 TW/cm^2. Even if I_{sf} is smaller than I_{th}, strong nonlinear processes would generate significant electrons and achieve microexplosion-like material changes. Thus, self-focusing with sufficiently high intensity pulses can produce microexplosion similar to ablation on the surface of the material, which ends up with decomposition of materials or defect generation. After the nonthermal heating of electrons by the laser light is turned off, the microexposion rapidly cools down due to heat transfers to the neighboring lattice. Furthermore, this region inside the dielectric shrinks its volume, leaving the density of the material increased at the focal point. Hence, the density enhancement, i.e., densification, takes place to generate higher refractive index regions, as observed in the other groups [10][71]. This internal microexplosion mechanism using high intensity laser beams is used to fabricate versatile passive photonic circuits, as follows.

3.3 Experimental Setup

The laser used in the experiment is the novel high intensity Ti:Sapphire laser oscillator, as explained in Chap. 2. This KLM laser generates the pulse energies of up to 100 nJ with the pulse duration of 60 ~ 100 fs at 800 nm. For this nonlinear material processing [13][71], this laser is operated with net positive intracavity dispersion to provide flexibly high pulse energies. LaFN28 prisms replace fused silica prisms to make the laser more compact. To compensate the positive dispersion, SF10 prisms are used in the prism compressor, as shown in Fig. 3.5. The pulse durations and energies are varied by changing the separation of prisms in the prism compressor and the power of an Ar^+ pump laser, respectively.

Next, the laser output is focused inside standard microslide glass plates of Corning 2947 (soda lime glass) with its optical property very similar to BK7, by microscope objectives [13]. Numerous objectives of 0.2 numerical aperture (NA) to 0.9 NA (63 X Achroplan) are used, but since the laser beam is truncated through the small aperture of these objectives, the greatest NA varies from 0.6 to 0.9. To avoid retro-reflection that prevents the laser mode-locking, the Corning 2947 glass is tilted a few degrees from the normal incidence.

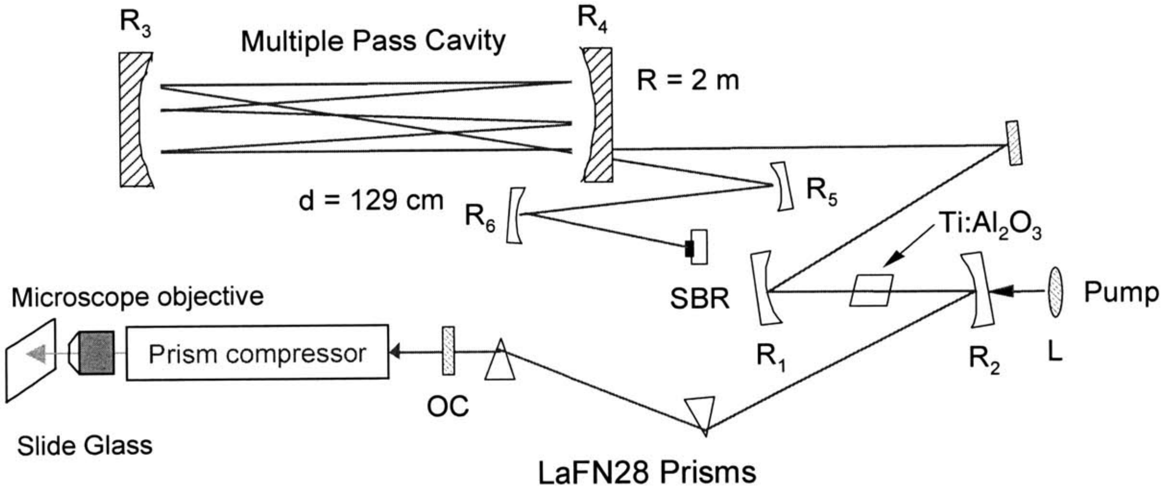

Figure 3.5: Schematics of waveguide fabrication with a Ti:Sapphire laser that incorporates a pair of multiple pass cavity mirrors; R_1, R_2, 10 cm radius of curvature (ROC) mirrors; R_3, R_4, 2" diameter MPC mirrors with 2 m ROC; R_5, 50 cm ROC; R_5, 20 cm ROC; L, 6.3 cm focal length pump beam focusing lens; OC, 27% transmission, 1/2" thick output coupler; external prism compressor that consists of a pair of SF10 prisms; Slide glass, Corning 2947.

3.4 Fabrication of Waveguides and Characterization

Waveguides are fabricated by laterally scanning the sample of glass plates with focal points of ~ 100 μm below the surface. It is used for a high-speed dc-motorized stage (Polytec PI,M-511.DD) capable of sub-μm resolution of spatial movement to precisely control the scanning speed.

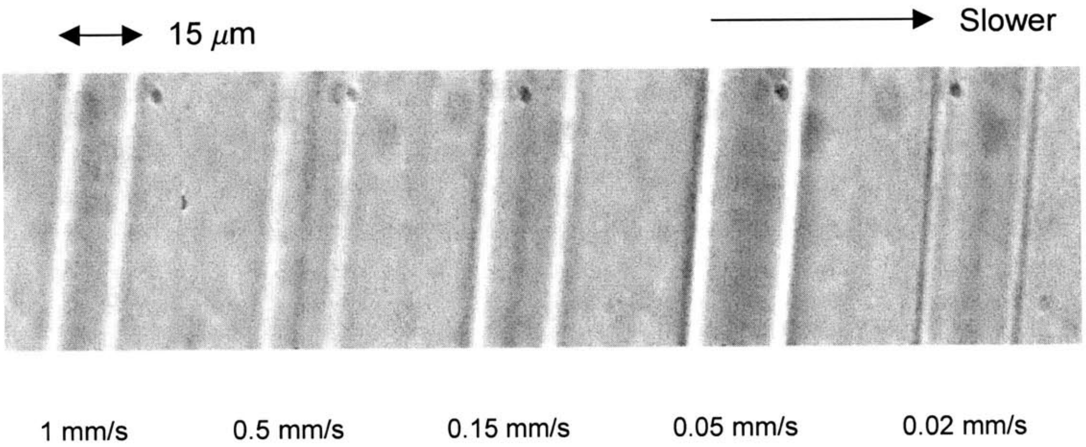

Figure 3.6: Microscope images of different sizes of waveguides, depending on the scanning speed of Ti:Sapphire laser beams.

Different sizes of linear waveguides are fabricated by changing the horizontal scanning speed of the laser, with the energies of 25 ~ 50 nJ and the pulsed durations of 80 fs, as shown in Fig. 3.6. As plotted in Fig. 3.7, the size of the waveguides is proportional to the $\log_{10}(v_s)$ or the $\log_{10}(I/l)$, where v_s is the scanning speed and I/l is the irradiated intensity per length. With the focused laser intensity of 1.45 TW/cm^2 through 3.5 TW/cm^2, the self focusing intensity in Eq (3.22) is 2.4 ~ 6 TW/cm^2, which is close to the threshold of microexplosion of BK7 as explained in Sec. 3.2.3. In this power range, processes such as significant expansion of the focal spot due to melting or defects, with partial internal explosion, would take place.

The guided mode structures are characterized, either by launching 544 nm He-Ne laser beams or 800 nm Ti:Sapphire laser beams into the different waveguides. These waveguides are fabricated by changing scanning speed from 0.5 mm/s to 10 mm/s, and fixed pulse energies of 25 nJ and fixed NA of 0.6. The waveguides of 4 μm core size is made with the scan-

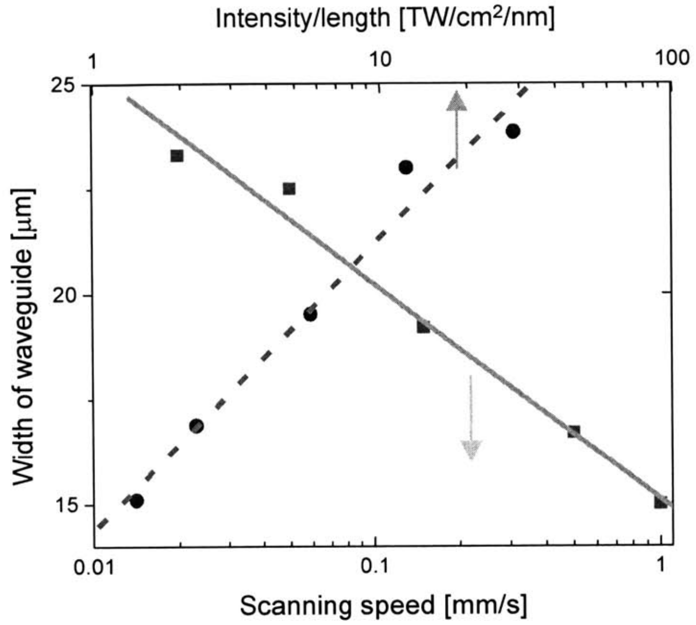

Figure 3.7: The scanning speed dependence of the size of waveguides fabricated: measurement (square-dot), fitting (solid); cumulative intensity dependence of the size of waveguides: measurement (circle-dot), fitting (dot).

ning speed of 10 mm/s, and the broadest waveguide of 20 μm is made with 0.5 mm/s. The near-field mode-profiles are monitored with a CCD camera, by coupling 544 nm He-Ne laser beams (Fig. 3.8) or by 800 nm CW Ti:Sapphire laser beams (Fig. 3.9). For waveguides shown in Fig. 3.8 (a) through (d), the mode profiles correspond to the linear polarized (LP) mode of LP_{51}, LP_{41}, LP_{21}, and LP_{11}. For waveguides in Fig. 3.9 (a) through (d), the mode profiles correspond to LP_{31}, LP_{21}, LP_{11}, and LP_{01} [72].

The change in refractive index with given pulse conditions is a very important parameter for designing devices of single or multi modes at a specific wavelength. Since two different wavelengths are launched to the same waveguides, the number of modes is analyzed by assuming step-index circular waveguides. The number of guided modes are determined by normalized frequency V with the NA and the core radius of the waveguide r by

$$NA = \sqrt{n_{core}^2 - n_{clad}^2} \tag{3.23}$$

$$V = \frac{2\pi r}{\lambda} \cdot NA \qquad (3.24)$$

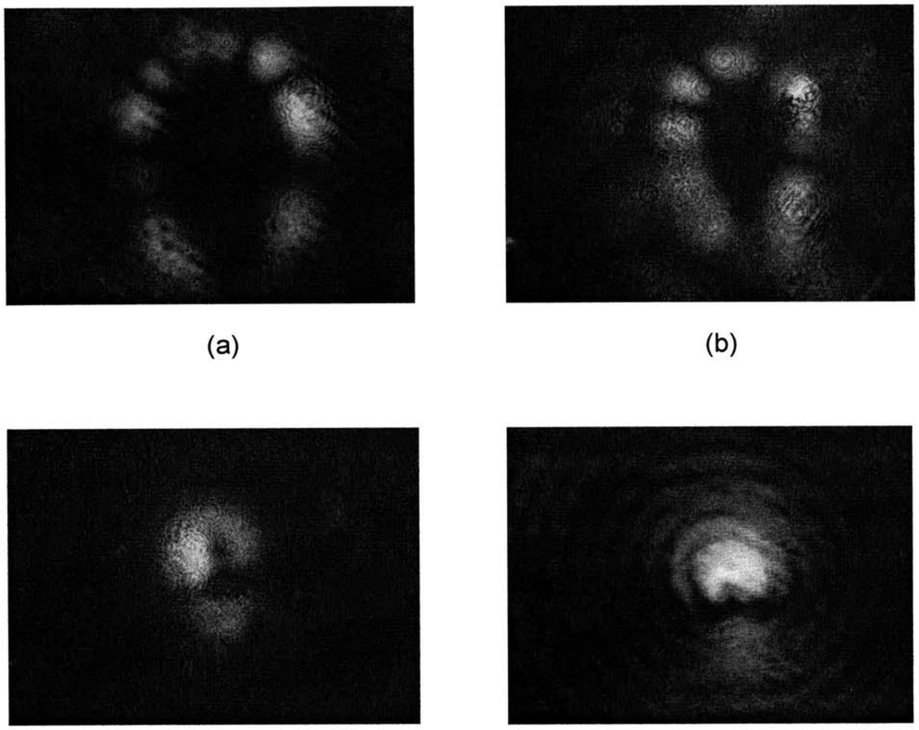

(a) (b)

(c) (d)

Figure 3.8: Mode profiles measured with 544 nm He-Ne lasers: with the different radii of the core (a) 10 μm; (b) 7.5 μm; (c) 4 μm; (d) 2 μm.

The lowest-order mode is LP_{11} in Fig. 3.8(d) and LP_{01} in Fig. 3.9(d), which have the same size of the core radius of 2 μm. From the cutoff V-number of LP_{11} and LP_{01}, given by the solution of Bessel function in in Eq. (3.24), the index of refraction is calculated. The lowest-order mode LP_{01} does not have a cutoff at the normalized frequency. The next-order mode is labeled LP_{11}, when $V = 2.405$. The higher order mode of LP_{21} is made when $V = 3.832$. Thus, to provide a single mode LP_{01} at 800 nm and the next mode LP_{11} at 544 nm, the V number should lies in between 2.405 and 3.832. Using Eq. (3.23) and (3.24), the core index of n_{core} is calculated to be 1.515 with the cladding index n_{clad} of 1.51. So the index difference between the core and glass substrate $(n_{core}-n_{clad})/n_{clad}$ is 4×10^{-3}, which is very consistent with the other groups' measurements of $3 \sim 4\times10^{-3}$ [71][73].

When the intensity of the laser is increased more than 30 nJ with 0.6 NA, plasma fluorescence is observed to the naked eyes. In this case the morphology of the waveguide structure is non-uniform along the waveguide such that bubbles or void-like structures are intermittently patterned.

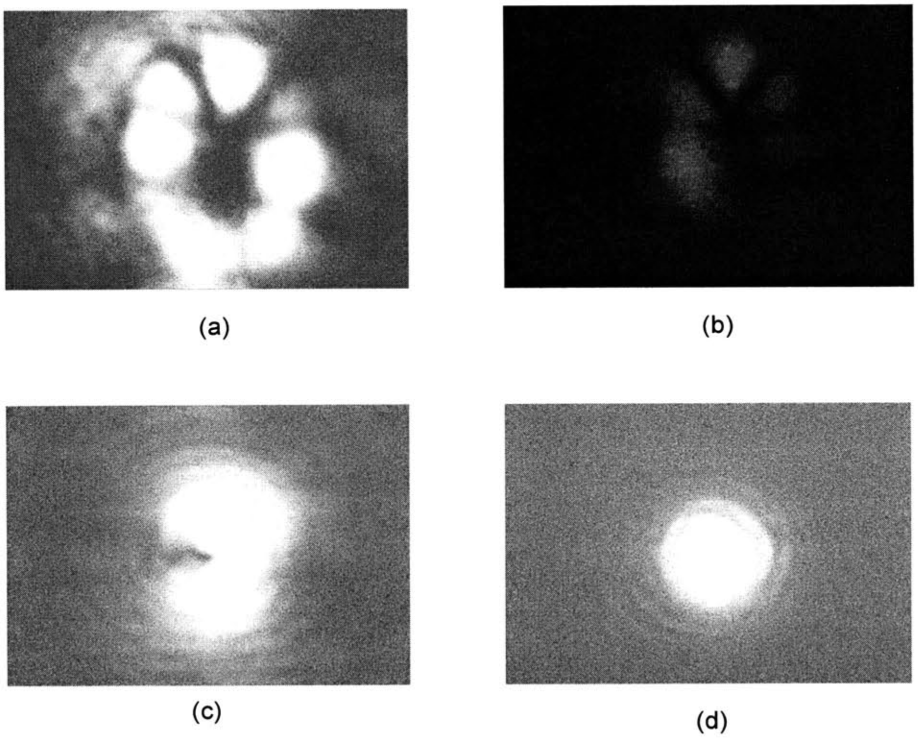

Figure 3.9: Mode profiles measured with cw 800 nm Ti:Sapphire lasers: with the different radii of the core (a) 10 μm; (b) 7.5 μm; (c) 4 μm; (d) 2 μm.

3.5 Fabrication of Gratings

To fabricate a frequency-filter similar to fiber Bragg gratings, grating structures are fabricated. A long period grating of 4 μm periodicity is fabricated. To this end, the incident high intensity laser beams are turned on and off using a chopper. Thus, corrugation is made through the waveguide, as shown in Fig. 3.10. Furthermore, the periodicity can be adjusted by changing the speed of scanning and the rotation frequency of the chopper. However, it is difficult task to fabricate waveguide gratings with a period of wavelength or so, because precise control of structural modification including index changes, scanning speeds, and laser

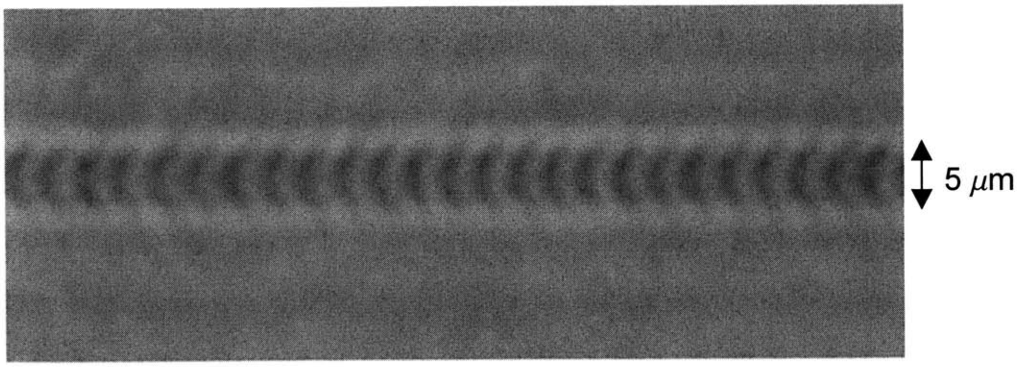

Figure 3.10: A grating is fabricated by chopping incident Ti:Sapphire laser beams.

intensities is necessary. Since a tunable light source at this infrared range is required to characterize frequency dependent transmission, frequency-domain analysis for this grating is not accomplished yet.

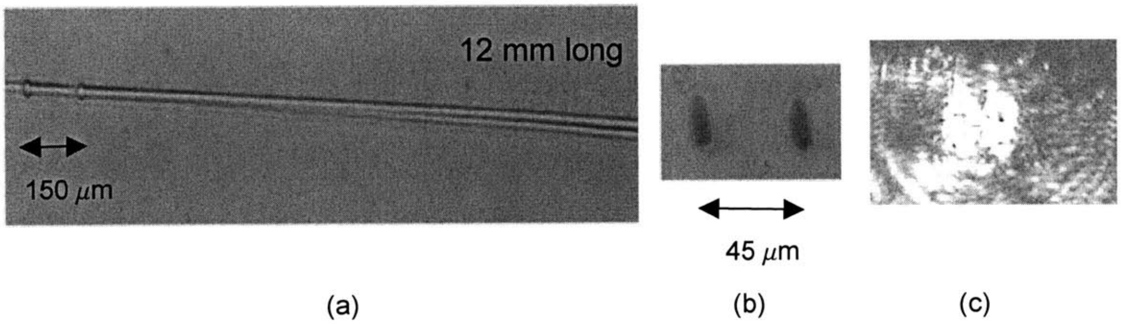

Figure 3.11: A Y-coupler (a) Top view; (b) Front view; (c) Output mode shape launched with 800 nm laser beams at the output port.

3.6 Fabrication of Coupled Mode Devices

3.6.1 Y-coupler

Once a single mode waveguide is developed, it is possible to fabricate a number of different devices. As a basic photonic device, a Y-coupler is fabricated by writing two identical waveguides at the Y-junction, as shown in Fig. 3.11. Each waveguide of the Y-coupler is fabricated by tightly focusing the high energy pulse using a 0.9 NA (net NA of 0.6) microscope objective inside a glass slide. The coupler is formed by translating the glass at a speed of 0.5 mm/s. Each waveguide is approximately 15 μm in diameter and 12 mm long, and the crossing angle is ~ 1°, as shown in Fig. 3.11(a). The 800 nm Ti:Sapphire laser beams are coupled at the two output ports with the beam coupled at the input port (Fig. 3.11(b)). As shown in Fig. 3.11(c), the beam coupling from one input port to two output ports is successfully demonstrated.

3.6.2 X-coupler

Each waveguide of the X-coupler is fabricated by the same method of fabricating a Y-coupler using a 0.9 NA microscope objective inside a glass slide, as shown in Fig. 3.12. The coupler is formed by cross-translating the glass sample perpendicular to the incident light at a speed of 0.4 mm/s. Each waveguide is approximately 15 μm in diameter and 12.5 mm long, and the crossing angle is 1.1 degrees. The coupled power of 544 nm He-Ne laser beam was measured at the two output ports with the beam coupled at either input port, as shown in Fig. 3.12(b). The launched beams are successfully coupled from one input port to two output ports. As shown in Fig. 3.12(a) and 3.12(c), the two waveguides of the X-coupler starts 120 μm under the surface and ends almost the surface because of vertical tilting of the sample. Fig. 3.12(b) and Fig. 3.12(d) show two beams coupled out when the He-Ne beams are launched from the output and the input port, respectively.

The cross-sectional profiles of the far field pattern are measured. The splitting ratio between two branches is approximately 1:1.1. This coupling ratio can be varied by changing the cross angle of two branches. It is interesting to note that there is a void region at the center of both waveguides, as observed in Fig. 3.13(c) [13]. Thus, the coupled light beam profile of Gaussian is seemingly divided into two radial regions in space. This region is due to multimode structure of the waveguide that has relatively low index changes at the center. When the laser light is focused into the central region with high intensity, the microexplosion overexpands and does not shrink much to densify the glass. Thus, the edge has higher index contrast than the central part of the waveguide.

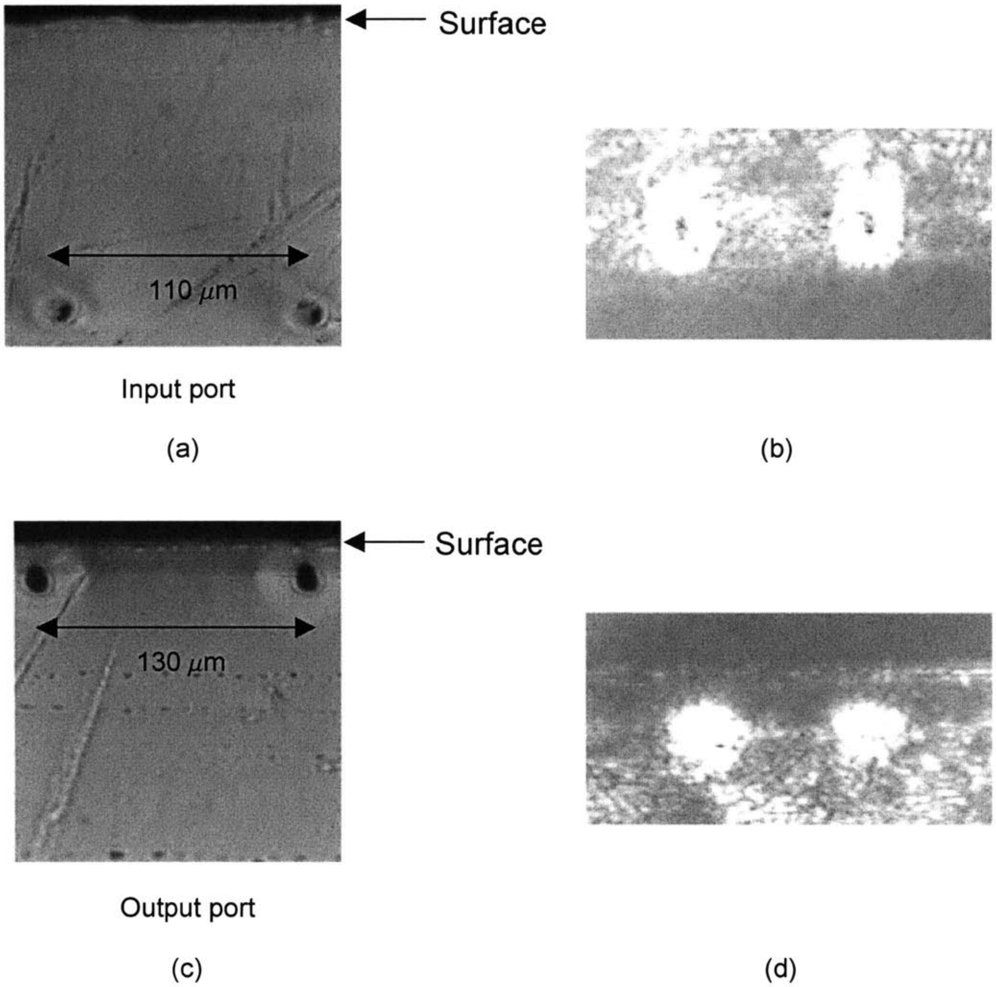

Figure 3.12: An X-coupler (a) Side view shown at the input por; (b) Output mode profiles launched with 544 nm laser beams at the input port; (c) Side view of at the output port. (d) Output mode profiles launched with 544 nm laser beams at the output port.

3.7 Fabrication of Three Dimensional Waveguides

Due to the high transparency of glass, most of the light transmits through the material to locally induce index changes at the focal spots. Both features of transparent glass and selective index changes in depth can provide a great advantage of 3D structures [74][75]. I demonstrate the fabrication of 3D devices of multiple waveguides that are vertically separated by 20 ~ 30 μm in depth, as shown in Fig. 3.14. An x-y scanning generates laterally multiple waveguides, and a z-scanning can generate vertically stacked waveguides or vertical couplers

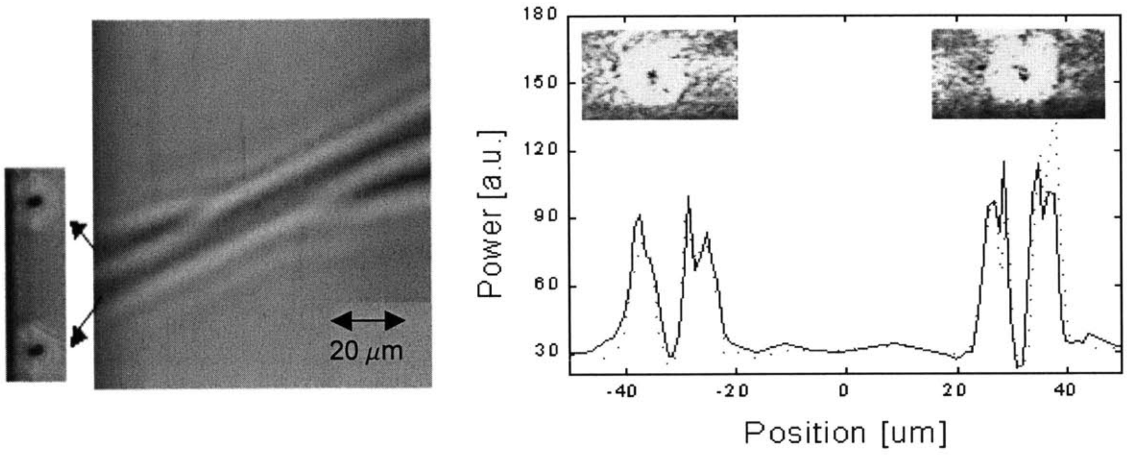

(a) (b) (c)

Figure 3.13: (a) Side view of an X-coupler shown at the input port. (b) Top view of the X-coupler. (c) The power at the output of an X coupler with a 544 nm He-Ne laser beam coupled into the input of one of the waveguides; input into one of the waveguide (dot), input into the other (solid). The inset shows images of the far-field modes.

at depths of as much as 300 μm below the surface of the glass. As shown in Fig. 3.14(b) and (c), four waveguides of 15 μm core size are vertically stacked within 80 μm in depth. It is intriguing that the launched light at the bottom-right waveguide might be slightly coupled to the left one, and then coupled to the top one, next to the left one. This multiple-layered structure can open up the possibility of 3D optical memories, possibly enhancing the writing capacity in compact disks.

The loss of these waveguides is not measured but could be conjectured from a similar waveguide. Florea et al., in University of Michigan have fabricated an active waveguide written by μJ pulse energies and a 2.5 cm focusing lens from Ti:Sapphire amplifiers on a commercially available Nd doped silica glass rod with Nd doping level of 2×10^{20} cm^{-3} [73]. They measured that the absorption, gain, and loss coeffcients, based on the cut-back experiment of this waveguide, are 4.6/cm at 806 nm, 1.5 dB/cm at 1054 nm, and 0.3/cm at 806 nm, respectively [76].

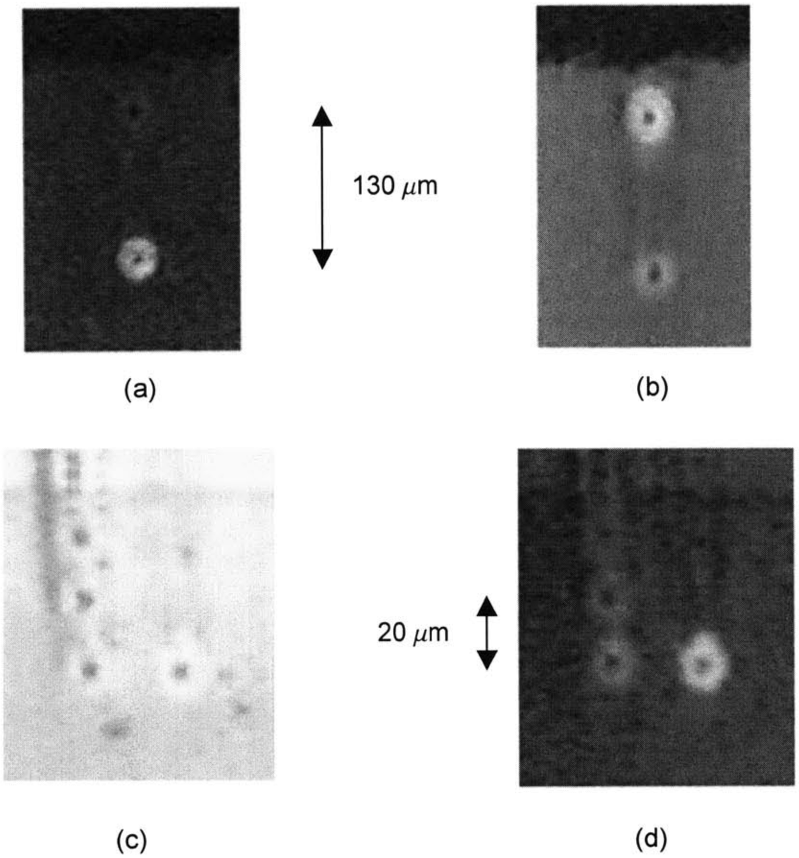

Figure 3.14: 544 nm He-Ne laser beams are coming out through vertically separate waveguides that are 130 um apart; (a) from the bottom waveguide; (b) from the top waveguide. Laser beams are coming out through vertically and laterally stacked waveguides that are 20 μm apart vertically with (c) a 800 nm Ti:Sapphire laser; (d) 544nm He-Ne laser.

3.8 Conclusion

I demonstrate single mode/multi-mode passive device fabrication directly by use of high pulse intensity laser beams directly from a novel, low repetition rate Ti:Sapphire laser resonator, without using any active devices or amplifiers. Two dimensional devices such as waveguides, gratings, and X and Y-couplers are fabricated, and most of their beam coupling is demonstrated. Three dimensional structures of multilayer waveguides are fabricated. Modal analysis shows that the index change after the laser-induced microexplosion is approximately 4×10^{-4}, which is consistent with the other groups' measurements. This nonlinear material processing on transparent glass is very promising technology for rapid prototyping and development of 3D photonic devices, possibly yielding significantly higher density integration than planar devices.

In future studies, I will investigate active optical devices of waveguide lasers and amplifiers using active glasses of, e.g., Er:glass and Nd:glass as well as active crystals of Ti:Sapphire, Cr:forsterite, etc. Eventually, it would be possible that 3D photonic circuits include all different passive and active components of laser transmitters, wavguides, and amplifiers where frequency filters of gratings or microring resonators are incorporated.

Chapter 4

Pulsed Laser Absorption Induced Quantum Well Intermixing

4.1 Introduction

Optoelectronic integration would be a boon to next generation lightwave circuits, because of their compactness, packaging robustness, reliability, reduced cost, and lower power consumption. However, it is a challenging task to combine active and passive PICs on one wafer. Lateral bandgap engineering is critical to realizing the potential benefits of PICs, because the different active and passive devices need different band gaps within the epiwafer. Conventionally, the process for fabricating PICs with different bandgaps consists of three steps: patterning, etching out the unwanted epitaxial layers, and subsequent selective epitaxial regrowth over the entire wafer, which is complex and cumbersome and requires a fair amount of cost and finesse.

Quantum well intermixing (QWI) is emerged as a simple, powerful, and promising technological approach for fabricating PICs [20][22]. QWI is a post-growth technique that allows the bandgap energy of an existing quantum well to be selectively modified. QWI slightly changes the composition of the interface between the quantum well and barrier layers through a process of controlled lattice disordering to form a new alloy. Essentially, QWI utilizes impurities or point defects such as vacancies or interstitials of lattice atoms that interdiffuse into the quantum well (QW) and barrier. Since QWs become metastable at high temperatures, due to large concentration gradient of atomic species across the QW/barrier, significant diffusion of atomic species hopping from the barrier to QWs and vice versa. The hopping of diffusion will occur the intermixing of the QW and adjacent barrier materials. This process provides a simple and robust route to fabricating PICs that integrate low-loss optical waveguides, modulators, lasers, and detectors, using only one epitaxial step. The key advantage of this technology is that different bandgap sections or different wavelength interfaces are aligned perfectly to each other. The reflection coefficient can be reduced to 10^{-5}, so the adiabatic transition in refractive index step can be achieved in a butt joint between active and passive regions.

4.2 Overview of Quantum Well Intermixing

QWI utilizes point defects such as vacancies or interstitials of interdiffusing lattice atoms [20][22]. Due to hopping of individual atoms in point defects from one lattice site to another, the QW intermixes or smears with adjacent barrier material. This allows the absorption edge of the QW structures to be controllably tuned with relatively high spatial selectivity. Essentially, three different QWI methods by which the defects are introduced have been developed, including impurity-induced disorder [20][77], impurity free vacancy disorder (IFVD) either by dielectric cap [78] or ion implantation [79], and laser or photoabsorption induced disorder (PAID) [80][81]. The impurity-induced method was discovered using Zn as an active dopant, about 20 years ago [77]. However, the more recent methods are preferable because the injection of active dopant ions into the waveguides can contribute to free carrier optical absorption. Direct laser writing without having the complication of using multiple Si_xN_y or SiO_2 layers for multiple bandgaps as used in IFVD, makes the PAID attractive for its simplicity.

Compared to the conventional regrowth and the selective area epitaxy, this fairly simple and planar processing allows cost effective and flexible PICs of passive and active components. To make QWI practical, it should fulfill following requirements:

(1) controllable bandgap changes between the various devices.

(2) very low loss compared to as-grown structures.

(3) no significant deterioration of electrical properties.

(4) no substantial adverse effect on the operating life time after the processing.

(5) almost no process-initiated changes in the properties of devices.

Furthermore, it is noted that the threshold current in semiconductor lasers is increased with the degree of interdiffusion (i.e., blue shift of wavelength). This is mainly due to the QW shape changing and the electrons and holes becoming less confined within the wells, leading to the emission properties closer to those of bulk material. In addition, waveguide loss in the passive sections that are fabricated from active sections by QWI is slightly increased mainly due to two reasons that follow. First, as the degree of blueshifts increases, the number of remnant point defects is increased and still reside in the structure as absorption centers. Second, impurities in the heavily-doped layer diffuse into the separate confinement heterostructure layer (SCH) in high temperature annealing during QWI, which increase free carrier absorption.

4.2.1 Advantages

The main advantage of the PAID technique is its selective interdiffusion of different QW layers [28][29][82]. The poor thermal stability of the InGaAs-InGaAsP system has been used to great advantage in the PAID process, in which photons from a 1064 nm Nd:YAG laser are preferentially absorbed within the InGaAs-InGaAsP QW region.

To achieve high spatial separation between intermixed and as-grown regions, pulsed laser beams are used, because continuous irradiation of laser beams heats a large lateral volume. Variations of the same technique using pulsed laser irradiation have recently been developed [30], and I coin them to be a pulsed-light absorption-induced disordering (PLAID) [31]. A Q-switched Nd:YAG laser with a pulse width of few nanoseconds is generally used. Since the spatial resolution is less than 3 μm, high density device manipulation with different bandgaps is enable. Unlike other QWI techniques, PLAID can simply achieve many different bandgap regions by only changing irradiated fluences for different regions, without using any photomasks.

It is especially interesting that frequency-doubled Nd:YAG lasers at 532 nm generate most defects in the capping layer rather than the defects that are generated in the SCH and MQW/ barrier regions at 1064 nm [31]. Thus, the remnant defects excited by PLAID using 532 nm pulses can be easily etched away to maintain the good crystal quality of QWs. The capping layer can be regrown to provide metal contacts later on.

4.2.2 Limitations

The CW PAID suffers from poor spatial selectivity due to thermal diffusion, and poor uniformity across the intermixed area accessed by the Gaussian beam profile. A pulsed laser can provide very good spatial resolution instead, but it is difficult to determine the optimal pulse durations and pulse energies. Compared to other QWI techniques, the PAID takes time to scan a whole wafer. Also, the power densities required to melt material can introduce thermal shock damage or sputtering if pulsed laser light is used. It can cause a potentially undesirable redistribution of dopants outside the active region of the device. Because melting needs a high temperature, dielectric capping is vital to preserve the stoichiometry of the semiconductor, but such caps can also act as sources of impurities or of vacancies. The quality of recrystallized material might be inferior to that of the original semiconductor.

4.2.3 Solutions

Although the CW PAID is not useful for high spatial selectivity due to its lateral heating, pulsed mode of the PLAID can impede the heat transfer of excited volume to unnecessary regions. Redistribution of dopants in the excitation or melting phase is prohibited in the PLAID process. Regarding well-defined fluence of pulses, a top-hat spatial profile is preferred over Gaussian beams. A surface needs a robust dielectric coating to protect crystalline structure against high intensity laser beams. As an approach to maintaining perfect crystallinity in the QWs during the PLAID, surface disordering is preferred over direct QW disordering, whose method is described in Sec. 4.2.1.

The PLAID is especially a powerful technique when the number of different bandgap regions increases even if there exist some limitations. Intermixing techniques such as IFVD need repeated, complicated steps of lithography patterns that are commensurate to the number of different bandgaps. In contrast, variable fluences of the laser beams in the PLAID can simply and reliably change as many bandgaps as necessary, while maintaining high spatial resolution of different bandgap regions.

4.3 Generic Mechanism of Quantum Well Intermixing

The intermixing mechanism between the QW and barrier is based on the fact that a QW has the large concentration gradient of atomic species across the QW/barrier interface. At high temperatures, significant diffusion of atomic species will occur, resulting in an intermixing of the QW and adjacent barrier materials, as shown in Fig. 4.1.

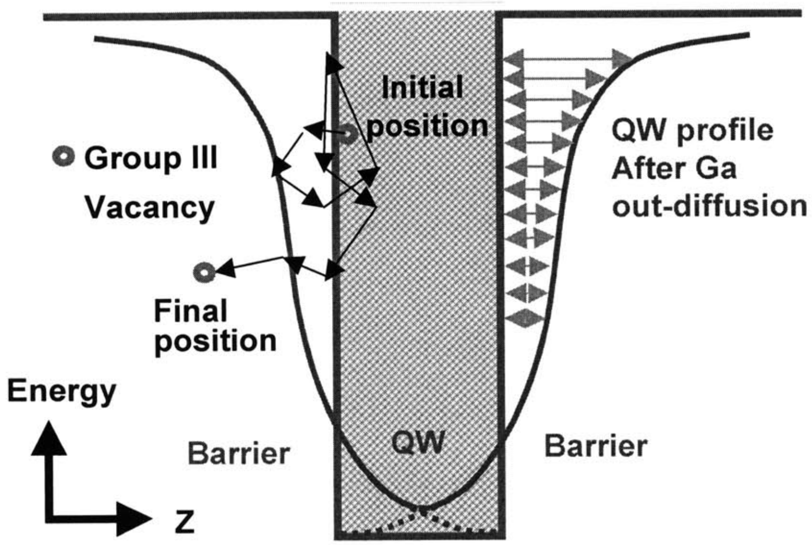

Figure 4.1: Schematic diagram of the lattice hops shows Ga out-diffusion from a QW and the QW interface crossings, carried out by group-III vacancies, during the random walks associated with their diffusion (adapted from [78]).

This process causes a rounding of the initially square QW bandgap profile and, in general, ensuing an increase of the bandgap energy. This in-turn modifies the subband energy in conduction and valence bands, resulting in the modification of interband transition energy. In addition, since the bandgap is increased, the refractive index is modified enough to provide optical confinement and gratings. This intermixing process can be greatly enhanced by the presence of impurities or defects in the vicinity of the interfaces of the QW.

After one of the disordering processes, the wafer is sent through an annealing process. At elevated temperatures, the vacancies or defects diffuse from their high-concentration region into low-concentration regions further down into the wafer structure. The vacancy movement intermixes the different atoms in the QW structure. The effect of intermixing creates a graded QW structure, thereby increasing its bandgap energy profile at the intermixed region [78]. Thus the final annealing process changes the QW bandgap energies in smooth steps. Smearing lattice boundaries provides precise alignment at active and passive regions without complicated regrowth steps. Since bandgaps can be tailored at any selected region of the quantum well, QWI can avoid any optical losses associated at the butt joints of an active region with a passive region. In effect, wafer-scale light beam connections at butt joints can be established.

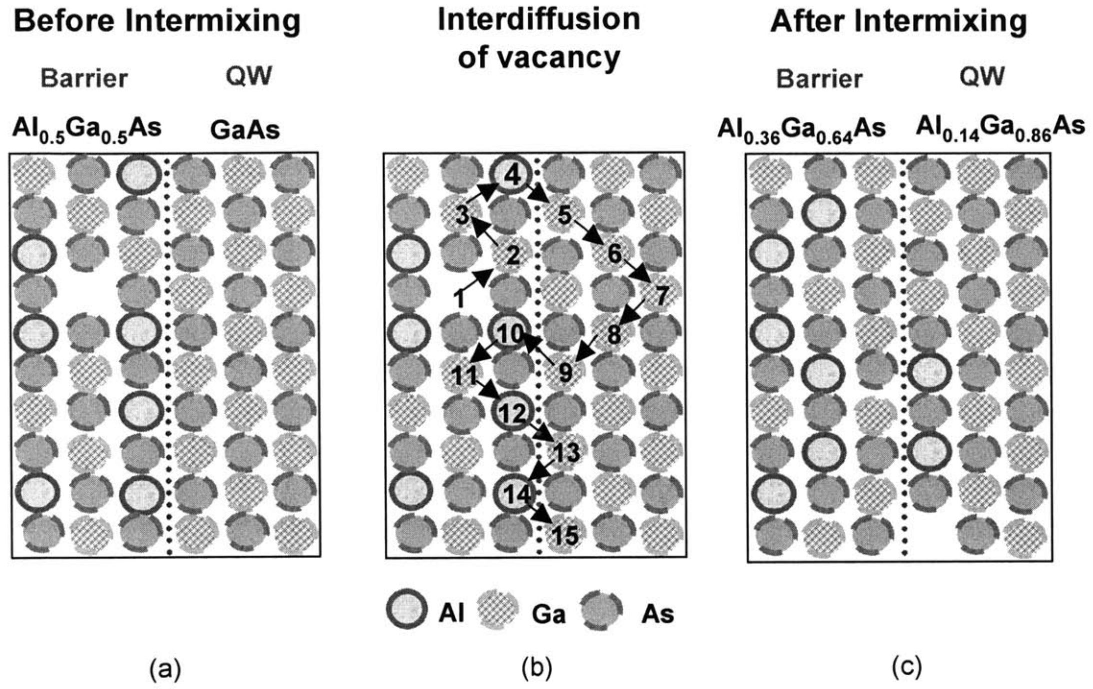
Before Intermixing
Barrier
QW
$Al_{0.5}Ga_{0.5}As$
GaAs
Interdiffusion of vacancy
1
2
3
4
5
6
7
8
9
10
11
12
13
14
15
After Intermixing
Barrier
QW
$Al_{0.36}Ga_{0.64}As$
$Al_{0.14}Ga_{0.86}As$
Al
Ga
As
(a)
(b)
(c)

Figure 4.2: These diagrams illustrate the change of atomic compositions (a) before QWI, (b) during QWI, and (c) after QWI by the diffusion of vacancies, which help interdiffusion of group-III atoms of Ga and Al.

Fig. 4.2 shows how vacancies affect group-III interdiffusion in a quantum well heterostructure. For example, compositional intermixing in, e.g. GaAs/AlGaAs, is carried out directly through diffusion of group-III vacancies of Ga (V_{Ga}) or Al (V_{Al}) as

$$V_{Ga} \Leftrightarrow V_{Ga} + (V_{Al} + I_{Al}) \Leftrightarrow (V_{Ga} + V_{Al}) + I_{Al} \Leftrightarrow V_{Al} \tag{4.1}$$

These vacancies hop around the QW and the barrier by exchaning atomic sites with interstitials of Ga (I_{Ga}) or Al (I_{Al}). After QWI in Fig. 4.2, the bandgap of as-grown QW is blueshifted from 1.424 eV of GaAs to 1.599 eV of $Al_{0.17}Ga_{0.83}As$ by 175 meV, following the compositional changes. The bandgap of $Al_xGa_{1-x}As$ is given by $1.424 + 1.247x$ ($0 < x < 0.45$) and $1.424 + 1.247x + 1.147(x - 0.45)^2$ ($0.45 < x < 1.0$).

Or Al and Ga interdiffusion is assisted by the formation of group-III Frenkel defect pairs, through diffusion of group-III interstitials as

$$I_{Ga} \Leftrightarrow I_{Ga} + (V_{Al} + I_{Al}) \Leftrightarrow (I_{Ga} + V_{Al}) + I_{Al} \Leftrightarrow I_{Al} \tag{4.2}$$

Thus, the interdiffusion of group-III atoms in the heterostructure is dependent on the diffusion coefficient as well as the concentration of group-III point defects [20][78]. Each defect is created with a certain activation energy that depends on the Fermi level, the As concentration, and the ambient temperature.

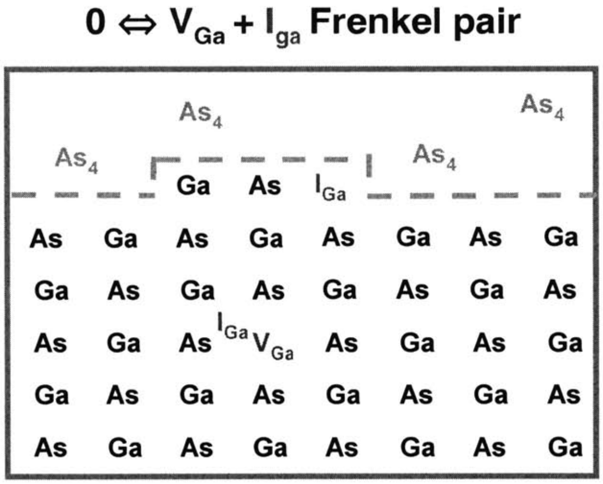

Figure 4.3: Schematic illustration of Frenkel defect pairs created in GaAs near the crystal surface. Interstitial defects can react with the As vapor at the crystal surface, thus determining equilibrium defect concentrations in GaAs bulk crystal.

Group-III point defects and Frenkel defect pairs can be introduced by various schemes such as impurities, dielectric caps or ion implantations, and photoabsorption. Regardless of the different disordering methods, during the annealing stage, these defects will diffuse through the heterostructures. Any diffusion length that has been undertaken by a defect is composed of a number of hops carried out in a random walk, as illustrated in Fig. 4.3. Within the regions in the lattice where group III vacancies exceeds group III interstitials, the movement of group III atoms is determined primarily by vacancies.

4.4 Pulsed Laser Absorption Induced Disordering

4.4.1 Method of Pulsed Laser Absorption Induced Disordering

The PLAID process [30][31][80] involves the irradiation of QW material, as shown in Fig. 4.3, by a Q-switched Nd:YAG laser with a pulse width of few nanoseconds. The absorption of high energy pulses from the Nd:YAG laser causes bond breaking and lattice disruption in the absorbed region of a sample, which lead to an increase in the point defect density. Subsequent high temperature annealing results in the diffusion of the point defects and enhances the QWI rate.

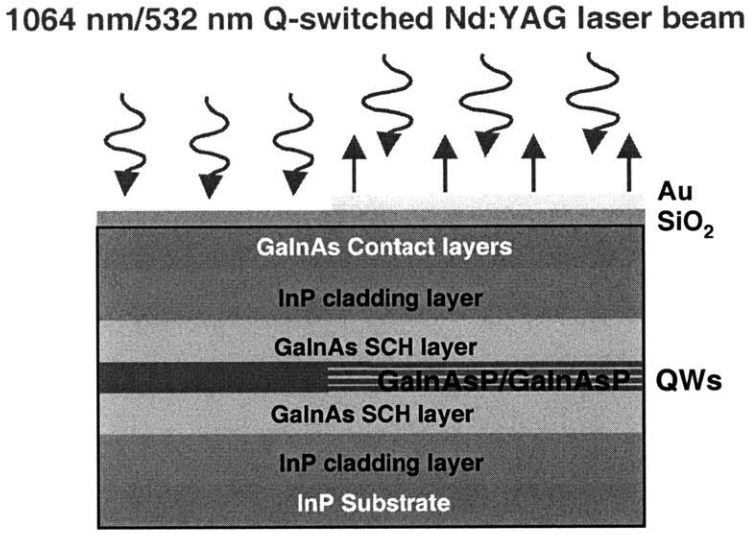
1064 nm/532 nm Q-switched Nd:YAG laser beam
Au
SiO2
GaInAs Contact layers
InP cladding layer
GaInAs SCH layer
GaInAsP/GaInAsP
QWs
GaInAs SCH layer
InP cladding layer
InP Substrate

Figure 4.4: Layer structure of the sample: most of the point defects are mostly created in the absorptive quantum well layers (1064 nm) or the contact layer (532 nm), where pulsed light beams transmit through SiO_2 antireflection coating or reflect from the Au coating (adapted from [28]).

A SiO_2 layer was first deposited on the entire InGaAs/InGaAsP wafer using PECVD or e-beam deposition to act as: (1) an antireflection coating; (2) a protective layer against surface reaction with the atmosphere, and (3) a capping layer to avoid the desorption of P or As form the sample, as illustrated in Fig. 4.4. It is noted that the thick SiO_2 can also protect the surface of the sample during high temperature annealing. To avoid poor recovery in the PL intensities and broadening of the PL spectra, laser irradiation with lower energy density and shorter exposure time is preferable. The sample was then annealed using rapid thermal annealing (RTA) apparatus. During annealing, the sample was sandwiched between two pieces of fresh GaAs substrates to provide As overpressure, so that the diffusion of As from the surface would be minimized during annealing. The SiO_2 layer was then removed by HF etching.

4.4.2 Review of Previous Work

The first CW laser induced disordering was investigated by Epler et al., at Xerox Palo Alto Research Center, on $GaAs/Al_{0.8}Ga_{0.2}As$ superlattices and incorporation of Si impurity using Ar^+ lasers working at 488 nm with 10^7 W/cm^2 back in 1986 [83]. They observed the transition between disordered and as-grown crystal due to melting and recrystallization using scanning electron microscopy. The first pulsed laser induced disordering was developed by Ralston et al, at Amoco Research Center, Illinois, using pulsed-KrF excimer lasers at 248 nm and 22 ns pulse durations with 220 - 900 mJ/cm^2 and frequency doubled Nd:YAG lasers of a few ns-pulses in 1987 [84]. They observed the intermixing of $Al_xGa_{1-x}As/GaAs$ superlattices by measuring GaAs-like longitudinal and transverse phonon peaks using Raman scattering profile and Auger electron spectroscopy extensively.

The device level experiments were pioneered by McLean, et al, at the University of Glasgow, UK, with InGaAs/InP based MQW structures in 1992, using cw PAID [78]. They used CW Nd:YAG laser working at 1064 nm with $0.1 \sim 2$ kW/cm^2 to intermix MQW regions and achieved bandgap shifts as large as 123 meV at 77 K. A year later, they fabricated a modulator based on quantum-confined Stark effect on GaInAs/GaInAsP MQW structures in 1993 and achieved 157 meV bandgap shifts [28]. They also achieved a good spatial selectivity of 25 μm, and 130 nm bandgap shifts of intermixing using pulsed-PLAID using Q-switched Nd:YAG laser at 1064 nm with 50 mJ/cm^2 [85]. By now, they have fabricated tunable multifrequency lasers, electroabsorption modulators, broadband LEDs, and monolithically integrated circuits with lasers, modulators and passive waveguides, on InGaAs/InGaAsP MQW structures, mostly using CW PAID [81][82][86][87]. Since 1997, Dubowski et al, at National Research Council of Canada have worked on PAID technology to fabricate monolithic mutiple wavelength ridge waveguide laser arrays using Nd:YAG lasers [29][88]. They have also worked on a comparative study of laser and ion implantation-induced QWI in GaInAsP/InP microstructures [88].

From 2000, Ong, et al, at Nanyang Technological University, Singapore, in collaboration with the UK group, have focused on PLAID processes to achieve high spatial resolution of ~ 2.5 μm [30][89]. They have worked on InGaAs/InGaAsP MQW/barrier structures with ns-Nd:YAG lasers at 1064 nm with 240 mJ/cm^2 minimal fluence and achieved bandgap shifts as large as 112 meV at 1550 nm with 3.9 mJ/cm^2 fluence.

4.5 Experiment of Pulse Laser Absorption Induced Disordering

4.5.1 Experimental Setup

Here, most PLAID experiments of mine are performed using the second harmonic beams of 532 nm rather than the fundamental beams of 1064 nm from a Nd:YAG laser. Since the bandgap of the capping layer of InGaAs is 1650 nm as shown in Fig. 4.5, most of the 532 nm beams is absorbed in the capping layer but the fundamental at 1064 nm beams are much transmitted to reach the QW region. Hence, 532 nm beams generate most defects in the capping layer and 1064 nm beams in the SCH and MQW/barrier regions. Although these defects diffuse into the MQW/barrier region to make QWI at high temperature, the remnant defects still reside in the source region, which degrades crystal structure quality and increase absorption/ loss in a device. For this reason, 532 nm pulsed beams are preferred in the experiment, to generate defects on the capping layer that is etched away after the PLAID process. The goal for the experiments is to achieve well-defined and high quality QWs with reasonable bandgap shifts after intermixing, while the least number of remnant defects are left after the PLAID process.

The p-i-n laser structure used in this study was grown by metal organic chemical vapor deposition in the University of California at Santa Barbara, whose structure is shown in Fig. 4.5. There are six 1% compressively-strained quantum wells and seven barriers made of InGaAsP quarternary surrounded by the InGaAsP quaternary undoped SCH cladding region. The delta-layer in p-SCH region is designed for another type of experiments to test current leakage over SCH p-cladding interface [90]. For 532 nm pulsed light at room temperature, the energy deposited in different layers of the epi-structure in Fig.4.5 is plotted by taking account of absorption coefficients for different bandgaps, as shown in Fig. 4.6. In this plot, the surface reflection is not counted. Following are the absorption coefficients [1/cm] of each layer: 3.94×10^5 ($In_{0.53}Ga_{0.47}As$, 50 nm); 30 (1×10^{18} Zn:InP, 50 nm); 10 (7×10^{17} Zn:InP, 2000

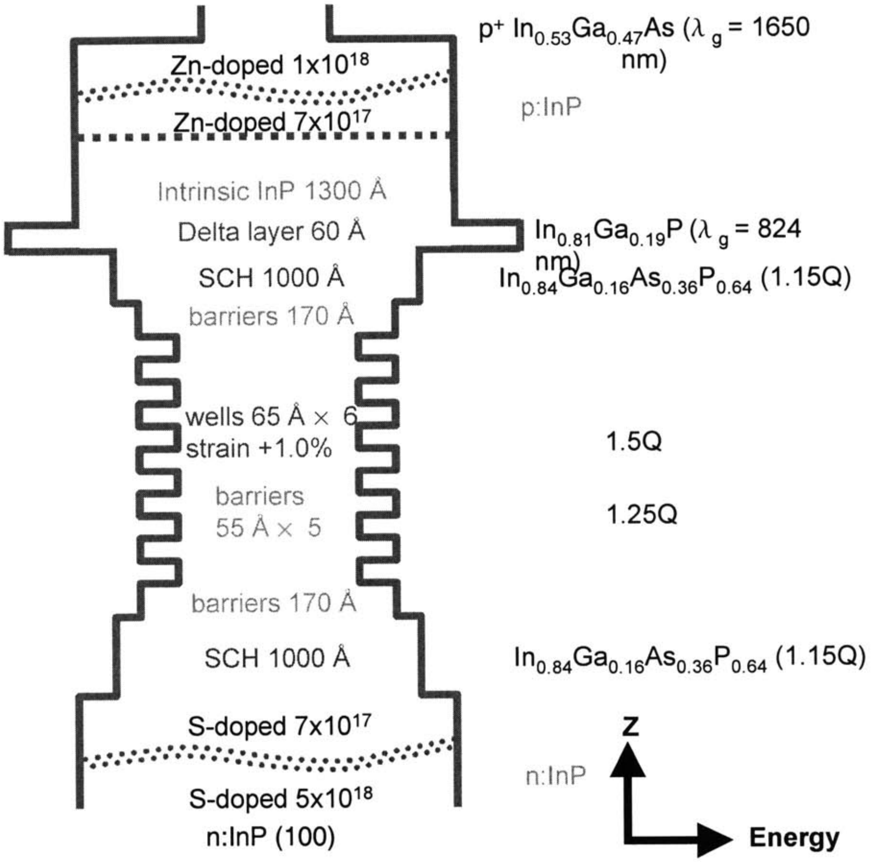
Zn-doped 1x10¹⁸
Zn-doped 7x10¹⁷
Intrinsic InP 1300 Å
Delta layer 60 Å
SCH 1000 Å
barriers 170 Å
wells 65 Å × 6
strain +1.0%
barriers
55 Å × 5
barriers 170 Å
SCH 1000 Å
S-doped 7x10¹⁷
S-doped 5x10¹⁸
n:InP (100)
p⁺ In0.53Ga0.47As (λg = 1650 nm)
p:InP
In0.81Ga0.19P (λg = 824 nm)
In0.84Ga0.16As0.36P0.64 (1.15Q)
1.5Q
1.25Q
In0.84Ga0.16As0.36P0.64 (1.15Q)
n:InP
Z
Energy

Figure 4.5: Structure of epitaxial layers for the PLAID process.

nm); 0 (intrinsic InP, 130 nm); 8×10^4 (delta layer, 6 nm); 1.5×10^5 (SCH, 100 nm); 1.5×10^5 (QW/barrier, 158 nm)[1][91].

For the PLAID process, samples are irradiated with the fundamental frequency of 1.064 μm or the second harmonic frequency of 532 nm of a Q-switched Nd:YAG laser (Infinity 40-100 Coherent Laser Inc.), at room temperature. The samples sit on a copper plate to facilitate cooling, at a few degrees off to normal incidence to the surface, so as to avoid back-reflection damage of the Nd:YAG laser. The typical pulse duration of Gaussian pulses of this laser is 3.5 ns for 1.064 μm and 3 ns for 532 nm, and the repetition rates is varied from 10 Hz to 20 Hz for these frequencies. For a faster processing, 10 Hz is used for 1.064 μm and 20 Hz for 532 nm. The photon energy density or fluence is chosen from zero to 400 mJ/cm^2. The samples are

---

1. The free carrier absoprtion coefficient is assumed from that in GaAs.

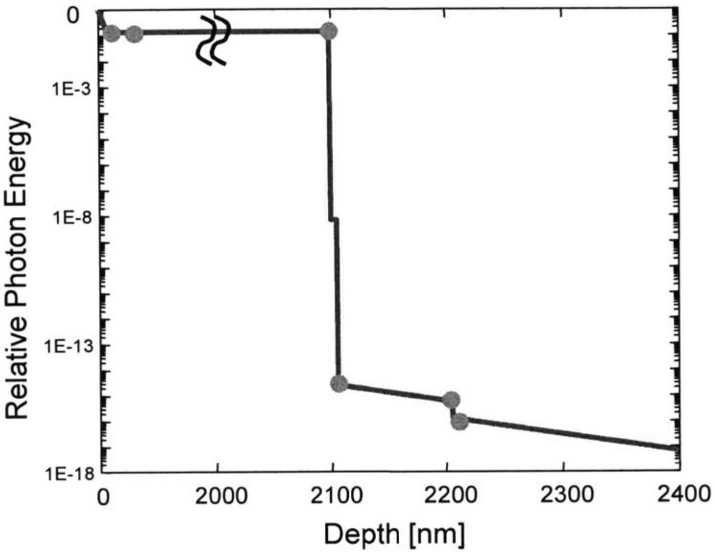

Figure 4.6: Photon energy is absorbed and deposited on different layers from the top of the capping layer to the MQW regions. The dots indicate the interfaces of different layers.

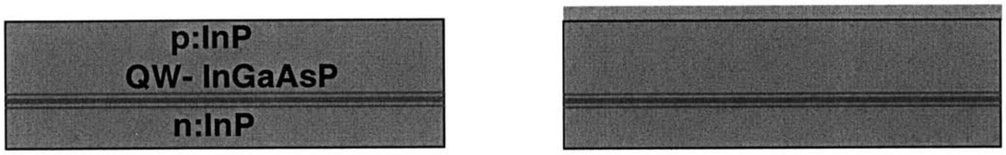

1. p-InP/InGaAsP/n-InP Epi-wafer

2. Ebeam Deposition of SiO_2

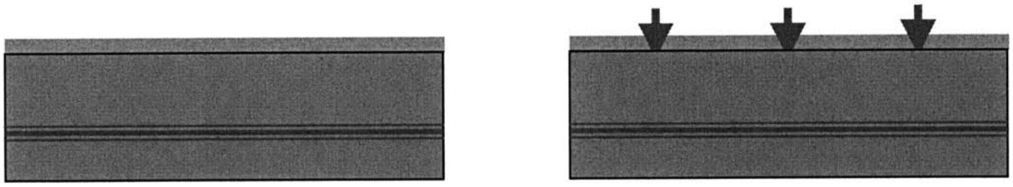

3. Irradiate pulsed Nd:YAG beams

4. Irradiate pulsed Nd:YAG beams

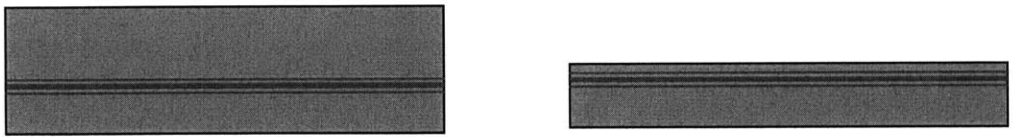

5. RTA at 675 °C for 3 min, sandwiching GaAs

6. Etching mesa with $H_3PO_4 : H_2O_2 : 8\ H_2O$ and $HCl:H_3PO_4$

Figure 4.7: Processing steps for oxide coating, PLAID, and etching

moved horizontally along the long axis of oval shaped laser beams at 0.1 Hz over a few mm during the laser irradiation, to avoid local damage due to hot-spots in the laser beams. Before the laser exposure, 6400 Å thick SiO_2 was coated on the samples with Electron Beam Deposition, so as to provide optimal anti-reflection coating for both 1.064 μm and 532 nm. The processing steps are detailed from the dielectric coating to etching mesa of the damaged capping layer after the PLAID process in Fig. 4.7. The top InGaAs capping layer is etched with 1:8:1 Phosphoric acid, Hydrogen Peroxide, and DI water for 1 min and the InP capping layer is etched with 1:1 Hydrochloric acid and Phosphoric acid for 2 min. The selective wet etching is stopped on top of the InGaP delta layer.

The samples are then annealed in RTA at 625 °C to 725 °C for 1 min to 5 min with a control sample that is not irradiated. During RTA, the samples are sandwiched between two fresh GaAs wafers, to provide As over-pressure.

4.5.2 Photoluminescence Measurement

The photoluminescence (PL) measurement for the irradiated samples is carried out at room temperature to observe the bandgap shifts of QWs. The PL measurement is carried out with a photo-excitation source of a CW Ti:Sapphire laser working at 975 nm, as shown in Fig. 4.8. With this wavelength, the light transmits through the InP capping layer and reach QWs. The continuous light beams from a Ti:Sapphire laser with 40 mW output power are delivered to the samples via 50/50 multimode fiber coupler. The photoluminescence is collected by an aspheric lens and delivered to an optical spectrum analyzer (HP7004A-HP70951B, 600-1700 nm). The output power is measured by an optical multimeter (ILX Lightwave) with a power detector head (OMM-6810B, InGaAs, 400-1100nm) in the other branch of the coupler.

4.5.3 Analysis of Photoluminescence Measurement

The samples are irradiated at 1.064 μm with the 10 Hz Nd:YAG laser from 1 min to 10 min, and then annealed in RTA at 650 °C for 2 min (Fig. 4.9). As the laser irradiation increases, the intensity of PL diminishes, but the bandgap shifts increases. However, the bandgap shifts start to be saturated beyond 3 min irradiation. FWHMs of the samples are almost the same as a control-sample, and the maximal bandgap blue-shift is 33 nm at room temperature.

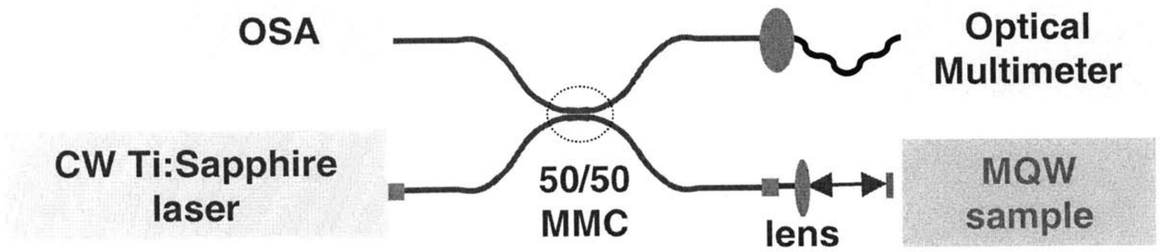

Figure 4.8: Schematic diagram for PL measurement: OSA, optical spectrum analyzer; MMC, multimode fiber coupler; Lens, 0.16NA 5 mm diameter, f = 15.36 mm.

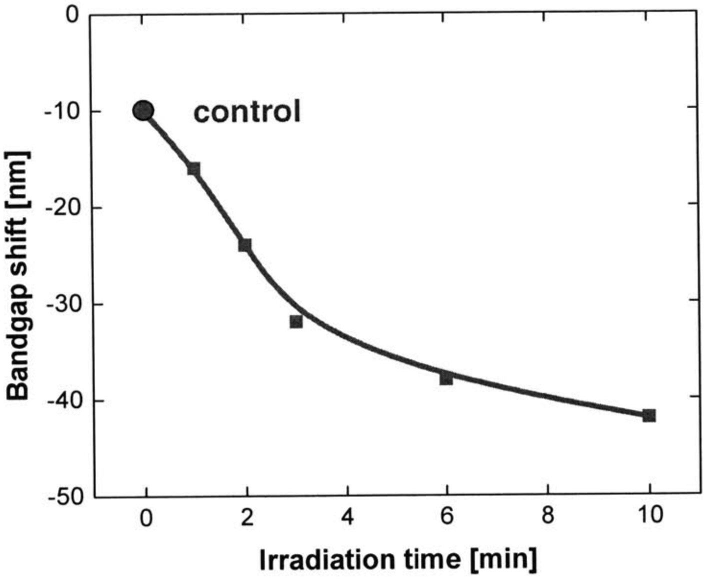

Figure 4.9: The irradiated fluence is 300 mJ/cm^2. Photoluminescence spectra measured at room temperature, after 650 °C rapid thermal annealing for 2 min show a maximal peak shift of 33 nm, compared to the bandgap shift of the control (circle).

Fig. 4.10 shows PLs of the InGaAsP/InGaAsP MQW samples after the 3 minutes irradiation of 20 Hz Nd:YAG 532 nm laser beams with the fluence of 65 mJ/cm^2 and 125 mJ/cm^2, respectively. These samples are annealed at 675 °C for 3 min, whose PL peak remains as narrow as the control-sample. The significant bandgap shift is observed with the fluence of 125 mJ/cm^2.

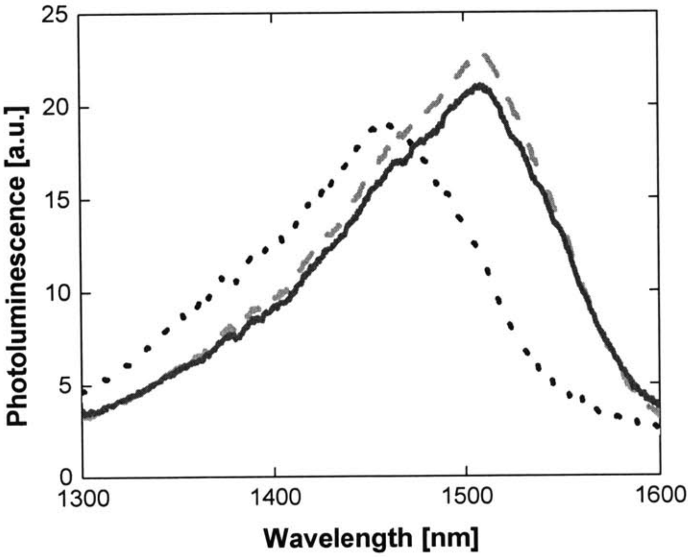

Figure 4.10: The blue-shift of photoluminescence is measured; the PLs of the InGaAsP/InGaAsP MQW sample after the RTA and laser irradiation with no irradiation (solid), the fluence of 65 mJ/cm^2(dash), and 125 mJ/cm^2(dot), respectively.

The intensity of the PL peak is measured for different fluences of 65 mJ/cm^2 and 125 mJ/cm^2. As opposed to the diminishing of peak values due to smearing of the bandgap in QWs, the peak value increases as QWI is enhanced, as shown in Fig. 4.11. This phenomenon is explained by the surface removal of the InGaAs capping layer, which enhances the transmission of Ti:Sapphire excitation photons to the QWs. However, the reduction of the peak value is observed after 1 min irradiation, as shown in dot lines of Fig. 4.11. The PL peak of the control-sample slightly diminishes to ~ 75% compared to that of as-grown when annealing temperature increases because of bandgap reshaping.

Fig. 4.12 shows the net bandgap blueshifts as large as 40 nm after 3 minutes irradiation of 535 nm, 20 Hz Nd:YAG laser beams with the fluence of 125 mJ/cm^2, as the irradiation duration increases. However, the net bandgap shifts of the sample irradiated with the fluence of 65 mJ/cm^2 is a few nm compared with the control-sample. Apparently, the blueshifts of the bandgaps appear to be saturated as the laser irradiation duration increases.

Fig. 4.13 shows the effect of RTA durations after the 3 min irradiation of 535 nm, 20 Hz Nd:YAG laser beams with the fluence of 125 mJ/cm^2. When RTA duration increases, the bandgap of the control-samples is shifted as large as 25 nm compared with the as-grown sam-

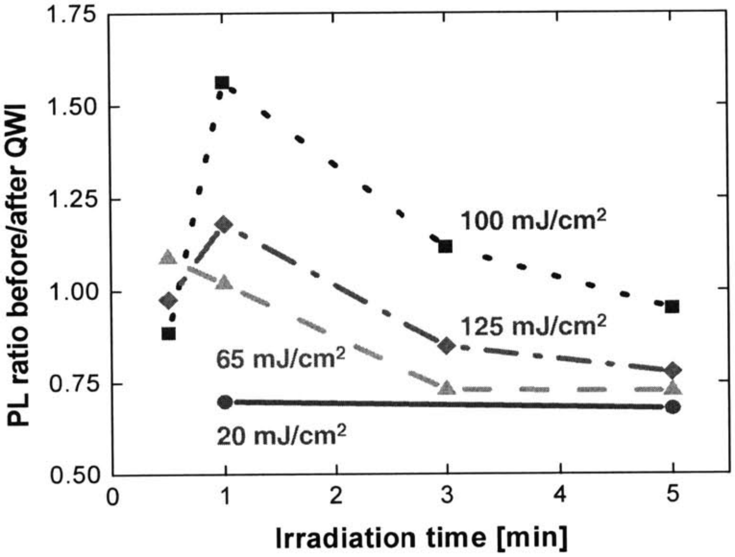

Figure 4.11: The intensity changes of PLs are measured as the irradiation of 532 nm Nd:YAG laser beams on MQW samples increases with different fluences and fixed RTA at 675 °C for 3 min; 20 mJ/cm^2 (solid), 65 mJ/cm^2 (dash), 100 mJ/cm^2 (dot), and 125 mJ/cm^2 (dash-dot).

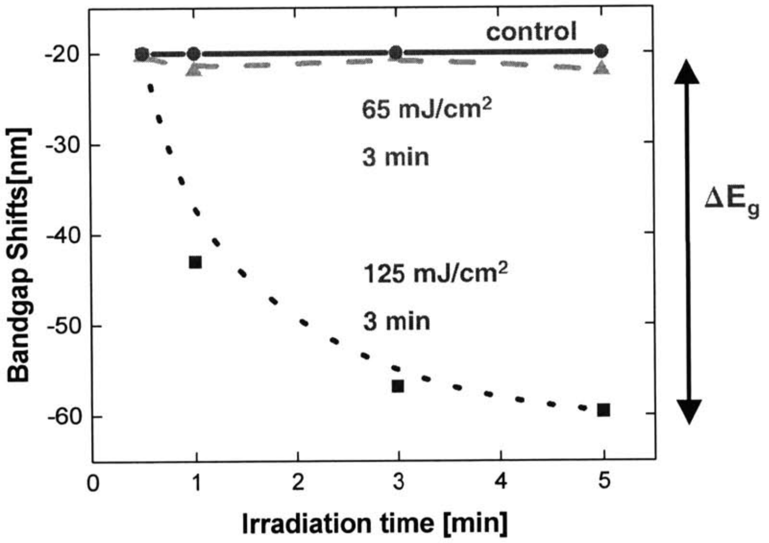

Figure 4.12: The bandgap shifts are represented by measuring the wavelength shifts of the peak value of each PL; the effect of laser irradiation at 532 nm with no irradiation (control), the fluence of 65 mJ/cm^2 and 125 mJ/cm^2.

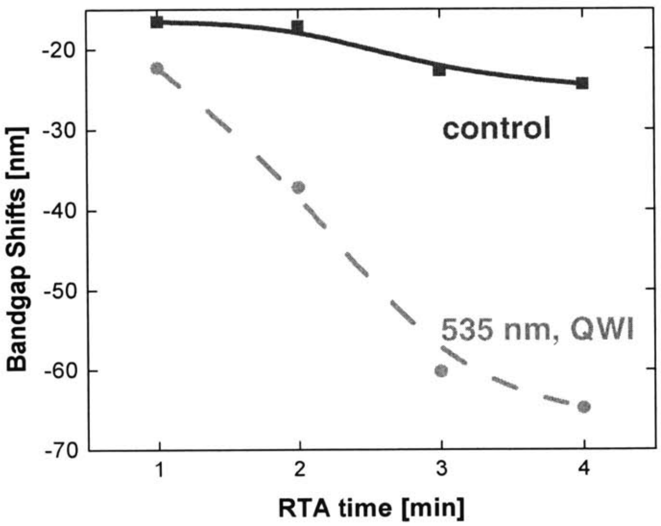

Figure 4.13: The blue-shift of PLs is measured to observe the effect of RTA time with an InGaAsP/InGaAsP MQW sample after the 3 minutes irradiation of 535 nm, 20 Hz Nd:YAG laser beams with the fluence of 125 mJ/cm^2. These samples are annealed at 675 °C; the control sample after the RTA only and the MQW sample after PLAID and RTA.

ple, and that of the sample irradiated with the fluence of 125 mJ/cm^2 is blue-shifted up to 40 nm, compared with the control-samples.

The effect of excitation wavelengths is studied with two different samples that are irradiated with 1.064 μm and 532 nm, respectively, as shown in Fig. 4.14. Under the same irradiation fluence of 125 mJ/cm^2, the maximal 45 nm bandgap shift annealed at 725 °C RTA for 3 min is observed with the sample of 532 nm excitation, compared with the control-sample. However, no bandgap shift is observed with the sample of 1.064 μm excitation. This effect of wavelength dependence of excitation is explained by the threshold difference of excitation wavelengths. The fluence of absorbed 1.064 μm light at the top InGaAs layer is not high enough to produce the point defects that can induce QWI. In contrast, the fluence of absorbed 532 nm light can generate enough point defects by melting of the top InGaAs layer with this fluence. The theoretical modeling of this comparison will be extensively discussed in the Sec. 4.6.3.

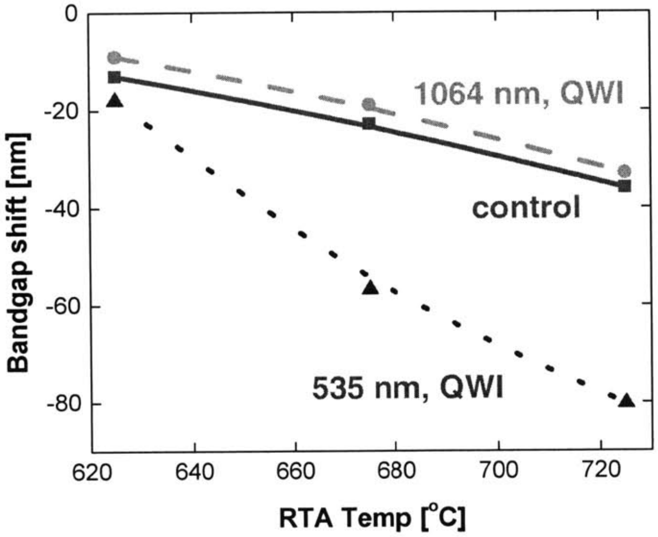

Figure 4.14: The blueshift of PLs is measured to observe the effect of RTA with an InGaAsP/InGaAsP MQW sample after the 3 min irradiation of 20 Hz Nd:YAG laser beams with the fluence of 125 mJ/cm^2, annealed at 675 °C for 3 min; a control sample after the RTA only (solid); 532 nm excitation (dot); 1064 nm excitation (dash).

4.5.4 Surface morphology

Surface morphology is scrutinized with micropic surface images. Fig 4.15(a) and 4.15(b) show that the surface images are intact before/after the oxide coating except dust particles on the surface. As shown in Fig. 4.15(c), the capping layer is mostly damaged after the PLAID with the fluence of 65 mJ/cm^2. This damaged region acts as the source of point defects. After wet-etching of this region, the surface morphology is fully recovered to be the same as the bare surface of the as-grown sample (Fig 4.15(d)). However, the surface irradiated with the fluence of 125 mJ/cm^2 (Fig. 4.16(a)), after the wet-etching, is left with ripples, as shown in Fig. 4.16(b). The surface imperfections after the etching comes from the heat transfer at melting from the InGaAs capping layer to the delta/SCH layer.

4.5.5 Experimental Conclusions

The bandgap shifts measured with the peak value of each PL compared to that of as-grown samples determine the threshold laser fluence for QWI. Regardless of irradiation wavelengths, bandgap shifts are saturated as the irradiation duration increases. From Fig. 4.9, the threshold fluence for bandgap shifts, at 1064 nm with 3.5 ns pulse duration, is observed less

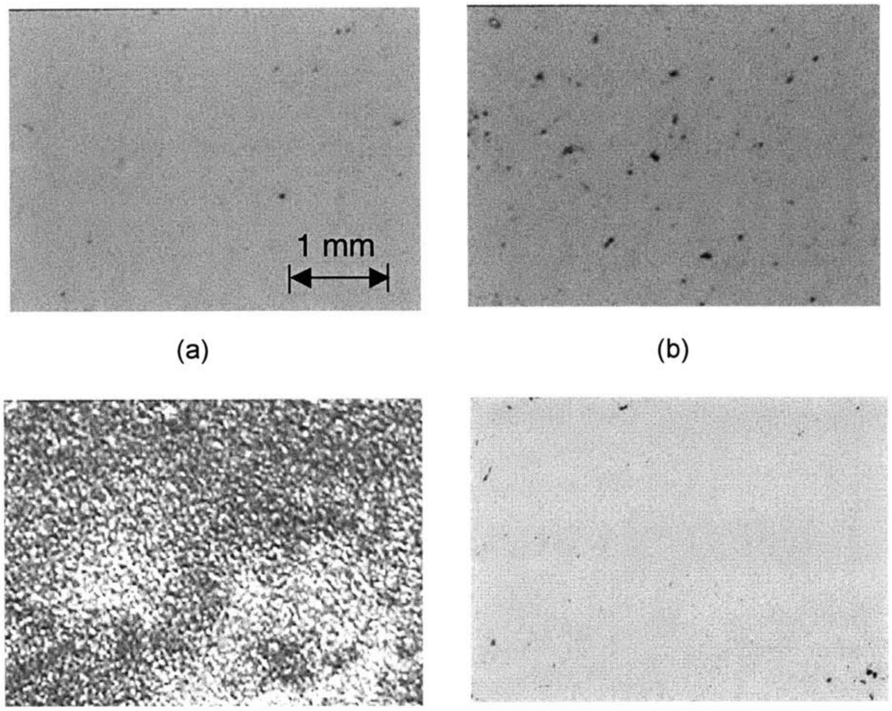

(a) (b)

(c) (d)

Figure 4.15: Microscope images of the surface (a) bare surface, (b) after 640 nm SiO_2 coating (c) After PLAID with 65 mJ/cm^2, (d) After wet etching of InGaAs/InP capping layers

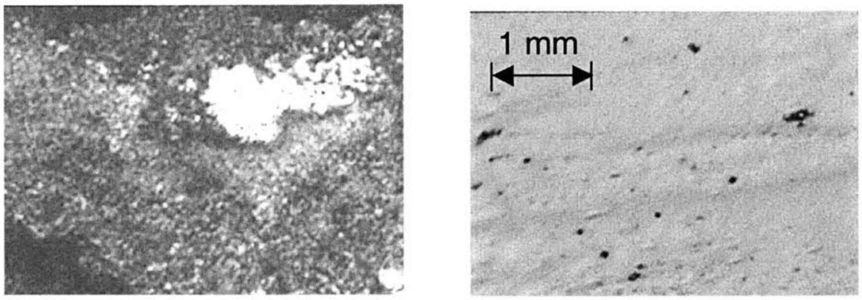

(a) (b)

Figure 4.16: Microscope images of the surface: (a) After PLAID with 125 mJ/cm^2, (d) After wet etching of InGaAs/InP capping layers.

than 300 mJ/cm^2. From Fig. 4.12, the threshold fluence for bandgap shifts, at 532 nm with 3 ns pulse duration, is very close to 65 mJ/cm^2 by observing the tendency of bandgap shifts.

The maximal bandgap blue-shift at 1064 nm irradiation of 6000 pulses compared to as-grown samples is 33 nm after 625 °C for 2 min RTA with the fluence of 300 mJ/cm^2, measured at 298 K, respectively. The maximal bandgap blue-shift at 532 nm irradiation of 6000 pulses is 45 nm after 725 °C for 3 min RTA with the fluence of 125 mJ/cm^2. The surface is damaged by removal of InGaAs capping layer above 65 mJ/cm^2. After the wet-etching of InGaAs/InP capping layers irradiated with 65 mJ/cm^2, the surface morphology is recovered as good as as-grown samples. However, ripples are observed at the surface irradiated above 125 mJ/cm^2, after the wet-etching. To take advantage of the separate source of defects away from QWs at 535 nm excitation, high quality and robust oxide coating is mandated, and the InP capping layer needs to be thicker than 2 μm to keep heat transfer for reaching the QWs. Then the disordered region both by laser irradiation and defect generation can be etched away to regrow the perfect crystalline capping layer later on.

4.6 Theory for Pulsed Laser Absorption Induced Disordering

4.6.1 Overview of Theoretical Modeling

Instead of using e-h excitation model in Sec. 3.2, in this section, a comprehensive theoretical model is developed to unravel laser absorption induced disordering and point defect generation for which experiments are presented in Sec. 4.5. This model focuses on estimating the threshold fluence of pulsed laser beams to achieve bandgap shifts. So, the goal for modeling is to understand the disordering mechanism macroscopically, based on a material decomposition mechanism such as melting or vaporization. Other experimental results are qualitatively explained from the viewpoint of lattice disordering and diffusion of defect centers for QWI in high annealing temperature, subsequent to photo-chemical bond breaking and defect generation mechanisms. The whole QWI process with intense pulsed laser beams is summarized below.

(1) ns-pulsed Nd:YAG laser irradiation at 532 nm is absorbed on the capping layer of InGaAs.

(2) Intense photons excite high density electron hole pairs from the valence band (bonding states) to conduction band (antibonding states) by linear absorption and avalanche ionization.

(3) Excitation of a large fraction of electrons to antibonding states causes repulsive interatomic forces that destabilize the lattice.

(4) The thermalization of lattice heating leads to a complete solid-liquid melting transition, vaporization, or direct bond-breaking.

(5) During the melting or vaporization, the covalently bonded lattice is heated, weakened, and disordered.

(6) The disordered lattice promotes the generation of Frenkel defect pairs.

(7) At the high annealing temperature, these point defects diffuse from the capping layer to the QW/barrier region.

(8) Point defects hop around the lattice and cause the atoms of the QW to intermix with those of the barrier, as explained in Section 4.3.

(9) The QW is modified and its bandgap is blue-shifted.

Laser processing requires a detailed knowledge of the fundamental interactions between laser light and matter and of the various relaxation processes involved. The elementary excitation is divided into thermal and non-thermal as explained in Sec. 3.2, where thermal excitation takes place if the thermalization of the excited carriers is fast compared to both the excitation time and subsequent scattering processes. In a thermally activated system, the state of the system is described by the temperature and the total enthalpy if phase changes or chemical reactions are involved. In contrast, non-thermal activation is a primary interaction between light and matter in which the state is described by the electron temperature only because electron-phonon coupling can be neglected in a ultrashort time scale of less than 100 fs - 1 ps.

In contrast to nonthermal decomposition or ablation of materials via femto-second laser pulses, excitation with nanosecond pulses on semiconductors or narrow bandgap materials with $h\nu > E_g$ causes ablation such as melting, sublimation, and vaporization when the pulse duration is longer than the phonon relaxation time.

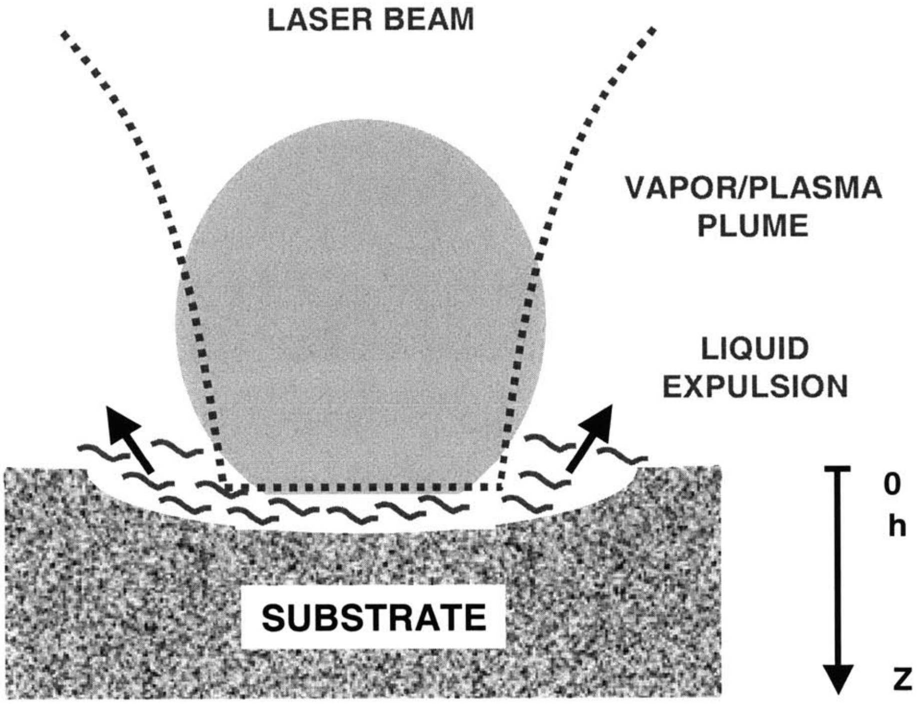

Figure 4.17: Laser induced surface melting, ablation, and liquid phase expulsion; h is ablation depth.

4.6.2 Theoretical Modeling of Laser Induced Decomposition

If the pulsed-laser fluence exceeds the threshold fluence for surface melting, liquid-phase expulsion, and evaporation, removal of surface elements starts with the formation of a plume, as illustrated in Fig. 4.17. The lattice temperature profile $T(\vec{r}, t)$ can be calculated from the heat conduction equation as

$$\rho(T)C_p(T)\frac{\partial}{\partial t}T(\vec{r}, t) - \nabla\kappa(T)\nabla T(\vec{r}, t) = Q(\vec{r}, t) \tag{4.3}$$

where ρ(T) [g/cm^3] is the density of mass, C_p(T) [J/gK] the specific heat at constant pressure, κ(T) [W/cmK] heat conductivity, and Q [W/cm^3] heat source. Here, the thermal properties can be simply characterized by a heat diffusivity, $D = \kappa/\rho C_p$ [cm^2/s], if the substrate is isotropic and uniform. The laser beam intensity is assumed to be, $I(\vec{r}, t) = I_o exp[-t^2/\tau_p^2]$ with a flat-top spatial profile, where τ_p is the pulse duration. The solution to Eq. (4.3) can be simplified, in the case of $\omega \gg \Delta h > max[l_\alpha, l_D]$, where Δh is the thickness of the substrate, ω is the beam size, l_α is the absorption length of optical penetration to the substrate, and l_D the diffusion length of excited electrons. If the lateral dimension of the incident beam is much larger than both the depth of the substrate and the absorption length or diffusion length, the lateral temperature is uniform compared to the variation of the temperature in the z-direction. So, the lateral heat flow can be ignored. Now that the heat flow is characterized by one dimensional propagation of heat in the z-direction, this equation reduces a (1+1) dimensional boundary value problem.

If all coefficients are independent of temperature, and laser irradiation with square pulses in time is uniformly absorbed in a very thin surface layer, the temperature distribution at $t < \tau_p$ is given by

$$T(\vec{r}, t) \approx T_o + \frac{2(1-R)I_o}{\kappa}\sqrt{Dt} \cdot ierfc\left(\frac{z}{2\sqrt{Dt}}\right) \tag{4.4}$$

where T_o is ambient temperature [92]. The *ierfc* function is defined as,

$$ierfc(x) \equiv \int_x^{\infty} erfc[s]ds = \int_x^{\infty}\left(\frac{2}{\sqrt{\pi}}\int_s^{\infty} e^{-t^2}dt\right)ds = \frac{1}{\sqrt{\pi}}e^{-x^2} - x \cdot erfc(x) \tag{4.5}$$

The temperature at $t > \tau_p$ is given by [92]

$$T(\vec{r}, t) \approx T_o + \frac{2(1-R)I_o}{\kappa}\sqrt{Dt} \cdot \left(ierfc\left(\frac{z}{2\sqrt{Dt}}\right) - \sqrt{\frac{t-\tau_p}{t}} \cdot ierfc\left(\frac{z}{2\sqrt{D(t-\tau_p)}}\right)\right) \tag{4.6}$$

To obtain an approximate temperature profile based on Eq. (4.4) and (4.6), effective temperature coefficients are calculated by taking their average in time as

$$[\kappa, Cp, \rho, R]_{eff} = \frac{1}{T_m - T_o}\int_{T_o}^{T_m}[\kappa[T], Cp[T], \rho[T], R[T]]dT \tag{4.7}$$

where R is the reflectance of the substrate. In Fig. 4.18 and Fig. 4.19, since the latent heat of melting or vaporization is not considered, and approximated parameters are used, only is the tendency of temperature profile depending on the depth and time before/after excitation provided.

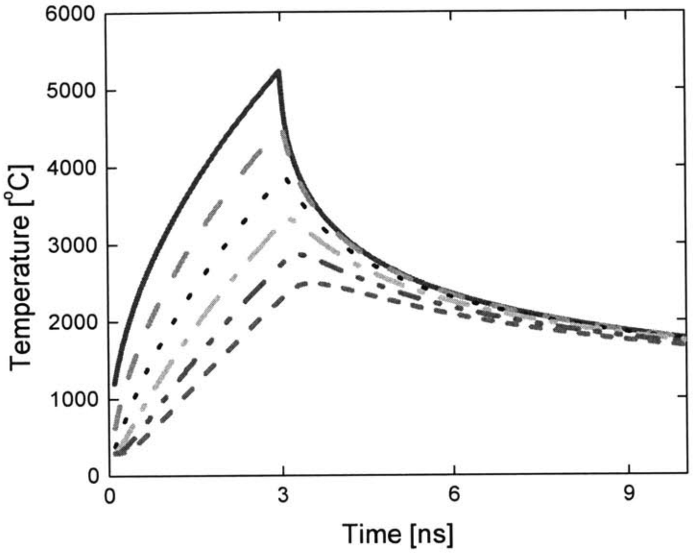

Figure 4.18: Variation of temperature with time for a uniform heating around the surface bounding a semi-infinite half-space, launched with 3 ns, 532 nm wavelength, and 81 mJ/cm^2 fluence: surface (solid), 10 nm deep (dash), 20 nm deep (dot), 30 nm deep (dash-dot), 40 nm deep (dash-dot-dot), and 50 nm deep (short dash).

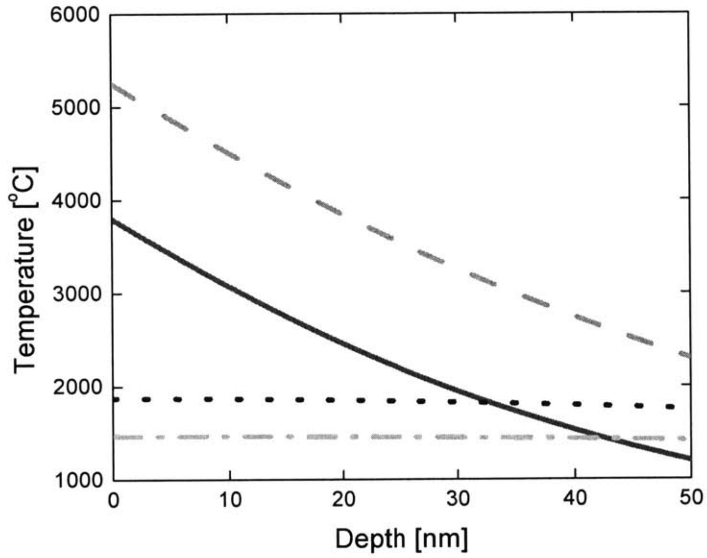

Figure 4.19: Variation of temperature with depth for a uniform heating over the surface bounding a semi-infinite half-space, launched with 3 ns, 81 mJ/cm^2: after 0 s (solid); τ_p (dash); $3\,\tau_p$ (dot); $5\,\tau_p$ (dash-dot).

The heat diffusion length is described by $l_D \approx 2\sqrt{D\tau_p}$. However, since all heat parameters in Eq (4.3) are strongly temperature dependent, and phase changes occur during the laser irradiation, a more complex formulation using numerical analysis is required. In order to solve this equation more intuitively, Eq (4.3) is integrated in time while neglecting the spatial variation of the temperature along the z-direction, as shown in Eq. (4.8).

$$\int_{T_o}^{T} \rho(T')C_p(T')dT' + \int_{T_o}^{T} (\delta(T'-T_m)\Delta H_m + \delta(T'-T_v)\Delta H_v)dT' = \frac{\int_0^{\tau_p} Q(t)dt}{T(t)} \tag{4.8}$$

For this calculation, enthalpy [J/cm^3] of melting and vaporization are used because the experiments, in general, performed at constant pressure while the pulsed irradiation excites the sample. The latent heat for phase transition of melting ΔH_m (Table 4.1) and evaporation ΔH_v are taken into account as a boundary condition of integration in temperature. The total enthalpy taken from an integration in temperature is approximated by

$$\Delta H(T) \approx \int_{T_o}^{T} \rho(T')C_p(T')dT' + \vartheta(T-T_m)\Delta H_m + \vartheta(T-T_v)\Delta H_v \tag{4.9}$$

where $\vartheta(T-T_m)$ is a Heaviside step function, T_m is melting temperature (Table 4.1), and T_v is evaporation temperature [1]. The first term describes the density of energy required to heat the material from the temperature T_o of solid to T of liquid or vapor. The specific heat that is dependent on the temperature, C_p(T), of the solid and the liquid phase is assumed to be equal, i.e., $C_p \sim C_{ps} \sim C_{pl}$ [93]. The error of this approximation mostly varies up to 20% for metals and 10% for nonmetals, respectively [93].

The second term describes the additional energy density of latent heat for melting, which is zero if $T < T_m$. The third term describes the latent heat of evaporation at the boiling point T_v, and vaporization may take place at temperatures at $T < T_v$.

Estimation of ablation threshold or ablation rate is approximated by the energy balance equation between absorbed photon energy and total enthalpy of the material. The total photon energy stored in the absorbed layer of semiconductors is represented by

$$[(1-R)I - I_L]\tau_p \cdot max[l_\alpha, l_D] \tag{4.10}$$

where R is the reflectivity of the sample, the absorption depth is $l_\alpha \approx 1/\alpha$, absorption coefficient is α, and fluence for loss is $F_L = I_L \tau_p$. I_L corrects for losses due to thermal radiation, heat conduction, free convection to air, etc, approximately given by

$$I_L(T) \approx \eta(T)(T - T_o) \tag{4.11}$$

where $\eta(T) = \eta_o((T - T_o)/T_o)^{1/4}$, and η_0 usually depends on the areas of substrates [1]. For the substrates with small areas of 2.5 mm^2 in this experiment, η_0 is around 10^{-5} $\text{W/cm}^2\text{K}$, as a scaling factor to make close fits to the experimental values of threshold melting fluences below.

Since the heat conductivity for crystalline insulators and semiconductors strongly depends on three phonon and higher processes, it decreases with increasing temperature. So, it seems reasonable to expect that the heat conductivity at much higher temperatures than Debye temperature (Table 4.1) can be described by

$$\kappa(T) \approx \frac{\kappa(T_o)}{(T/T_o)^n} = \frac{\kappa(T_o)T_o^n}{T^n} \tag{4.12}$$

with $1.20 \le n \le 1.55$ for many III-V compounds [1]. The exponent n is estimated from experimentally obtained thermal conductivities.

Table 4.1: Temperature independent parameters [1][94].

Parameter	ΔH_m [10^3J/cm^3]	Debye Temp [K]	Melting Temp [K]
$In_{0.53}Ga_{0.47}As$	0.47	330	1356
InP	0.51	425	1337
GaAs	0.55	360	1514
Si	1.78	640	1687

This formula is especially useful because no experiment has reported temperature dependence of heat conductivity for $In_{1-x}Ga_xAs$ ternary. For Si, the experimental data within 300 K < T < 1400 K are better fit with the inverse law of temperature. The maximal error of heat conductivity for $In_{1-x}Ga_xAs$ taken with n = 1.375 is less than 13 %, say 150 to 600 K, but for binaries, this power law works well above 1000 K, as fit from T_o to T_m in Table 4.2 [95].

Table 4.2: Temperature dependent parameters[a] [95][96][97][98].

Parameter	**Reflectivity** R	**Specific heat** C_p**[J/g]**
$In_{0.53}Ga_{0.47}As$	$0.40+5\times10^{-5}T$	$0.29+0.8\times10^{-4}T+87.69T^{2}$
InP	$0.34+5\times10^{-5}T$	$0.28+1.0\times10^{-4}T$ (T < 910 K) 0.378 (T > 910 K)
GaAs	$0.35+5\times10^{-5}T$	$0.302+0.8\times10^{-4}T+87.69T^{2}$
Si	$0.38+5\times10^{-5}T$	$0.748+1.68\times10^{-4}T$

a. Temperature dependent data are fit from references.

Density ρ**[g/cm^{3}]**	**Heat conductivity** κ**[W/cmK]**
$5.56+1.3\times10^{-4}(T-298)$	$154/T^{1.375}$
$4.793+0.8\times10^{-4}(T-298)$	$2890/T^{1.45}$
$5.336+1.3\times10^{-4}(T-298)$	$540/T^{1.2}$
$2.56+1.69\times10^{-4}(T-T_m)+1.75\times10^{-7}(T-T_m)^{2}$	$299/(T-99)$

For surface absorption of semiconductors, threshold fluence [J/cm^2] for melting or vaporization can be calculated, using Eq. (4.9) and (4.10).

$$F_{th} \approx \left(\int_{T_o}^{T} \rho(T')C_p(T')d(T') + \vartheta(T-T_m)\Delta H_m + F_L \right) \frac{max[l_{\alpha}, l_D]}{1-R(T)} + F_L \qquad (4.13)$$

Fig. 4.20 indicates the threshold fluence for melting and the necessary light energy to overcome the latent heat of melting. The kinks mean phase transition from solid to liquid phase, so two phases are mixed between top-fluence and bottom-fluence at the kinks. The threshold fluence for melting is defined by the top-fluence at the kinks. Based on the experimental results of Sec 4.5, the defects start to be generated around the melting temperature. As explained in Sec 4.6.1, high density defects will be generated in this phase when material removal due to the lattice weakening comes into play. The calculated melting threshold without taking into account vaporization is fairly matched with experimental results, as shown in Table 4.3.

To compare the wavelength effect of excitation at 1.064 μm with that at 532 nm, the threshold fluence at 1.064 μm excitation is calculated based on Eq. (4.13). The different parameters at 532 nm are the absorption coefficient α, the absorption length l_{α}, and the reflec-

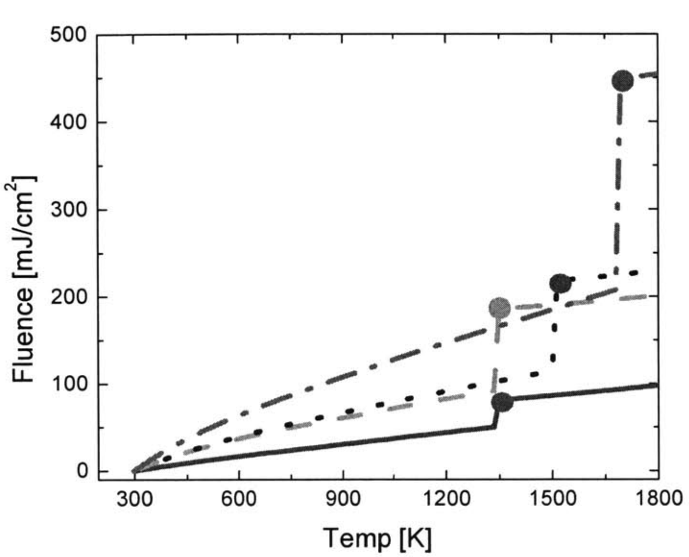

Figure 4.20: Temperature dependence of melting fluence with Nd:YAG lasers at 532 nm: InGaAs (Solid); InP (dash); GaAs (dot); Si (dash-dot). The dots at the kinks indicate the threshold fluence.

Table 4.3: A comparison of threshold fluences for melting between theoretical calculation and experimental determination, with Nd:YAG lasers at 532 nm [99][100].

Semiconductor	**Theoretical threshold Fluence [mJ/cm^2]**	**Experimental threshold Fluence [mJ/cm^2]**	
	3 ns	**3 ns**	**15 ns**
$In_{0.53}Ga_{0.47}As$	81	none	none
InP (100)	185	170±50	200
GaAs (100)	218	250±50	none
Si (111)	448	500±50	470

tivity R. This absorption length turns out the same as the depth of semiconductor, $l_\alpha = \Delta h$. Furthermore, Eq. (4.12) needs to be divided by the absorption correction factor of $(1\text{-}e^{\alpha_{1064\mathrm{nm}}\Delta h})$, because 1064 nm photons do not completely absorbed in the capping layers. For $In_{0.53}Ga_{0.47}As$ which absorbs 1.064 μm, thus, the threshold fluence for melting is 260 mJ/cm^2.

4.7 Discussion

The threshold fluence for melting of $In_{0.53}Ga_{0.47}As$ at 1.064 μm excitation is calculated to be 260 mJ/cm^2, which is close to the threshold fluence for bandgap shift of 230 mJ/cm^2 for the bandgap shift as reported in [89]. Likewise, the threshold fluence of melting at 532 nm is calculated to be 81 mJ/cm^2, which is close to the threshold fluence for bandgap shift of 65 mJ/cm^2 according to the measurement. Hence, based on experimental conclusions in Sec.4.5.4, significant defects might be generated, and significant bandgaps are thus shifted at around the fluence of melting on the substrate excited either by 1.064 μm or by 532 nm. The longer interaction length at 1.064 μm excitation needs the higher threshold for melting and bandgap shifts than 532 nm excitation. From the PLAID process of 6000 pulses, I obtain the maximal bandgap shifts of 33 nm with the fluence of 300 mJ/cm^2 at 1.064 μm excitation and 45 nm with the fluence of 125 mJ/cm^2 at 532 nm excitation.

Chapter 5

Unidirectional Semiconductor Ring Lasers

5.1 Unidirectional Semiconductor Ring Lasers for High Density Circuit Integration

5.1.1 Introduction

Photonic integrated circuits (PIC) [18][101] have the potential to satisfy the need for telecommunication devices in the trend toward high capacity global networking. In this context, integrated semiconductor lasers [102][103] will be associated with various photonic circuits [104], e.g. optical amplifiers, wavelength converters, transceivers, and routers. However, the necessary microphotonic laser integration techniques have not been developed for densely integrated devices, mainly because of two fabrication limitations: the cleaved-facet necessity of Fabry-Perot lasers (FPL) and the vertical output coupling of vertical cavity surface emitting lasers (VCSEL). Distributed feedback and distributed Bragg grating lasers have been limited to one-dimensional integration because of the inflexibility of lithography for fabricating gratings. Whereas the vertical packaging solution in VCSELs is not sufficient to provide elaborate horizontally guided optical beam delivery system [105].

Since monolithic semiconductor ring lasers do not need cleaved facets, these lasers can be easily integrated with other types of sophisticated photonic devices [106]. High-Q microring resonators have been adopted for dense wave-division [107] multiplexing as well as time-division multiplexing systems of PIC with well-known linear and nonlinear characteristics [108]. The ring size that is determined by lithography has precision that the cleaved facets of FPL cannot achieve. Consequently, the definite ring size determined by lithography can provide well-controlled repetition rates in mode-locked operation [109][110]. Furthermore, the traveling wave operation in unidirectional ring lasers eliminates spatial hole burning, and results in high side mode suppression ratios (SMSR) as well as reduced sensitivity to feedback [106]. The high SMSR is expected to reduce mode partition noise. Also, unidirectional ring lasers are robust, because spurious intracavity reflections can be dumped into the nonlasing direction of propagation within the resonator. Although numerous semiconductor ring lasers have been fabricated, such as squared [111], tetragonal [112], triangular [113], circular resonator [114][115][116], and microdisk [117], most of them have not eliminated mode-competition between bi-directionally propagating lasing modes. Squared and triangular-shaped ring lasers can take advantage of low loss by use of total internal reflection facets and straight waveguides. However, triangular lasers require additional output waveguides for PIC applications. For square lasers, light coupled into the output waveguide is scattered and diffracted at the deeply etched facets and corners.

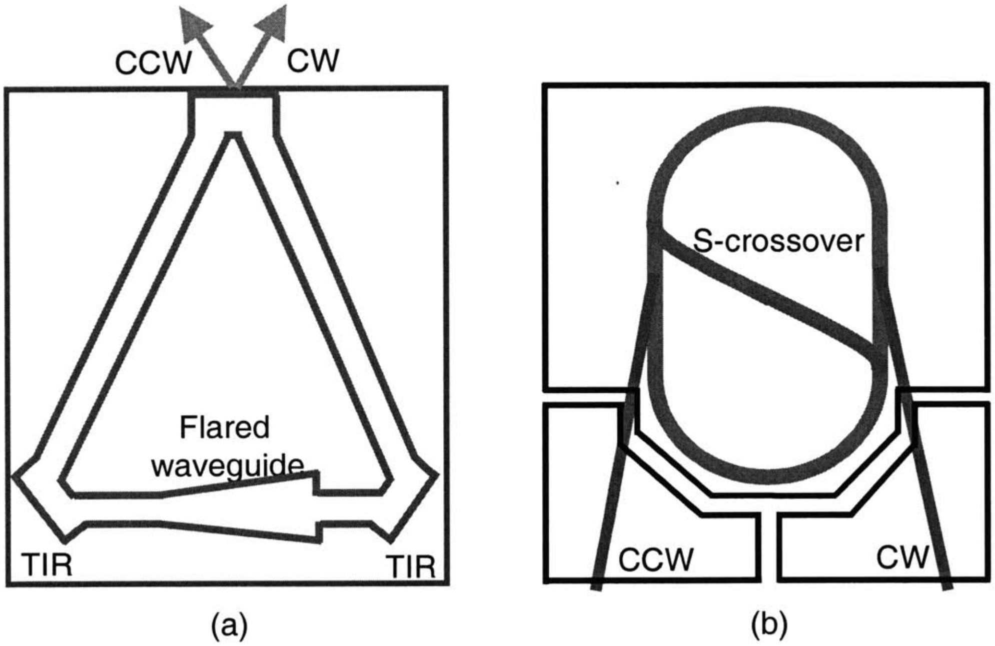

Figure 5.1 (a) An integrated triangular unidirectional ring laser; TIR, total internal reflecting mirror. (b) An integrated S-crossover unidirectional ring laser (adapted from [35] and [36]).

Ring lasers are inherently bi-directional due to the reciprocity of the gain medium in the ring resonator, so most ring laser systems need a Faraday isolator to obtain unidirectional operation. Unfortunately, monolithically integrable isolators are not available today. Recently, unidirectional operation has been achieved for square [118], triangular [119], and circular lasers [106][120]. In square ring lasers, unidirectional operation has been demonstrated by controlled feedback from external cavities. In triangular ring lasers, unidirectional operation has been demonstrated by asymmetrical flared ridge waveguides fabricated in GaAs/AlGaAs using graded-index separate-confinement heterostructures (Fig. 5.1(a)). The flared waveguide as an optical diode only provides non-reciprocal transmission for multimode waveguides. In semiconductor circular lasers, unidirectional operation has been demonstrated by breaking reciprocity of the ring resonator with an S-crossover segment in polyimide-embedded GaAs/AlGaAs rib-waveguide structures (Fig. 5.1(b)). In these circular lasers, the active S-crossover waveguide couples light directly to the ring resonator and successfully introduces a nonreciprocal gain into the ring. Although unidirectional operation has been demonstrated with an active S-crossover waveguide, single transverse mode operation and any theoretical analysis has not been presented.

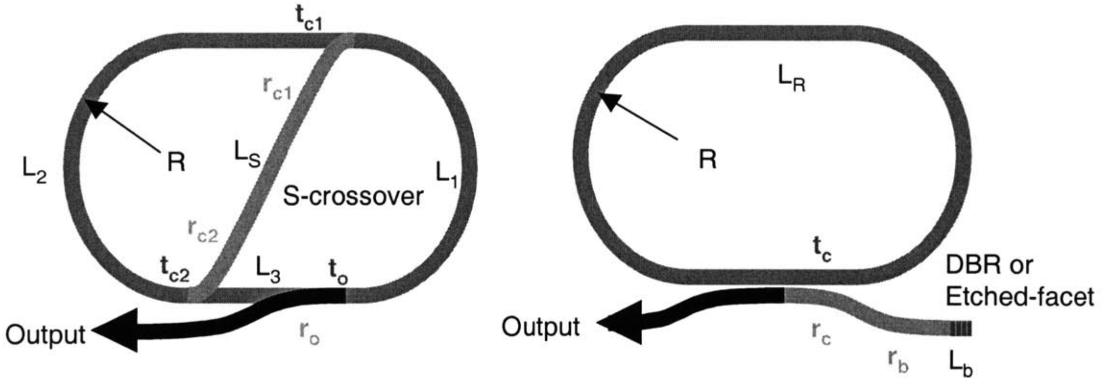

Figure 5.2 (a) A unidirectional ring laser resonator into which an S-crossover waveguide is incorporated; L_1, the length of right half segment; L_2, the length of left half segment; L_S, the length of the S-crossover segment; L_3, the length of a segment from CW output port to Y-branch on the bottom; r, bend transmission coefficient from the straight waveguide to the S-crossover waveguide; t, transmission coefficient from the straight waveguide to straight waveguide. (b) A unidirectional ring laser resonator into which a distributed Bragg reflector or an etched facet is incorporated; L_R, the length of the ring; L_b, the length of retro-arm; R, the radius of curvature.

I design and analyze unidirectional continuous wave circular lasers without using an isolator in the beam path. These lasers operate in a single transverse mode at telecommunication wavelengths [120]. To enforce the unidirectional and single transverse mode operation, I carefully design a ring laser with the S-crossover waveguide based on the cascaded scattering matrix (S matrix) analysis (Fig. 5.2(a)). For the directional light coupling from the ring to crossover waveguide and to the output waveguide, asymmetric Y-branches are introduced. The S matrix components of these Y-branches are obtained with finite difference time domain (FDTD) simulation (Appendix A). Another approach to unidirectional operation with a ring resonator is to use a slave arm with a retro-reflecting mirror [120][121]. This technique has been employed for unidirectional operation of He-Ne ring lasers [122] and Kerr-lens mode-locked Ti:Sapphire ring lasers (Fig. 5.2(b)) [123]. As I will show, these lasers have lower intracavity losses than the S-crossover lasers because of reduced radiation loss for evanescent couplers.

By means of path integration based on cascaded S matrices, the resonance filter properties of S-crossover and retro-reflected laser systems are derived (Appendix B). For these semiconductor ring lasers, I develop a coupled rate equation model to demonstrate unidirectionality of laser operation. The coupled carrier density and photon density rate equations predict the light output power versus the driving current (L-I) curves where injected photons are coupled from the CCW (counter-clockwise) direction to the preferred CW (clockwise) direction. I theoretically analyze reciprocity breaking phenomena with the output power ratio between the two directions of propagation, which I refer to as the counter-mode suppression ratio (CMSR).

To verify the model, hybrid semiconductor fiber ring lasers are developed to demonstrate unidirectionality, with macroscopic S-crossover waveguides or fiber pigtailed retro-reflectors. These macroscopic prototype lasers are made with semiconductor optical amplifiers (SOA) as gain media as well as with single mode optical fibers as waveguides. A large CMSR of 21.5 dB in macroscopic S-crossover lasers and 24.5 dB in macroscopic retro-reflected lasers is demonstrated.

5.2 Theory of Integrated Unidirectional Ring Lasers

5.2.1 Resonance Properties of Unidirectional Ring Lasers

With the S matrix that is derived in Appendix I, I focus on the overall S matrix analysis of the ring laser structure where the cosine S-bend crossover waveguide links two ring segments with two asymmetric Y-branches. The input wave is incident on the output port, and then circulates in the CW or CCW direction affected by the S-crossover waveguide. Subsequently, part of the incident wave is reflected back to the output port, depending on how many times the incident wave circulates around the ring resonator. By cascading the S matrix at each Y-branch along the resonator, I obtain the relative amplitude and phase of the overall S matrix. Thus resonance filter properties are obtained from the electric field of the output beam, which is diagrammatically modeled by path integration [124] using the overall S matrix of the ring resonator.

The overall reflectivity of the S-crossover ring resonator, as shown in Fig. 5.2(a), is given by Eq. (5.1) with a unit input from the output port, where all coefficients are subscripted with the top Y-junction *c1*, the bottom junction *c2*, and the output junction *o*. The straight transmittance T and the bend transmittance R are represented by κt^2 and κr^2, respectively, according to Eq. (A.2) and (A.4). The amplitude and phase of the output beams is derived in Appendix II and represented in terms of the phase offset θ, the effective refractive index n, the emission wavelength λ, and the length of ring resonator L_R. It is interesting to note that the S-crossover waveguide does not affect the resonance property because the light beams pass only once through the S-crossover segment compared to their infinite times in the ring.

$$Ref_S = 4R_{c1}R_{c2}T_{c1}\left[\frac{R_o}{1 + T_oT_{c1}T_{c2} - 2\sqrt{T_oT_{c1}T_{c2}} \cdot \sin(2\pi nL_R/\lambda + \theta)}\right]^2 \tag{5.1}$$

Fig. 5.3(a) plots the overall-reflectivity Ref_S versus wavelength for three different choices of the transmission coefficient with the constant radiation loss α of 20% in Eq. (A.2). It is evident that the ring resonator acts as a Fabry-Perot band pass filter, with a periodic reflectivity whose bandwidth depends on the Q-value of the resonator and peak values of the reflection depend on the transmission through the S-crossover waveguide.

The overall reflectivity of the retro-reflected ring resonator, as shown in Fig. 5.2(b), is given by Eq. (5.2) and by taking the same method of path integrations. Similar to the S-crossover waveguide, the length of the retro-reflector arm does not affect the resonance properties. However, the reflected power linearly depends on the reflectivity of the retro-reflector R_b.

$$Ref_R = R_b\left[\frac{(T_c + R_c)^2 + T_c + 2(T_c + R_c)\sqrt{T_c} \cdot \sin(2\pi nL_R/\lambda + \theta)}{1 + T_c + 2\sqrt{T_c} \cdot \sin(2\pi nL_R/\lambda + \theta)}\right]^2 \tag{5.2}$$

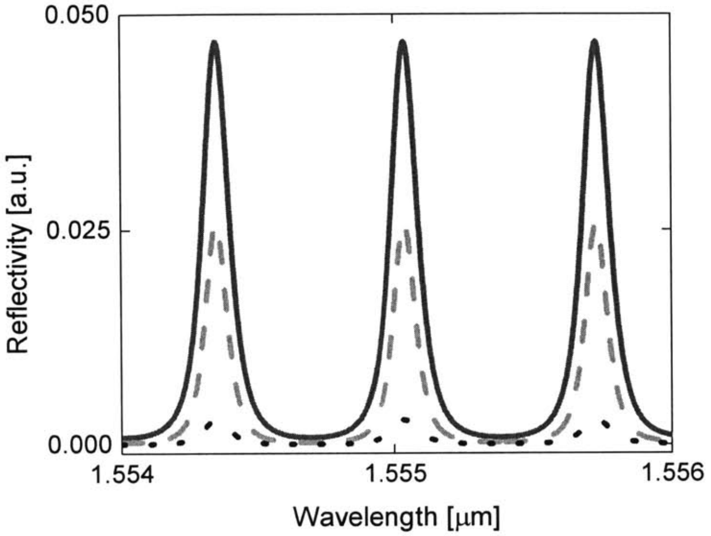

Figure 5.3 Overall reflectivity of an S-crossover ring laser in wavelength domain is plotted with three different transmissions at Y-junctions, $\kappa = 0.8$ and $\theta = \pi$, $i = c1$, $c2$, and o; $R_j = 0.2$, $T_j = 0.6$ (solid); $R_j = 0.15$, $T_j = 0.65$ (dash); $R_j = 0.1$, $T_j = 0.7$ (dot).

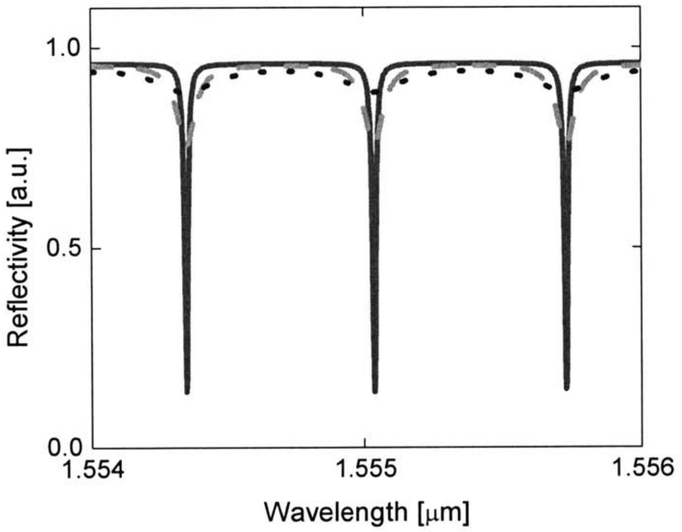

Figure 5.4 Overall reflectivity of a retro-reflected ring laser in wavelength domain is plotted with three different transmissions at an evanescent coupler, $\kappa = 0.98$ and $\theta = 0$, and $R_b = 1$; $R_c = 0.08$, $T_c = 0.9$ (solid); $R_c = 0.48$, $T_c = 0.5$ (dash); $R_c = 0.88$, $T_c = 0.1$ (dot).

Similarly, Fig. 5.4 plots the wavelength dependent overall-reflectivity Ref_R for three different choices of the transmission coefficient. The bandwidth of reflection spectra in Fig. 5.4 is much narrower than in Fig. 5.3, because much less radiation loss of 5% is assumed at the evanescent coupler.

5.2.2 Coupled Rate Equations for Unidirectional Ring Lasers

I develop a rate equation model for charged carriers in semiconductor active regions and for their subsequent photon generation process toward a preferred direction of propagation. In this model, I do not consider a coupled phase effect since the output intensity tends to be dominant for one direction at the expense of the other. For unidirectional operation, strong coupling to the preferred direction is provided by the S-crossover waveguide or the retro-reflector, as shown in Fig. 5.2(a) and Fig. 5.2(b). Also, the carrier density and the photon lifetime in the CW direction are identical to those in the CCW direction. The photon density equation should be modified by the additional term that includes the contribution of coupled photons. Based on rate equations in simple bi-directional ring lasers [32], I obtain coupled photon and carrier density rate equations, where injected photons are coupled from the CCW direction to the preferred CW direction.

$$\frac{dN}{dt} = G-(R_{rec,cw}+R_{rec,ccw}) \tag{5.3}$$

$$\frac{dS_{ccw}}{dt} = \Gamma R_{st,ccw}+\Gamma\beta R_{sp,ccw}-\frac{S_{ccw}}{\tau_l} \tag{5.4}$$

$$\frac{dS_{cw}}{dt} = \Gamma R_{st,cw}+\Gamma\beta R_{sp,cw}+S_{couple}-\frac{S}{\tau_l} \tag{5.5}$$

For a double hetero-structure active region, injected currents generate carriers which recombine by radiative and nonradiative processes. So, the carrier density rate equation is given in Eq. (5.3), where G is the rate of injected electrons $\eta_i I/qV_a$, and $R_{rec,cw}$ and $R_{rec,ccw}$ are the rate of recombining CW and CCW electrons per unit volume in the active region, respectively. Other parameters are the current I, the internal quantum efficiency η_i, the electric charge q, and the volume of the active region V_a. The two directional $R_{rec,j}$ can be summarized to $AN+BN^2+CN^3+R_{st,j}$ (j is cw *or* ccw) where the terms of electron density represent the leakage A, the bimolecular recombination B, and the Auger recombination C, and $R_{st,cw}$ and $R_{st,ccw}$ are the stimulated emission rate for CW and CCW, respectively. Also, the rate equation of the CCW photon density S_{ccw} is given in Eq. (5.4), where there are the confinement factor Γ, the spontaneous emission factor β, the photon lifetime τ_l, and the CW and CCW spontaneous emission rate $R_{sp,cw} = R_{sp,ccw} = BN^2$. The rate equation of the CW photon density Scw has the additional term representing coupled photons from the CCW direction, Scouple, in Eq. (5.5).

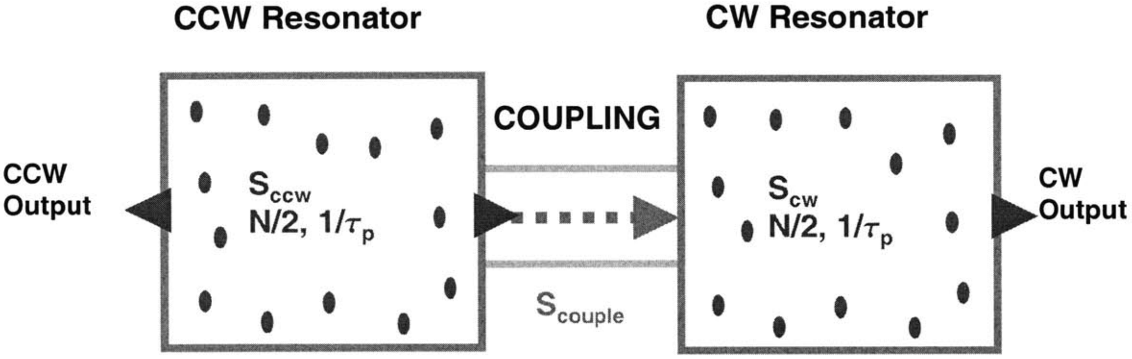

Figure 5.5 Conceptual diagram of unidirectional lasers with a directional coupling S_{couple}, where both CW and CCW resonators have identical carrier densities and photon lifetimes and dots represent photons.

The photon lifetime τ_l for the CW and CCW directions are the same by reciprocity of two directions of propagation along the ring waveguide. As illustrated in Fig. 5.5, the photon lifetime for *CCW* includes not only the output coupling to the CCW output port but also coupling to CW. However, since I design the unidirectional lasers to couple intracavity photons only from the CCW direction to the CW direction, the photon lifetime for CW does not include coupling to CCW.

$$\frac{dN_R}{dt} = \frac{\eta_i I_R}{qV_a} - v_g g_R(S_{ccw} + S_{cw}) - (AN_R + BN_R^{\ 2} + CN_R^{\ 3}) \tag{5.6}$$

$$\frac{dS_{ccw}}{dt} = \Gamma v_g g_R S_{ccw} + \Gamma \beta B N_R^{\ 2} - \frac{S_{ccw}}{\tau_l} \tag{5.7}$$

$$\frac{dS_{cw}}{dt} = \Gamma v_g g_R S_{cw} + \Gamma \beta B N_R^{\,2} + S_{couple} - \frac{S_{cw}}{\tau_l} \tag{5.8}$$

For Eq. (5.6) to (5.8), half of the spontaneous emission at the ring as well as at the S-crossover waveguide goes for the CW and the other half goes for the CCW, where the subscripts of R denote parameters in the ring. v_g is the group velocity which is defined to be c/n_g, where c is the velocity of light, and n_g is the group refractive index. The gain coefficient of the ring g_R is given by $g_R\ln(N_R/N_{Ro})$. The gain coefficient of the S-crossover waveguide g_S is given by the measured experimental value rather than by the fitted value to provide the gain saturation of the SOA. N_R and N_{Ro} are the carrier density and the transparency carrier density in the ring, respectively.

5.2.3 Coupled Equations for S-crossover Ring Lasers

In the S-crossover ring lasers, the intracavity photons of the CCW direction couple to those of the *CW* direction through two asymmetric Y-couplers in the S-crossover waveguide during each round trip. The fraction of the coupled photons relative to the round trip photons flows into the S-crossover segment at an inverse rate of resonator roundtrip time, $1/\tau_R$ [6]. The coupled photons are then amplified in the active segment of the S-crossover waveguide with the gain of , where there are the gain coefficient g_S, the length of S-crossover segment L_s, the internal loss $\exp((\Gamma g_S - \alpha_i + \ln(T_m))L_s)$, and the transmittance in the fiber-pigtailed SOA T_m, and Γ is identical to that in the ring. After all, the amplified photons leave for the ring with another bend transmission of R_{c1} or R_{c2}, which is summarized in the first term with in Eq. (5.9).

$$S_{couple} = e^{(\Gamma g_S - \alpha_i + \ln(T_m))L_S} R_{c1} R_{c2} \left(\frac{1}{T_{c1}} + \frac{1}{T_{c2}}\right) \frac{1}{\tau_R} S_{ccw} + (R_{c1} + R_{c2}) \beta B N_R^{\,2} \tag{5.9}$$

$$\frac{1}{\tau_l} = \frac{1}{\tau_R}\left[\alpha_i L_R + \ln\left(\frac{1}{T_m T_{c1} T_{c2} T_o}\right)\right] \tag{5.10}$$

Furthermore, the second term shows the power flow of the amplified spontaneous emission as it leaves, with the two bend transmissions, a perfectly inverted gain medium to the ring. Eq. (5.9) enumerates two distinct couplings from the top and the bottom at the two Y-junctions of the S-crossover waveguide and the ring, subscripted with $c1$ and $c2$. The mirror losses are calculated with different straight transmissions of T_{c1} at $c1$, T_{c2} at $c2$, and T_o at the output coupler. The resonator round trip time $1/\tau_R$ equals L_R/v_g in Eq. (5.10), where L_R is the length of the ring resonator, and N_S is the carrier density in the S-crossover segment.

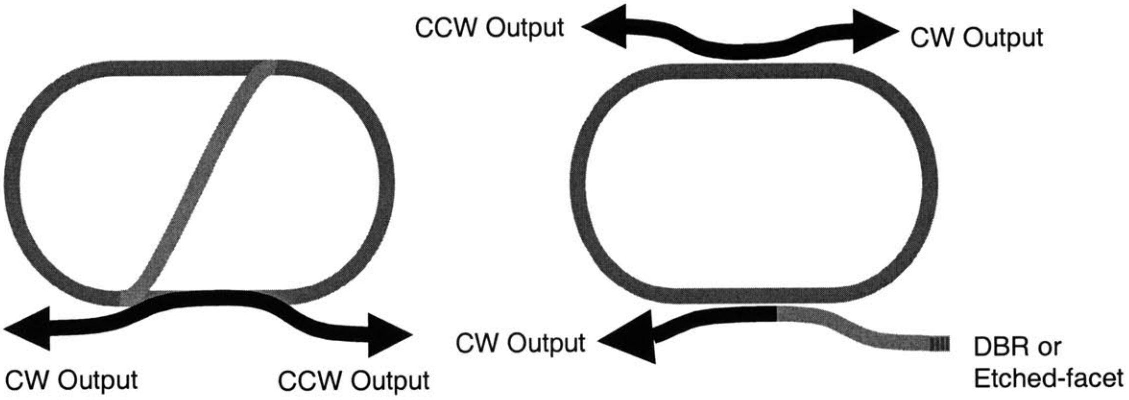

Figure 5.6 (a) An S-crossover ring laser with two output arms. (b) A retro-reflected ring laser with two output arms.

I carefully design the integrated S-crossover ring lasers that have two directional outputs to prove unidirectionality of laser operation as shown in Fig. 5.6(a). In the figure, two additional couplers can be introduced to monitor the relative intracavity power in the CW and CCW directions. When the laser is operating bi-directionally, e.g., when the term S_{couple} goes to zero, then the two tap couplers will have identical output powers. So I can analyze steady state solutions of S_{cw}, S_{ccw}, and I to derive L-I curves for the CW and CCW directions based on the coupled rate equations of Eq. (5.6) to (5.10). The two directional output powers are given as functions of the current to the S-segment and to the ring in Eq. (5.11), where ν is the optical frequency, F is the fractional power extraction factor, and V_a is the active region volume. Hence, the output power ratio between the two directions of propagation, *CMSR*, is given in Eq. (12).

$$P_{out,j}(I_S, I_R) = F\frac{1}{\tau_R}\ln\left(\frac{1}{T_o}\right)h\nu S_j(I_S, I_R)\frac{V_a}{\Gamma} \tag{5.11}$$

$$CMSR(I_S, I_R) = \frac{S_{cw}(I_S, I_R)}{S_{ccw}(I_S, I_R)} \tag{5.12}$$

where *j* is *CW* or *CCW*.

5.2.4 Coupled Equations for Retro-reflected Ring Lasers

In the retro-reflected ring lasers, the intracavity photons of the CCW direction flow into the CW direction through an evanescent coupler. A fraction of the coupled photons, relative to the roundtrip photons, flows into the retro-reflector arm at an inverse rate of resonator round trip time $1/\tau_R$. The outgoing photons are next reflected back at the retro-reflector with the reflectivity of R_b. Finally, the retro-reflected photons leave for the ring with another transmission of R_c, which Eq. (5.13) summarizes. Photon density and carrier density equations are identical to those in the S-crossover laser except the coupled-photon density and the photon lifetime given in Eq. (5.13) and (5.14), respectively.

$$S_{couple} = R_b \frac{R_c^2}{T_c} \frac{1}{\tau_R} S_{ccw} \tag{5.13}$$

$$\frac{1}{\tau_l} = \frac{1}{\tau_R}\left[\alpha_i L_R + \ln\left(\frac{1}{T_m T_c T_o}\right)\right] \tag{5.14}$$

CW and CCW tap couplers are added to the retro-output arm, by use of an evanescent coupler in which the out-coupling is T_o, as shown in Fig. 5.6. The two directional output powers and the *CMSR* are given as functions of the current to the ring and the reflectivity in the retro-reflector in Eq. (5.15) and (5.16), respectively.

$$P_{out,j}(I_R, R_b) = F\frac{1}{\tau_R}\ln\left(\frac{1}{T_o}\right) h\nu S_j(I_R, R_b)\frac{V_a}{\Gamma} \tag{5.15}$$

$$CMSR(I_R, R_b) = \frac{S_{cw}(I_R, R_b)}{S_{ccw}(I_R, R_b)} \tag{5.16}$$

The retro-output power is given by both the output power from the ring resonator with the out-coupling T_c and the output power from retro-reflector with the out-coupling R_c, at the retro-arm, in Eq. (5.17). The first term is dominant, because the out-coupling R_c is much larger than T_c, and the CW power becomes dominant as the retro-reflectivity increases.

$$P_{retro}(I_R, R_b) = F\frac{1}{\tau_R}h\nu\left[\ln\left(\frac{1}{T_c}\right)S_{cw}(I_R, R_b) + R_bR_cS_{ccw}(I_R, R_b)\right]\frac{V_a}{\Gamma} \tag{5.17}$$

$$\cong F\frac{1}{\tau_R}h\nu\ln\left(\frac{1}{T_c}\right)S_{cw}(I_R, R_b)\frac{V_a}{\Gamma} \tag{5.18}$$

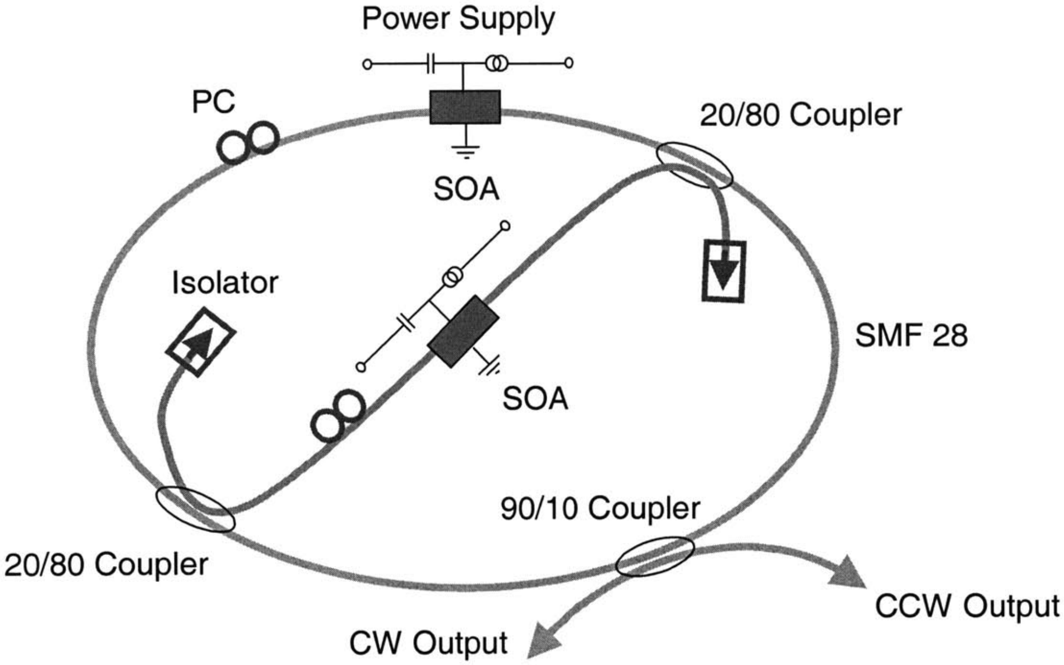

Figure 5.7 Unidirectional macroscopic hybrid ring laser into which an S-crossover fiber is incorporated. The laser consists of an SOA and single mode fibers. The circulating beam is coupled out with a 90% evanescent fiber coupler; SMF28, Corning single mode fiber at 1.55 μm; PC, polarization controller.

5.3 Macroscopic Unidirectional Hybrid Ring Lasers

5.3.1 Gain and Internal Parameter Measurement of SOA

Hybrid semiconductor fiber ring lasers have been developed to demonstrate unidirectional operation without isolators in the beam path, with macroscopic S-crossover waveguides or fiber pigtailed variable retro-reflectors. These macroscopic prototype lasers are made with

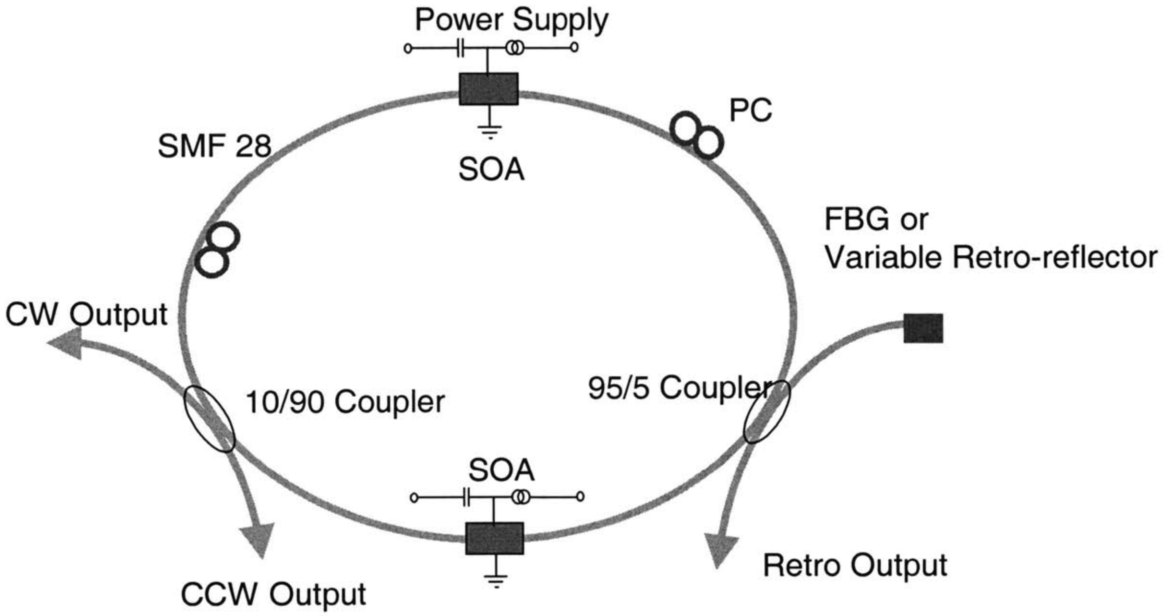

Figure 5.8 Unidirectional macroscopic hybrid ring laser into which a variable retro-reflector of a fiber Bragg grating (FBG) is incorporated. The circulating beam is coupled out with a 10% evanescent fiber coupler.

semiconductor optical amplifiers (SOA) as gain media and with single mode optical fibers (SMF28) as ring waveguides, shown in Fig. 5.7 and Fig. 5.8. These macroscopic lasers are similar to integrated semiconductor ring lasers, except that the gain is concentrated on the SOA instead of being distributed along the ring. In addition, these lasers allow us to vary parameters such as retro-reflectivity easily so as to verify the theoretical model. Table 1 displays parameter values of the SOA in which some values are measured λ, g, α_i, η_i, or adapted from similar SOA (L, w, d, Γ_t, n_g, β) and (A, B, C) [125] because they are comparable for our SOA. Some parameters might have some errors according to the slight difference in the design of our SOA from similar ones as well as to the measurement uncertainty.

The values for important internal parameters of the internal loss α_i and the differential quantum efficiency η_i are commonly determined from L-I curves of hybrid bi-directional ring lasers with a single SOA or doubly cascaded SOA. With two different output couplers, two L-I curves are measured to obtain two different mirror losses and differential quantum efficiencies of α_{m1} and α_{m2} as well as η_{m1} and η_{m2}, respectively. Once these parameter values are set, the internal loss and internal quantum efficiency are calculated from Eq. (5.18) and (5.19),

TABLE 5.1 Parameter values used in rate equations.

Parameter	Symbol	Value	Value
Length of active region; S-crossover/Retro ring	L_R, L_S	750/1500	μm
Depth of active region	d	0.25	μm
Width of active region	w	2.5	μm
Transversal confinement factor	Γ	0.3	
Coupling transmittance in the fiber-pigtailed SOA	T_m	0.2	
Group refractive index	n_g	3.56	
Internal quantum efficiency; one SOA/two SOA	η_i	0.65/0.85	
Internal loss	α_i	30	cm^{-1}
Spontaneous-emission factor (multimode)	β	0.001	
Gain coefficient; one SOA/two SOA	g_{Ro}	500/300	cm^{-1}
Transparency carrier density; one SOA/two SOA	N_{Ro}	$8.65\times10^{17}/6.65\times10^{17}$	cm^{-1}
Nonradiative recombination rate	A	5×10^{17}	sec^{-1}
Radiative recombination rate	B	1.0×10^{-10}	$cm^{-3}sec^{-1}$
Auger recombination rate [125]	C	8.0×10^{-29}	$cm^{-6}sec^{-1}$

which are displayed in Table 5.1. Note that the power fraction factor *F1* and *F2* should be included to refer to the actual power delivered out of the laser resonator, because radiation loss at the fiber coupler cannot be ignored.

$$\alpha_i = \alpha_{m1}\left(\frac{F_1}{F_2} - \frac{\eta_{d1}}{\eta_{d2}}\right) \Big/ \left(\frac{\eta_{d1}}{\eta_{d2}} - \frac{F_1\alpha_{m1}}{F_2\alpha_{m2}}\right) \tag{5.19}$$

$$\eta_i = \frac{\eta_{d1}}{F_2}\left(1 - \frac{\alpha_{m1}}{\alpha_{m2}}\right) \Big/ \left(\frac{\eta_{d1}}{\eta_{d2}} - \frac{F_1\alpha_{m1}}{F_2\alpha_{m2}}\right) \tag{5.20}$$

where $F_i = R_i/2(1-T_i)$, $i=1,2$.

The SMF28 pigtailed SOA in the macroscopic S-crossover hybrid ring lasers provide nearly polarization insensitive gain of 25 dB with 300mA current centered at 1540 nm, and have a saturation power of 10 dBm and a gain bandwidth of 76 nm (JDS Uniphase CQF872). I experimentally evaluate the frequency-dependent gain coefficients and the transparency-carrier densities of the SOA from fits to the gain curves as a function of frequencies using an optical spectrum analyzer (HP70950B) and a frequency tunable laser source (HP81640A). From fixed input powers of 5 μW and frequencies of 1510 nm to 1620 nm, the measured gain of a single SOA as well as a doubly cascaded SOA is fitted to $g_{Ro}\ln(N_R/N_{Ro})$. For this measurement, two fiber pigtailed isolators are used before and after the SOA to prevent lasing during the measurement. By calibrating the loss in the isolators, I measure the frequency-dependent gain with different bias currents in Fig. 5.9.

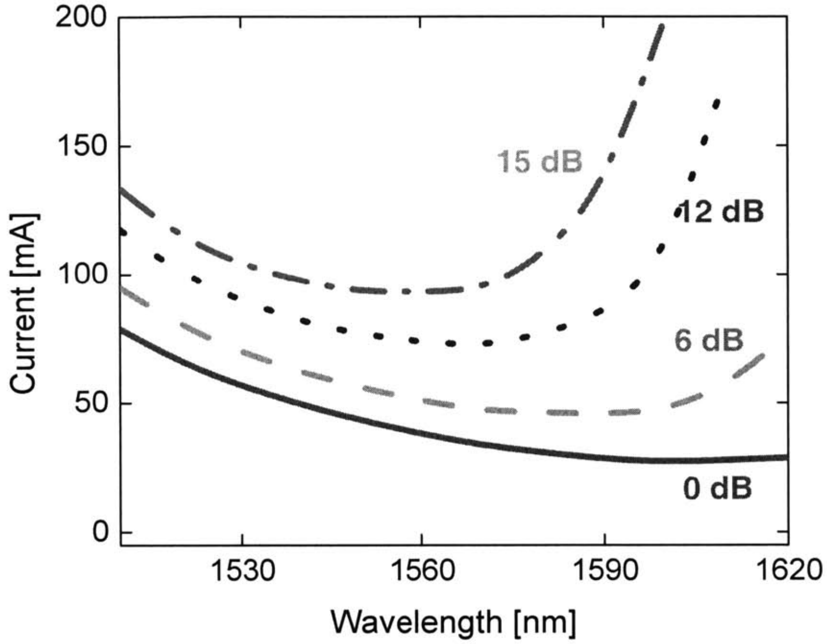

Figure 5.9 Gain contours of current versus wavelength. The contours of a constant gain are separated by 3 dB.

The SOA emits a significant amount of spontaneous emission from 5 mW to 9 mW with the bias current of 400 mA, without external inputs. As the bias current increases from zero to 400 mA, the center of the spontaneous emission shifts from 1560 nm to 1510 nm due to band filling. The emission wavelength and its threshold current can be predicted by taking the minimum value of the bias current from current contours in Fig. 5.9, with the known loss of a laser resonator.

5.3.2 S-crossover Hybrid Ring Lasers

Theoretical Predictions

As a prototype approach to an integrated S-crossover ring laser, the macroscopic version of a unidirectional S-crossover hybrid ring laser is developed without using isolators inside the laser resonator, as shown in Fig. 5.7. The parameter values of this laser are shown in Table 1. The lateral confinement factor Γ should be multiplied by the axial confinement factor Γ_L, in Eq. (5.4) through Eq. (5.7). The Γ_L equals L_R/L, where L_R and L is the length of the SOA in the ring and the ring resonator, respectively, because the gain is concentrated on the SOA. The ring is 10 m long, and S-segment is 6 m long.

Based on Eq. (5.11), the L-I curves for CW and CCW beams in the S-crossover ring laser are plotted with fixed currents in the S segment in Fig. 5.10(a) and Fig. 5.10(c), respectively. As the *S* current increases from zero to 400 mA, the threshold current of CW lasing decreases from 71 mA to 63 mA. Also, the differential quantum efficiency of CW lasing increases, and that of CCW lasing is conversely suppressed to the spontaneous emission level. Spontaneous emission floors below threshold increase according to the increasing the *S* current. Fig. 5.11(a) shows the calculated unidirectionality of lasing due to reciprocity breaking as the *S* current, so called the reciprocity breaking current, IS increases and the ring current I_R is fixed. When the *S* current goes to zero, the CW and CCW output powers are degenerate. As the S current increases, then the degenerate powers bifurcate to the higher power level for the CW direction and in contrast to the lower power level for the CCW direction.

Fig. 5.12(a) and Fig. 5.12(c) show *CMSR* predictions with constant currents to ring and with constant currents to the S segment, respectively. Below the lasing threshold, a larger *CMSR* is predicted than over threshold in Fig. 5.12(a). This phenomenon is explained by spontaneous emission, the second term in Eq (5.9), which exclusively couples from the *S* segment to the ring along the CW direction. As larger currents drive the SOA in the *S* segment, larger *CMSR* is predicted due to the increase of spontaneous emission floor. The *CMSR* curves are at minima around the threshold current of lasing in the ring. The *CMSR* is distinctively saturated after the currents to the S segment of 200 mA, regardless of the current level to the ring, as shown in Fig. 5.12(c). Above the lasing threshold, a maximal *CMSR* of 22.5 dB is predicted.

Experimental Results

As shown in Fig. 5.7, isolators, after a 20/80 evanescent 2×2 coupler, block reflections at the unused port; this loss is similar to radiation loss in the integrated Y-branch. The 20/80 coupler

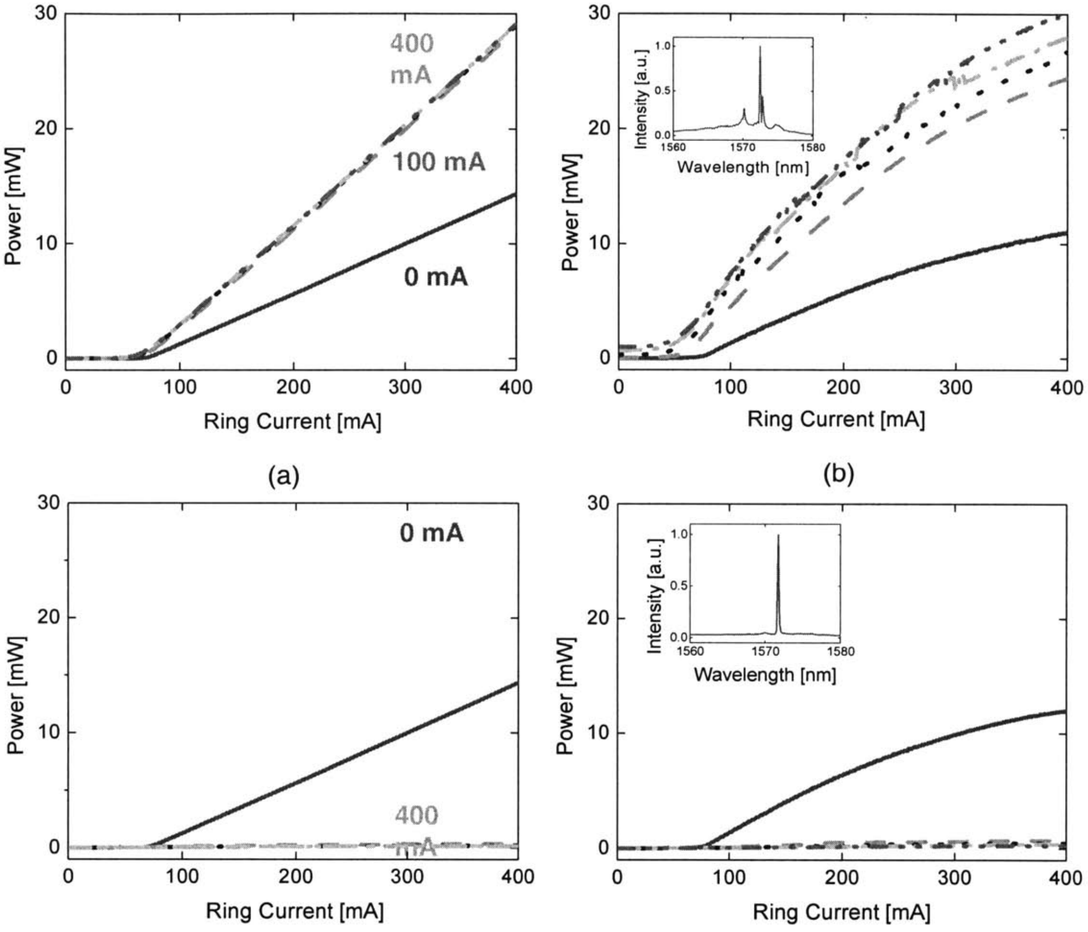

(a) (b)

(c) (d)

Figure 5.10 Calculated L-I curves in an integrated S-crossover ring laser as the S currents are constant and the ring current increases; (a) CW direction (c) CCW direction. Measured L-I curves in an S-crossover hybrid semiconductor ring laser; (b) CW direction (d) CCW direction; 0 mA (solid); 100 mA (dash); 200 mA (dot); 300 mA (dash-dot); 400mA (dash-dot-dot).

is used at the junction to match the same coupling into the S-crossover segment as is designed in integrated semiconductor ring lasers, and the 90/10 output coupler is used to increase the output power. When the transmission through the S-crossover segment goes to zero, this laser is identical to a simple ring laser with counter-propagating modes of equal intensity.

The L-I curves for CW and CCW beams in the S-crossover ring laser are measured with fixed currents in the *S* segment in Fig. 5.10(b) and Fig. 5.10(d), respectively. As the *S* current increases from zero to 400 mA, the threshold current of CW lasing decreases from 71 mA to 45 mA but the spontaneous emission noise increases. The differential quantum efficiency of

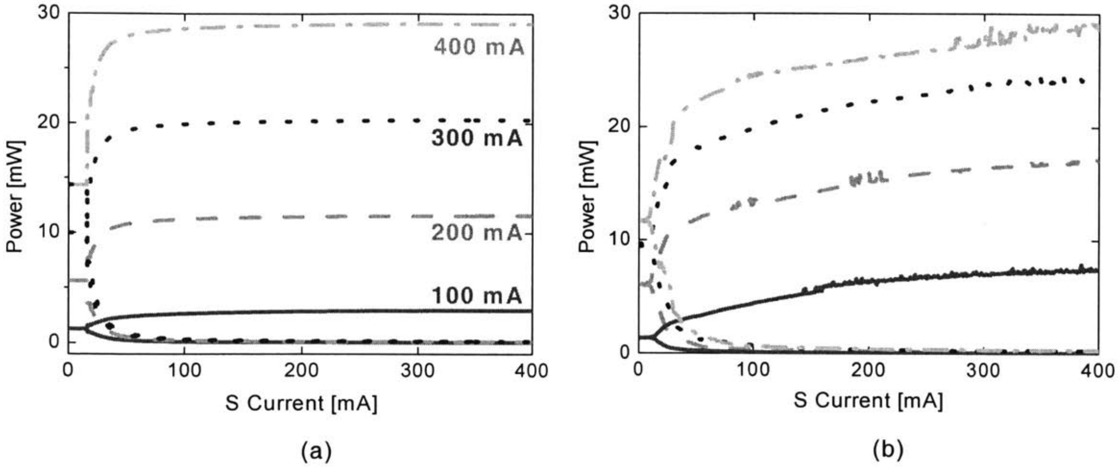

Figure 5.11 (a) Calculated reciprocity breaking curves of the CW and CCW output power in an integrated S-crossover ring laser as the S current increases and the ring currents are constant. (b) Measured reciprocity breaking curves in an S-crossover hybrid semiconductor ring laser.

CW lasing increases from 0.045 W/A to 0.11 W/A, and that of CCW lasing is conversely suppressed from 0.049 W/A to spontaneous emission level. These curves indicate that when the transmission through the S-crossover segment goes to zero, this laser reduces to a bi-directional ring laser. However, when the S current goes to zero, the differential quantum efficiency of CW and CCW lasing is not completely degenerate because of the slight difference in coupling of the 90/10 coupler between the CW and CCW direction. Both spectra of CW and CCW lasing are centered at 1572 nm, in the inset of Fig. 5.10(b) and Fig. 5.10(d). These spectra have a single frequency just above threshold, and become multimoded as the ring current increases. The excess fluctuation in the L-I curves for the CW direction in Fig. Fig. 5.10(b) exists, because the gain in the S-crossover is not clamped and there is also the interference between different modes.

The threshold current and the emission wavelength are predicted according to current contours in Fig. 5.9, for the given loss of 12.3 dB. These predicted values of the threshold current 73 mA and the emission wavelength 1568 nm are well matched with experiment values of 71 mA and 1572 nm. The decrease of the threshold current and the increase of the differential quantum efficiency in *CW* lasing are due to the gain through the SOA in the S segment.

Fig. 5.11(b) shows the measured unidirectionality of lasing due to reciprocity breaking as the *S* current increases and the ring current is constant. Since the laser resonator is composed

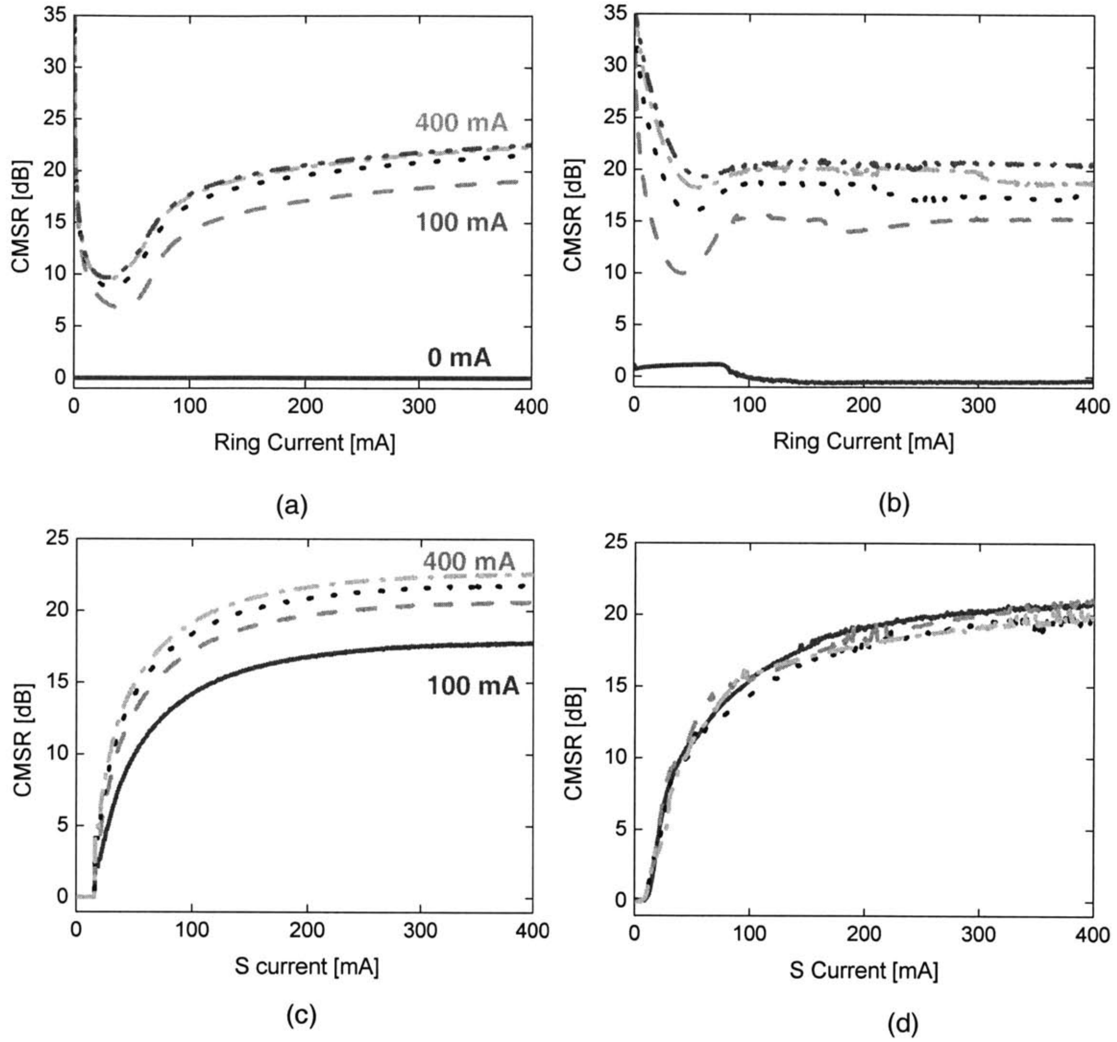

Figure 5.12 Calculated reciprocity breaking curves in an integrated S-crossover ring laser; (a) as the S currents are constant and the ring current increases (c) as the S current is fixed and the ring currents increase. Measured reciprocity breaking curves in an S-crossover hybrid semiconductor ring laser; (b) as the S currents are constant and the ring current increases (d) as the S current is fixed and the ring currents increase.

of optical fibers, the careful tuning of birefringence in these fibers should be performed with polarization controllers. Otherwise, kinks are observed due to polarization-dependent gain fluctuation of around 1 dB in the SOA and polarization-dependent loss in the output couplers.

Fig. 5.12(b) and Fig. 5.12(d) show *CMSR* measurements with constant currents to the ring and with constant currents to the S segment, respectively. Below the lasing threshold, a larger *CMSR* is observed than over the threshold in Fig. 5.12(b). This phenomenon agrees with the theoretical prediction of the preferential coupling of spontaneous emission to the CW direction in Fig. 5.12(a). As larger currents drive the SOA in the S segment, larger *CMSR* is observed due to the increase of spontaneous emission floor. The *CMSR* is distinctively saturated after the currents to the S segment of 200 mA in Fig. 5.12(d). The *CMSR* is steady or slightly decreasing as the ring current increases. For the same reason as the fluctuations in the L-I curves, bumps in different *CMSR* curves are explained by gain fluctuation and birefringence-dependent phase mismatch between the *S* segment and the ring.

I obtain a maximum *CMSR* of 35 dB below threshold and 21.5 dB above threshold and a maximum power of 31 mW from the CW direction. The *CMSR* is mainly limited by the remanant output power of the CCW direction even if the output power in CCW lasing is suppressed to spontaneous emission level. According to the numerical simulation with Eq. (5.9), the *CMSR* can be further increased by employing a higher-output coupler at the junction of the S segment and the output coupler. In this case, the output power and threshold current tends to increase in addition to the increased *CMSR*.

5.3.3 Retro-reflected Hybrid Ring Lasers

Theoretical Predictions

The macroscopic version of a unidirectional retro-reflected hybrid ring laser with a retro-reflector is shown in Fig. 5.8. The axial confinement factor in Eq. (5.6) and Eq. (5.7) for this laser is determined by the length of the ring that is 12 m long. L-I curves for the CW and the CCW outputs and the retro-outputs are almost the same as the S-crossover ring lasers except that the reciprocity breaking S current is replaced with retro-reflectivity. As the reflectivity of the retro-reflector R_b increases from 0% to 100% when the ring current I_R is constant, the threshold current of CW lasing decreases from 49 mA to 44 mA. Likewise, the retro-output power increases but the CCW power significantly suppressed, as shown in Fig. 5.13(a), Fig. 5.13(c), and Fig. 5.13(f). Fig. 5.14a shows theoretical calculations of reciprocity breaking as the retro-reflectivity increases and the ring current is constant. When the retro-reflectivity goes to zero, the CW and CCW output powers are degenerate. Then two directional powers start to bifurcate as the retro-reflectivity increases.

Fig. 5.15(a) and Fig. 5.15(c) show *CMSR* calculations with constant retro-reflectivity and the constant ring current, respectively. Like the S-crossover ring laser, the *CMSR* is distinc-

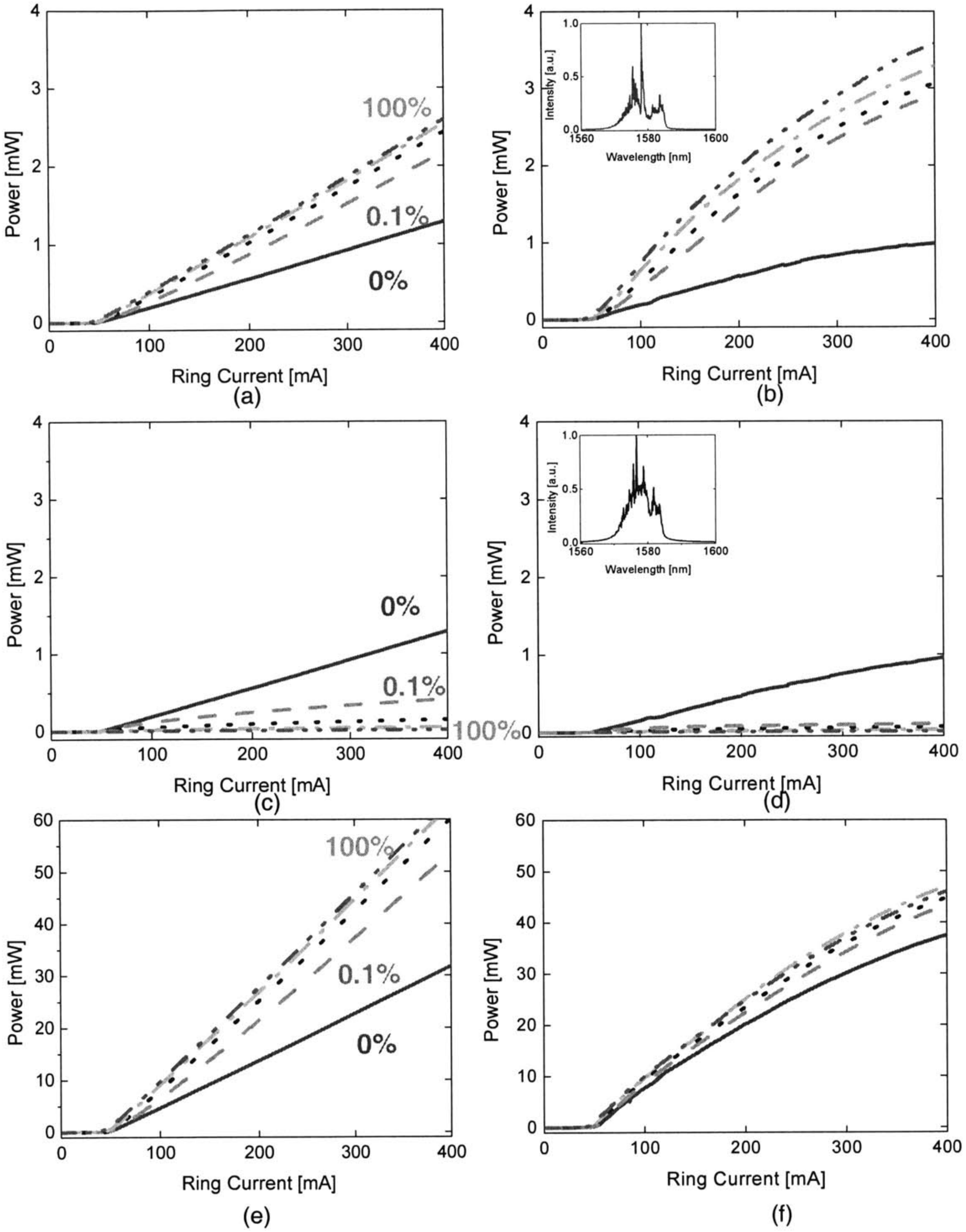

Figure 5.13 Calculated L-I curves in an integrated retro-reflected ring laser as the retro-reflectivity is constant and the ring current increases; (a) CW direction (c) CCW direction (e) retro-reflection output. Measured L-I curves in a retro-reflected hybrid semiconductor ring laser; (b) CW direction (d) CCW direction (f) retro-output; 100% (solid); 10% (dash); 1% (dot); 0.1% (dash-dot); 0% (dash-dot-dot).

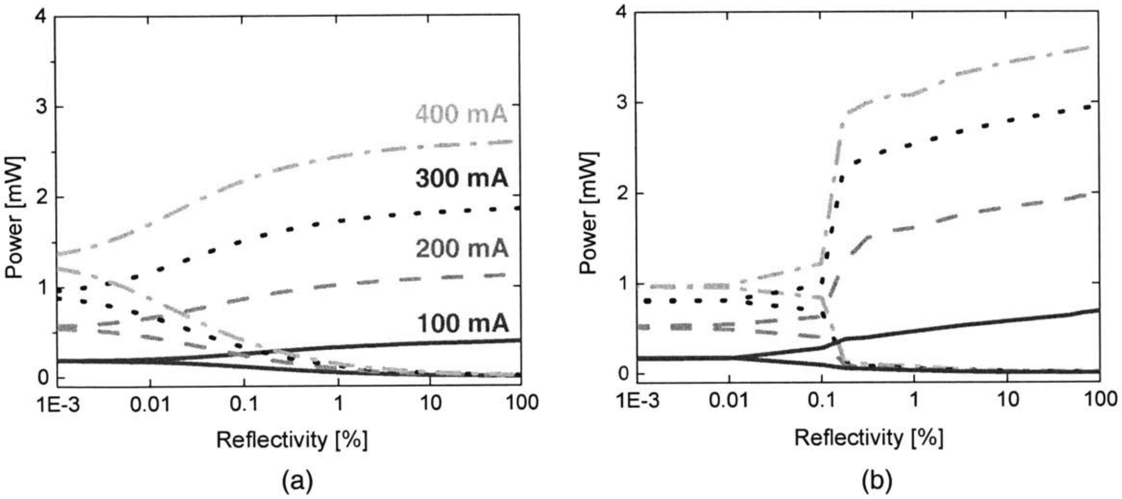

Figure 5.14 (a) Calculated reciprocity breaking curves in an integrated retro-reflected ring laser as the retro-reflectivity increases and the ring currents are constant. (b) Measured reciprocity breaking curves in a retro-reflected hybrid semiconductor ring laser.

tively saturated after the currents to the ring of 100 mA, as shown in Fig. 5.15(a). In the semi-log scale, gradual changes of the *CMSR* shown in Fig. 5.15(c) are predicted as the retro-reflectivity increases, and a maximal *CMSR* of 22.2 dB is predicted.

Experimental Results

In the macroscopic version of a retro-reflected hybrid ring laser, a fiber pigtailed Bragg grating can serve as a retro-reflector in addition to being a frequency filter. Here, a precision variable back-reflector (JDS Uniphase VB8B) is used to demonstrate unidirectionality of this laser. The retro-reflecting arm is 2 m long, and it feeds part of the losses to the ring resonator from the CCW direction into the CW direction. Isolators block all feedbacks at the outputs. A 95/5 coupler is used to maximize the coupling of a CCW beam into a CW beam at the retro-reflector arm, and a 10/90 coupler is used to minimize the effect of intracavity power tapping at the CW/CCW output-coupling arm. Two SOAs are used to provide two balanced output beams to the CW and CCW directions.

The L-I curves for CW and CCW beams in the retro-reflected ring laser are measured with the constant retro-reflectivity in Fig. 5.13(b) and Fig. 5.13(d), respectively. As the retro-reflectivity increases from 0% to 100%, the threshold currents of CW lasing decrease from 49

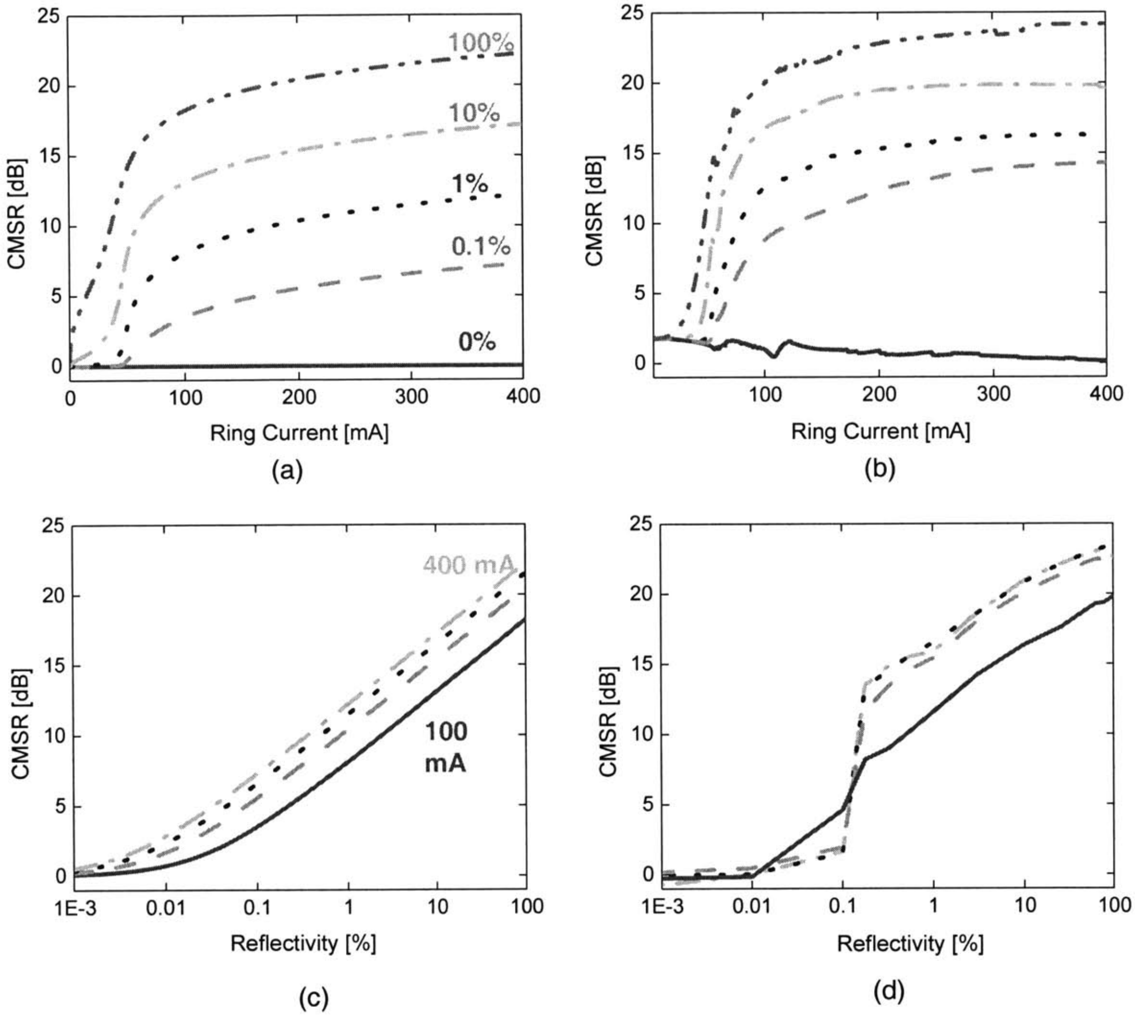

Figure 5.15 Calculated reciprocity breaking curves in an integrated retro-reflected ring laser; (a) as the retro-reflectivity is constant and the ring current increases (c) as the retro-reflectivity increases and the ring currents are constant. Measured reciprocity breaking curves in a retro-reflected hybrid semiconductor ring laser; (b) as the retro-reflectivity is constant and the ring current increases (d) as the retro-reflectivity increases and the ring currents are constant.

mA to 44 mA. Similar to the S-crossover laser, when the retro-reflectivity goes to zero, this laser reduces to a simple bi-directional ring laser with counter propagating modes of equal power. Both spectra of CW and CCW lasing are centered at 1577 nm, in the inset of Fig. Fig. 5.13(b) and Fig. 5.13(d). As the ring current increases, these spectra become multimode from a single frequency just above the threshold current. The threshold current of 50 mA and the emission wavelength of 1580 nm can be predicted, according to current contours in Fig. 5.9, the given loss of 13.8 dB, two SOAs in series, and zero retro-reflectivity. These calculated values are well matched with the experimental results of 49 mA and 1577 nm.

The L-I curves for retro-reflected output beams are measured with the constant retro-reflectivity in Fig. 5.13(f). The threshold currents of retro-outputs are the same as that of CW lasing. As the retro-reflectivity increases from zero to 100%, the differential quantum efficiency of CW lasing including the CW arm and the retro-reflector arm increases from 0.15 W/A to 0.18 W/A. In this case, the maximum power increases 38.5 mW and 50 mW, respectively. This low measured power of 50 mW, compared to the calculated power of 63 mW is mainly caused by the gain saturation due to the heating effect or carrier leakage with the large bias current to the SOA.

Fig. 5.14(b) shows the measured unidirectionality of lasing due to reciprocity breaking as the retro-reflectivity increases. In this semi-log figure, dramatic changes of output powers are observed around the retro-reflectivity between 0.1% and 0.2%. One explanation for this dramatic shift in the CCW power is that injection locking between reflected CCW and CW requires sufficiently large coupling of CCW into CW. Only after injection locking, the rate equation model assures the steady coupling from CCW to CW for unidirectionality.

Fig. 5.15(b) and Fig. 5.15(d) show *CMSR* measurements with constant retro-reflectivity and constant ring currents, respectively. Like the S-crossover ring laser, the *CMSR* is saturated after the currents to the ring of 150 mA in Fig. 5.15(b). In this retro-reflected ring laser, I obtained a maximum *CMSR* of 24.5 dB. According to Eq. (5.13), the *CMSR* can be further increased by employing a higher-output coupler at the junction of the retro-reflector and the ring.

5.4 Conclusion

The laser performance of unidirectional operation can be compared with that of bi-directional operation from L-I curve measurements. For S-crossover lasers, the threshold current decreases and the differential quantum efficiency increases, from 71 mA and 0.045 W/A for bi-directional operation to 45 mA and 0.11 W/A for unidirectional operation, according to Fig. 5.7(b). Also, the measured unidirectional power enhances approximately three times relative to the bi-directional ($I_S = 0$) power due to coupled photons to the preferred direction and their subsequent amplification in the S-segment, as shown in Fig. 5.8(a) and Fig. 5.8(b). For retro-reflected ring lasers, the threshold current decreases and the differential quantum efficiency increases, from 49 mA and 0.15 W/A for bi-directional operation to 44 mA and 0.18 W/A for unidirectional operation, according to Fig. 5.10(b). Also, the measured unidirectional power enhances approximately 30% relative to bi-directional (R_b = 0) power due to retro-reflected coupling beams, as shown in Fig. 5.1(a) and Fig. 5.1(b). This power enhancement is saturated because of gain saturation in the SOA.

For two types of unidirectional ring lasers, I compare the measured performances between them in regard to the output power, the threshold current, the *CMSR*, and stability. S-crossover ring lasers experimentally generate the maximal power of 30 mW, the threshold current of 45 mA, and the *CMSR* of 21.5 dB, as shown in Fig. 5.7(b) and Fig. 5.9(b). Retro-reflected ring lasers experimentally generate the maximal power of 45 mW, the threshold current of 44 mA, and the *CMSR* of 24.5 dB, as shown in Fig. 5.13(f) and Fig. 5.13(b). As a result, it is found both theoretically and experimentally that retro-reflected ring lasers generate higher output powers and the *CMSR* with the same 90/10 coupler, while maintaining almost the same threshold current as S-crossover lasers. S-crossover lasers produce more fluctuation as the bias current increases, because amplified spontaneous emission fluctuation in *S*-segment is added to the laser as shown in Fig. 5.9(b). Thus, retro-reflected ring lasers are more stable, assuming the same level of fiber-birefringence induced fluctuation of the output power. It is interesting to note that 30% of retro-reflectivity is strong enough to reach more than 20 dB of the *CMSR*. In addition, since it is unnecessary to provide amplification as in the electrically separate S-crossover waveguide, the integrated retro-reflecting arm can be easily fabricated with the same electrical contact as the ring in the processing.

Unidirectional operation in ring lasers improves the output power rather than two outputs of bi-directional operation and increases the side-mode suppression ratio due to the fact that traveling wave propagation along the ring eliminates spatial hole burning. For macroscopic systems such as gas, dye, and solid state Ti:Sapphire ring lasers, unidirectional operation has been widely performed using retro-reflecting mirrors in an external cavity as a simple and cost effective method. Unidirectional operation without using a Faraday isolator in Ti:Sapphire lasers has a great advantage to generate ultrafast mode-locked pulses where material dispersion of the isolating medium significantly obstructs sub-10-fs pulse generation [123]. Also, ring lasers facilitate the operation of high repetition rates at GHz ranges because the resonator round trip time is the half of the FPL in a given resonator length [125].

As a conclusion, I suggest two different approaches for unidirectional operation of integrated semiconductor ring lasers that are potentially useful for large-scale photonic integrated circuits. Since monolithically integrable isolators are not available in microphotonic integrated circuits, isolator-free S-crossover or retro-reflected semiconductor ring lasers are useful for unidirectional operation. For S-crossover ring lasers, a careful design is conducted with the finite-difference time-domain simulation to provide a single transverse mode at 2 μm width of the waveguide. An S-crossover waveguide of asymmetric Y-branch in these lasers is the key element to breaking the reciprocity of the ring. For retro-reflected ring lasers, a distributed Bragg grating as a retro-reflector as well as a frequency tuner or an etched facet can be incorporated into the ring to provide unidirectionality of lasing. Resonance properties of these ring lasers are derived from the transmitted and reflected electric fields based on the scattering matrix formalism. For these unidirectional ring lasers, I develop coupled rate equations to unravel the detailed light coupling for unidirectional operation. The macroscopic prototype lasers for unidirectional operation without using isolators are developed to demonstrate unidirectionality with semiconductor optical amplifiers and single mode optical fibers. In macroscopic hybrid ring prototype lasers, a Y-branch is replaced with an evanescent coupler, and a distributed Bragg grating is replaced with a fiber pigtailed retro-reflector. Macroscopic S-crossover and retro-reflected lasers result in up to 21.5 dB and 24.5 dB of counter-mode suppression ratio, respectively, which is in good agreement with theoretical predictions.

Chapter 6

Conclusions

First, I focused on developing a novel laser resonator that can generate high intensity pulses to fabricate passive photonic devices using nonlinear material processing. Mode-locked operation of a Ti:Sapphire laser was demonstrated at repetition rates of 15 to 4 MHz using a novel multiple pass cavity as an optical delay line. For 15 MHz lasers, I obtained 11.3 nJ pulse energy at 4.8 W pump power and 16.5 fs pulse duration centered at 806 nm with the bandwidth 42 nm. So, the peak power of the pulses is approximately 0.7 MW out of a 10 m long cavity. For 7 MHz lasers with a saturable Bragg reflector, I obtained 21 nJ total energy from two output couplings at 6.5 W pump power and 23.5 fs pulse duration centered at 821 nm with the bandwidth of 31 nm. Thus, the peak power would be 0.9 MW from a 21 nm long cavity, if there were a single beam-out through the output coupler instead two outputs. For 4 MHz lasers, I obtained 55 fs pulses with 48 nJ pulse energy when operating in the net negative dispersion regime and 80 fs pulses with 100 nJ pulse energy when operating in the net positive dispersion regime. Consequently, the peak power is as high as 1.25 MW from a 37 m long cavity.

This unprecedented low repetition rate of femtosecond laser suggests new approaches for achieving several MHz repetition rates and MW level peak powers. The low repetition rate laser is a cost effective approach for generating high pulse energies useful for laser-induced micromachining and nonlinear phenomenon studies. Additionally, the reduction in pulse repetition rates for a given pulse peak intensity should make it possible to study ultrafast nonlinear phenomena more easily by reducing parasitic thermal and excitation effects. To analyze the higher order effect of pulse shaping, such as saturable absorption and self-phase modulation, I analytically solved a quintic complex nonlinear Schrödinger equation with different pulse parameters. In these high intensity pulses, I showed that the modified-Sech is better fit to autocorrelation measurements than conventional Sech or Gaussian fits.

Second, passive photonic devices were fabricated by use of this novel high intensity laser resonator. Nonlinear processes of microexplosion mainly due to avalanche ionization and multiphoton absorption of intense ultrashort laser beams play the key role in generating index changes inside glass material. A theoretical model was set up to explain laser induced material decomposition and microexplosion. I demonstrated single mode/multi-mode passive device fabrication directly using high intensity laser pulses from this novel, low repetition rate Ti:Sapphire laser resonator, without using any active devices or amplifiers. Two dimensional devices were fabricated by linear scanning of femtosecond laser beams that are focused onto a glass using a microscopic objective. Passive photonic devices such as waveguides, gratings, and X and Y-couplers were fabricated, and most of their beam coupling was demonstrated. As a key component of switching devices like Mach-Zehnder interferometers and coupled mode devices is a very important device to control photon-flows. These X and Y couplers were fabricated by laterally branching focused beams, and their light coupling characteristics were analyzed. Three-dimensional structures of multiple-layer waveguides were fabricated, and their evanescent beam coupling was shown. Modal analysis showed that the index change after the laser-induced microexplosion was approximately 4×10^{-4}, which is consistent with other groups' measurements. This micromachining on transparent glass is a very promising technology for rapid direct writing and development of 3D photonic devices, possibly yielding significantly higher density integration than conventional planar devices.

Third, active photonic devices on InGaAsP/InGaAsP multiple quantum well p-i-n structures were fabricated using a high power Q-switched Nd:YAG laser. A theoretical model was developed to explain the threshold behavior of bandgap blue-shifts. The threshold fluence for melting of $In_{0.53}Ga_{0.47}As$ at 1.064 μm excitation was theoretically calculated to be 260 mJ/cm^2, which is close to the threshold fluence for bandgap shift of 230 mJ/cm^2 for the bandgap shift as reported in [80]. Likewise, the threshold fluence of melting at 532 nm was theoretically calculated to be 81 mJ/cm^2, which is close to the threshold fluence for bandgap shift of 65 mJ/cm^2 according to the measurement. Hence, based on the experiments, significant defects might be generated, and significant bandgaps were thus shifted at around the fluence of melting on the substrate excited either by 1.064 µm or by 532 nm. The longer interaction length at 1.064 µm excitation caused the higher threshold for both melting and bandgap shifts than 532 nm excitation. From the pulsed laser absorption induced disordering with 6000 pulses, I obtained the maximal bandgap shifts of 32 nm with the fluence of 65 mJ/cm^2 at 1.064 µm excitation and 45 nm with the fluence of 125 mJ/cm^2 at 532 nm excitation, respectively.

The surface was damaged by laser induced-decomposition of InGaAs capping layer, and the surface morphology, after the wet-etching of InGaAs/InP capping layers, was recovered as good as as-grown samples. However, ripples were observed at the surface irradiated above 125 mJ/cm^2, after the wet-etching. To take advantage of the separate source of defects away from QWs, the InP capping layer needed to be grown thicker than 2 µm. Then the disordered region both by laser irradiation and defect generation were etched away to regrow the perfect crystalline capping layer later on.

Last, I suggested two different approaches for unidirectional operation of integrated semiconductor ring lasers that were potentially useful for large-scale photonic integrated circuits. Since monolithically integrable isolators are not available in microphotonic integrated circuits, isolator-free S-crossover or retro-reflected semiconductor ring lasers are useful for unidirectional operation. For S-crossover ring lasers, a careful design was conducted with the finite-difference time-domain simulation to provide a single transverse mode of the waveguide. An S-crossover waveguide of asymmetric Y-branch in these lasers was the key element to breaking the reciprocity of the ring. For retro-reflected ring lasers, a distributed Bragg grating as a retro-reflector as well as a frequency tuner or an etched facet could be incorporated into the ring to provide unidirectionality of lasing. Resonance properties of these ring lasers were derived from the transmitted and reflected electric fields based on the scattering matrix formalism. For these unidirectional ring lasers, I developed a coupled rate equation model to unravel the detailed light coupling for unidirectional operation. The macroscopic prototype lasers for unidirectional operation without using isolators were developed to demonstrate unidirectionality with semiconductor optical amplifiers and single mode optical fibers.

In macroscopic hybrid ring prototype lasers, the laser performance of unidirectional operation was compared with that of bi-directional operation from L-I curve measurements. In macroscopic S-crossover lasers, Y-branch was replaced with an evanescent coupler, and a distributed Bragg grating was replaced with a fiber pigtailed retro-reflector. For S-crossover lasers, the threshold current decreased and the differential quantum efficiency increased, from 71 mA and 0.045 W/A for bi-directional operation to 45 mA and 0.11 W/A for unidirectional operation. This power enhancement was saturated because of gain saturation in the SOA. For retro-reflected ring lasers, the threshold current decreased and the differential quantum efficiency increased, from 49 mA and 0.15 W/A for bi-directional operation to 44 mA and 0.18 W/A for unidirectional operation. Macroscopic S-crossover and retro-reflected lasers resulted in up to 21.5 dB and 24.5 dB of counter-mode suppression ratio, respectively, which was in good agreement with theoretical predictions. As a result, it was found both theoretically and experimentally that retro-reflected ring lasers generated higher output powers and the CMSR with the same 90/10 coupler, while maintaining almost the same threshold current as S-crossover lasers.

S-crossover lasers produced more fluctuation as the bias current increased, because amplified spontaneous emission fluctuation in S-segment was added to the laser. Thus, retro-reflected ring lasers were more stable, assuming the same level of fiber-birefringence induced fluctuation of the output power. It is interesting to note that 30% of retro-reflectivity is strong enough to reach more than 20 dB of the CMSR. Unidirectional operation in ring lasers improved the output power rather than two outputs of bi-directional operation and increased the side-mode suppression ratio due to the fact that traveling wave propagation along the ring eliminated spatial hole burning. Also, ring lasers could facilitate the mode-locked operation of high repetition rates at GHz ranges because the resonator round trip time is the half of the FPL in a given resonator length.

In further studies I will investigate the possibility of extending MPC laser designs to operate with repetition rates of ~ 1 MHz. In this case, higher peak pulse intensities are expected and the laser cavity has to operate with a reduced saturable absorption nonlinearity against multiple pulsing instability. These high pulse energies can facilitate to fabricate active optical devices of waveguide lasers and amplifiers on active glasses of, e.g. Er:glass and Nd:glass as well as laser crystals. Eventually, it would be possible that 3D photonic circuits include all different passive and active components of tunable filters, waveguides, laser transmitters and amplifiers using the novel high intensity laser resonator.

In addition, it is important to have the passive waveguide of output couplers and retro-reflectors in semiconductor ring lasers. To this end, quantum well intermixing can be employed to change the bandgap of these waveguide sections, making them low-loss passive waveguides.

Appendix A

Appendix: Chapter 2

A.1 Quintic Complex Master Equation for Nonlinear Solitary Pulses

From the solution of Eq. (2.19), various parameters are derived. The pulse energy W is derived by integrating $a(\mathrm{T,t})a(\mathrm{T,t})^*$ as.

$$W = \frac{2A^2\tau Tan^{-1}\left(\sqrt{\frac{1-B}{1+B}}\right)}{\sqrt{1-B^2}} \tag{A.1}$$

When Eq. (2.19) is plugged into Eq. (2.12), the complex master equation reduces to three complex equations involving three multipliers of $(\cosh(t/\tau_p)+B)^{-(1+j\beta)/2}$. From setting them to zero, I obtain the following parameters. The chirp parameter β is calculated by

$$\beta = \frac{3g\delta - 3D\delta\Omega^2 - \sqrt{8(g\delta + D\gamma\Omega^2)^2 + (3g\delta - 3D\delta\Omega^2)^2}}{2(g\delta + D\gamma\Omega^2)} \tag{A.2}$$

The pulse width τ is

$$\left(\tau = 6B(g^2 + D^2\Omega^4)\left(-3g\gamma + 3D\delta\Omega^2 + \sqrt{8(g\delta + D\gamma\Omega^2)^2 + (3g\delta - 3D\delta\Omega^2)^2}\right)\right)$$

$$\cdot\frac{Tan^{-1}\left(\sqrt{\frac{1-B}{1+B}}\right)}{W(g\delta\Omega + D\gamma\Omega^3)^2\sqrt{1-B}} \tag{A.3}$$

The phase of the pulse is

$$\Psi = \frac{2g\beta - D(\beta^2 - 1)\Omega^2}{\tau^2\Omega^2} \tag{A.4}$$

The constant B is calculated with given energy W by

$$B = \cos\left(\frac{1}{2}W\Omega\sqrt{\frac{D\mu\Omega^2 - g\nu}{\beta(g^2 + D^2\Omega^4)}}\right) \tag{A.5}$$

Appendix B

Appendix: Chapter 5

B.1 Scattering Matrix for Asymmetric Y-Branch

The S matrix is a useful means to represent the relationship between the incident, reflected, and transmitted wave amplitudes at a waveguide junction. For lossless networks, in particular, simple relations between the different scattering coefficients can be found by using the condition for conservation of energy.

For a given polarization, the amplitudes of the incident and reflected waves at the input and output planes constitute a full description of the action of the system - a total of four wave amplitudes [126]. The amplitudes of incident and reflected waves are denoted by *a* and *b*, respectively. If there are n-ports at the junction, then the relationship is described by the matrix Eq. (B.1). When a junction carries more than one mode, each mode is treated as a separate port by virtue of the orthogonality of waveguide modes. Orthogonality does not allow the individual modes to couple along the waveguide, but they can interact at the junction.

$$b_i = \sum_{k=1}^{n} S_{ij} a_j \tag{B.1}$$

In order to enforce the unidirectional operation of semiconductor ring lasers, an S-crossover waveguide is incorporated into the ring to break the reciprocity between the clockwise (CW) and the counter-clockwise (CCW) propagation (Fig. B.1a). For the coupling from the ring to the crossover or to the output waveguide, asymmetric Y-branches or forks are introduced and their S matrix components are obtained with finite-difference time-domain (FDTD) simulation (Fig. B.2). The width of a single transverse mode waveguide is determined to be 2 (m from the effective core index of 3.5 and the effective background index of 3.3 at 1.55 μm in which InGaAsP constitutes a quantum well, and InP/polyimide is a guiding ridge.

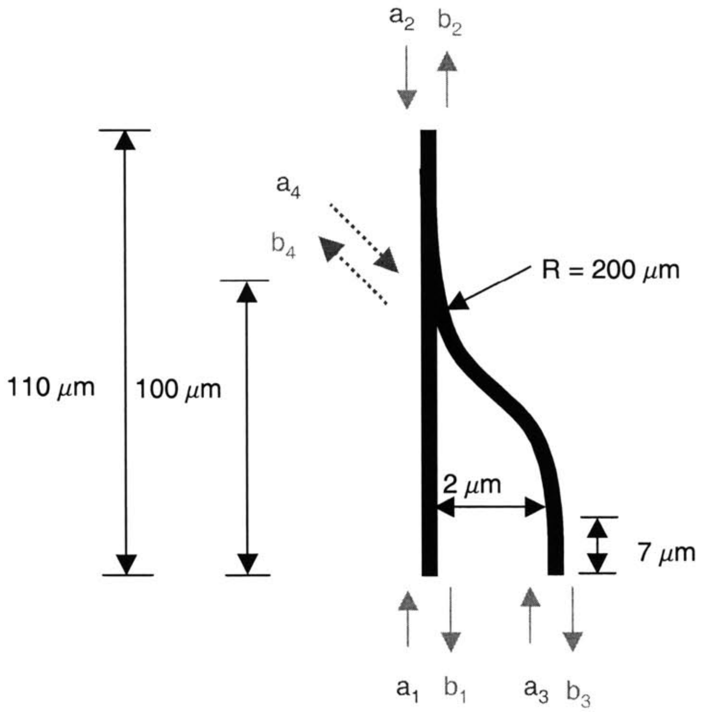

Figure B.1 Asymmetric Y-branch or fork; width of 2 μm, index of core of 3.5, and index of background of 3.3.

Two kinds of radiation losses are associated with the junction. One of these losses is the interferometric radiation loss that is related to the phase difference of the light waves at the Y-junction [127]. The other loss is the fractional coupling loss that depends on the branching angle of the asymmetric Y-junction from the straight waveguide [128]. A hypothetical fourth port is introduced to take into account the interferometric radiation loss in the vicinity of the junction, and a fractional coupling loss factor α is introduced. Without loss, the reflection r and the phase offset θ describe the whole operation, where $t = \sqrt{1-r^2}$ in Eq. (B.2).

I obtain each component of the S matrix from the amplitude of the transverse electric field at the asymmetric Y-junction based on well-known FDTD simulation with FullWAVE (Rsoft) as shown in Fig. B.2. The FDTD technique is based on numerical integration in time of Max-

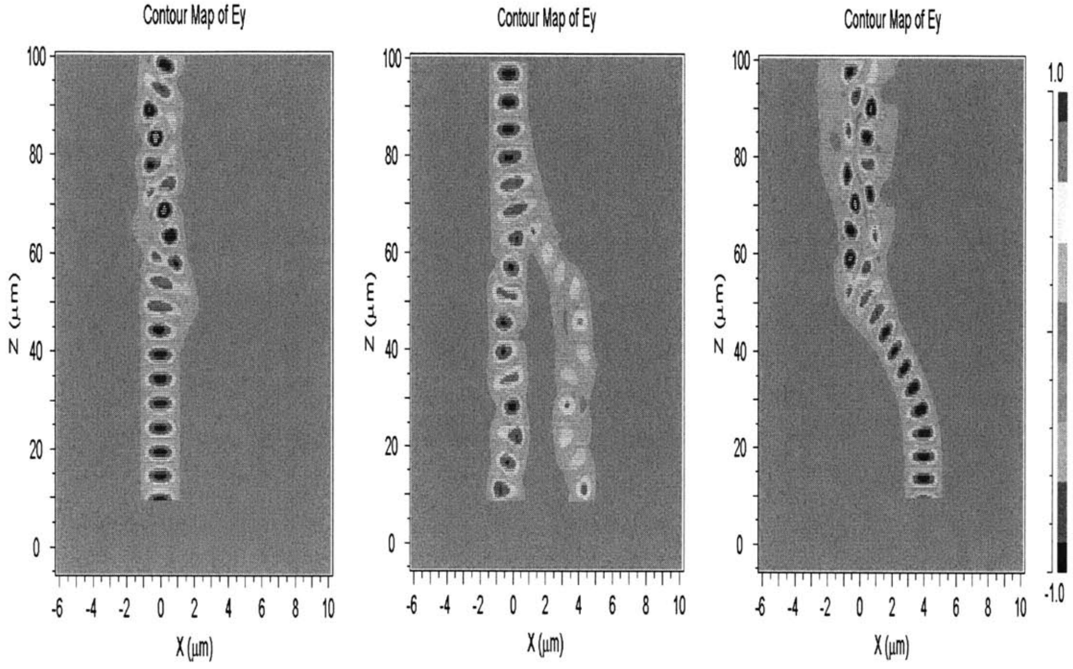

Port 1 Port 2 Port 3

Figure B.2 Contour map of transverse electric field launched from each port; (a) $a_1 = 1$ (b) $a_2 = 1$ (c) $a_3 = 1$.

well's equations using Yee meshes. FullWAVE is a simulation package that employs perfectly matched boundary conditions for absorbing electromagnetic waves incident on the edges of the computation domain in space. Table B.1 shows the major parameter values of FullWAVE including the refractive index distribution and the electromagnetic field excitation of the continuous wave.

In this case, the coupling between adjacent ports and reflected waves is zero within the computational error.

$$\begin{bmatrix} b_1 \\ b_2 \\ b_3 \\ b_4 \end{bmatrix} = \sqrt{1-\alpha}\begin{bmatrix} 0 & jte^{j\vartheta} & 0 & -r \\ jte^{j\vartheta} & 0 & -r & 0 \\ 0 & -r & 0 & jte^{-j\vartheta} \\ -r & 0 & jte^{-j\vartheta} & 0 \end{bmatrix}\begin{bmatrix} a_1 \\ a_2 \\ a_3 \\ a_4 \end{bmatrix} \tag{B.2}$$

TABLE B.1 Major parameter values of FullWAVE simulation; PML, perfectly matched layer.

Parameter	Value	Unit
Attenuation constant	0	μm^{-1}
Domain maximum along z direction	100	μm
Domain minimum along z direction	-5	μm
Index of background	3.3	
Index difference in core and background	0.2	
Launched wavelength	1.55	μm
PML width along x direction	0.3	μm
PML width along z direction	0.3	μm
PML reflectivity	10^{-8}	
Position of source	14.7	μm
Size of step in time	0.005	sec
Size of grid	0.03	μm
Size of step in space	0.03	μm
Type of excitation	CW	
Type of index profile	PROF_STEPINDEX	
Width of waveguide	2	μm

The S matrix is symmetric, which holds for the linear reciprocal system of any isotropic material in the Y-branch. With a cosine-shaped S-bend in the Y-branch, the transmittance between port 1 and port 2 is 0.6, and transmittance between port 2 and port 3 is 0.2. Thus, the fractional coupling loss factor, α in Eq. (B.2), is 0.2; it is zero in the lossless S matrix. The S matrix of the four ports at the asymmetric Y-branch is obtained in Eq. (B.3).

$$S = \sqrt{0.8}\begin{bmatrix} 0 & j\sqrt{0.25}e^{j\vartheta} & 0 & -\sqrt{0.75} \\ j\sqrt{0.25}e^{j\vartheta} & 0 & -\sqrt{0.75} & 0 \\ 0 & -\sqrt{0.75} & 0 & j\sqrt{0.25}e^{-j\vartheta} \\ -\sqrt{0.75} & 0 & j\sqrt{0.25}e^{-j\vartheta} & 0 \end{bmatrix}$$

As a result, the S matrix represents a lossy network of the Y-branch because the power is not conserved in Eq. (B.3).

$$SS^{\dagger} = \kappa\tilde{I} = 0.8\tilde{I} < \tilde{I} \tag{B.3}$$

where κ is 1-α.

Appendix C

Appendix: Chapter 5

C.1 Derivation of Resonance Filter Properties using Diagrammatic Approach

C.1.1 S-crossover ring resonator

A diagrammatic approach is introduced to represent the infinite sum of all possible paths from input field a to output field G in a reminiscence of the perturbation theory [129]. Each diagram and its physical meaning are enumerated in Table C.1. The first-order distinctive paths of *G1* and *G2* are topologically factorized and evaluated, where two diagrams are conceptually equal because there exists only the change of ordering between the S-crossover waveguide and the ring in Eq. (C.1) and (C.2). Likewise, the unit turn of M and N are equal because the direction of turns is opposite in Eq. (C.3) and (C.4). The higher order paths are simply the multiplication of the unit turn with M (CCW) or N (CW) before and after the first order paths of *G1* and *G2*. The infinite orders in Eq. (C.5) are then summed over to derive the overall reflection coefficient G in Eq (C.6). Thus, the overall reflectivity in Eq. (5.1) is represented by the ratio of the output power to the input power $|a|^2$ by taking the total phase offset, $\theta_1 + \theta_2 + \theta_3$, as in Eq. (C.7).

$G_1 =$

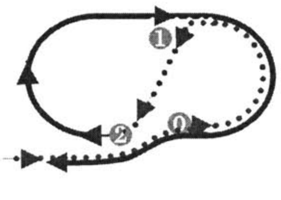

$$= \rightarrow \cdot {}_{o}\supset \cdot S^{1} \cdot \subset_{2} \cdot {}^{1}\supseteq \cdot \leftarrow_{o}$$

$$= [a]\,[(-r_o)e^{i\Phi_1}]\,[(-r_1)e^{i\Phi_S}]\,[(-r_2)e^{i\Phi_2}]\,[(jt_1\, e^{i\vartheta_1})e^{i\Phi_1}]\,[-r_o]$$

$$= a\,(j\, r_o{}^2 r_1 r_2 t_1 e^{i\vartheta_1})e^{i(2\Phi_1+\Phi_2+\Phi_S)} \tag{C.1}$$

TABLE C.1 Diagrams of different terms and corresponding features of an S-crossover resonator in Fig. 5.29(a).

Diagram	**Feature**
$\rightarrow$	Input a to the resonator
$\leftarrow_o$	Output after the bend transmission in the port O
${}_o\supset$	CCW Propagation along the waveguide L1 after the bend transmission in the port O
${}^1\supseteq$	CW propagation along the waveguide L1 after the straight transmission in the port 1
${}^1\supset$	CW propagation along the waveguide L1 after the bend transmission in the port 1
S^1	Downward propagation along the S-crossover Ls after the bend transmission in the port 1
$\subset^1$	CCW propagation along the waveguide L2 after the straight transmission in the port 1
$\subseteq_2$	CW propagation along the waveguide L2 after the straight transmission in the port 2
$\subset_2$	CW propagation along the waveguide L2 after the bend transmission in the port 2
$-_o$	CW propagation along the waveguide L3 after the straight transmission in the port O
${}_2-$	CCW propagation along the waveguide L3 after the straight transmission in the port 2

$G_2=$

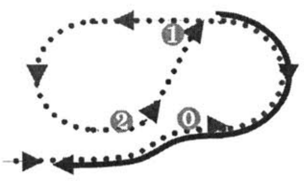

$$= \rightarrow \cdot {}_o\supset \cdot \subseteq_2 \cdot S^1 \cdot {}^1\supset \cdot \leftarrow_o$$
$$= [a]\,[(-r_o)e^{i\Phi_1}]\,[(jt_1\, e^{i\vartheta_1})e^{i\Phi_2}]\,[(-r_2)e^{i\Phi_S}]\,[(-r_1)e^{i\Phi_1}]\,[-r_o]$$
$$= G_1 \tag{C.2}$$

$M =$

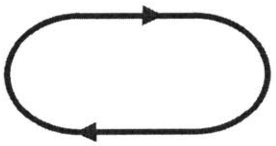

$$= -_o \times \subset_2 \times {}^1\supset$$
$$= [(jt_o\, e^{i\vartheta_o})e^{i\Phi_3}]\,[(jt_2\, e^{i\vartheta_2})e^{i\Phi_2}]\,[(jt_1\, e^{i\vartheta_1})e^{i\Phi_1}]$$
$$= (-j\, t_o t_1 t_2 e^{i(\vartheta_o+\vartheta_1+\vartheta_2)})e^{i(\Phi_1+\Phi_2+\Phi_3)} \tag{C.3}$$

$N =$

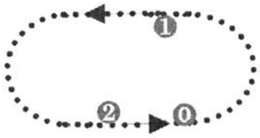

$$= {}_o\supset \times \subset^1 \times {}_2-$$

$$= [(jt_o\ e^{i\vartheta_o})e^{i\Phi_1}]\ [(jt_1\ e^{i\vartheta_1})e^{i\Phi_2}]\ [(jt_2\ e^{i\vartheta_2})e^{i\Phi_3}] = M \tag{C.4}$$

$$G = G_1 \sum_{m=0}^{\infty} M^m + G_2 \sum_{n=0}^{\infty} N^n = 2\ G_1 \sum_{m,n=0}^{\infty} M^m M^n = \frac{2\ G_1}{(1-M)^2} \tag{C.5}$$

$$= \frac{2j\ r_o{}^2 r_1 r_2 t_1 e^{i\vartheta_1} e^{i(2\Phi_1+\Phi_2+\Phi_S)}}{(1+j\ t_o t_1 t_2 e^{i(\vartheta_o+\vartheta_1+\vartheta_2)} e^{i\Phi_R})^2}\ a \tag{C.6}$$

$$Ref_S = \frac{G\ G^*}{a\ a^*} \tag{C.7}$$

C.1.2 Retro-reflected ring resonator

Each diagram and its physical meaning are enumerated in Table C.1. The first-order distinctive paths from *H1* to *H4* are topologically factorized, where two diagrams of *H2* to *H3* are conceptually equal because there exists only the change of ordering between the retro-reflector arm and the ring in Eq. (C.8) and (C.5). Similar to the S-crossover resonator, the unit turn of M and N are equal because the direction of turns is opposite in Eq. (C.12) and (C.13). The higher order paths are simply the multiplication of the unit turn with M (CCW) or N (CW) before and after the first order paths of *H1* through *H4*. The infinite orders are then summed over to derive the overall reflection coefficient *G* in Eq (C.15). Thus, the overall reflectivity in Eq. (2) is represented by the ratio of the output power to the input power |a|2 by taking the phase offset, θ_O, as θ in Eq. (A20).

$H_1 =$

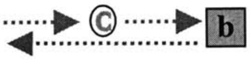

$$= \rightarrow \cdot {}_c\Rightarrow \cdot \Leftarrow_b \cdot \leftarrow_c$$

$$= [a]\ [(jt_c e^{-i\vartheta_c})e^{i\Phi_b}]\ [-r_b e^{i\Phi_b}]\ [(jt_c\ e^{-i\vartheta_c})]$$

$$= a\ (t_c{}^2 r_b e^{-i2\vartheta_c})e^{i2\Phi_b} \tag{C.8}$$

$H_2 =$

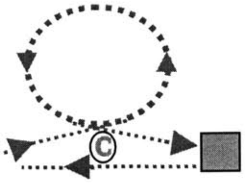

$$
\begin{aligned}
&= \rightarrow \cdot \underset{c}{O} \cdot {}_{c}{\rightarrow} \cdot \Leftarrow_b \cdot \leftarrow_c \\
&= [a]\,[(-r_c)e^{i\Phi_R}]\,[(-r_c)e^{i\Phi_b}]\,[-r_b e^{i\Phi_b}]\,[(jt_c\, e^{-i\vartheta_c})] \\
&= a\,(-j\, r_c{}^2 r_b t_c)e^{-i\vartheta_c} e^{i(\Phi_R+2\Phi_b)}
\end{aligned}
\tag{C.9}
$$

$H_3 =$

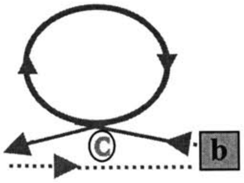

$$
\begin{aligned}
&= \rightarrow \cdot {}_{c}{\Rightarrow} \cdot \Leftarrow_b \cdot \underset{c}{O} \cdot \leftarrow_c \\
&= [a]\,[(jt_c\, e^{-i\vartheta_c})e^{i\Phi_b}]\,[-r_b e^{i\Phi_b}]\,[(-r_c)e^{i\Phi_R}]\,[-r_c] \\
&= H_2
\end{aligned}
\tag{C.10}
$$

$H_4 =$

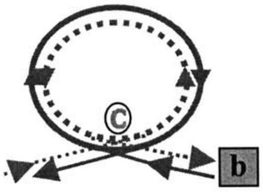

$$
\begin{aligned}
&= \rightarrow \cdot \underset{c}{O} \cdot {}_{c}{\rightarrow} \cdot \Leftarrow_c \cdot \underset{c}{O} \cdot \leftarrow_c \\
&= [a]\,[(-r_c)e^{i\Phi_R}]\,[(-r_c)e^{i\Phi_b}]\,[-r_b e^{i\Phi_b}]\,[(-r_c)e^{i\Phi_R}]\,[-r_c] \\
&= a\,(-r_c{}^4 r_b)e^{i(2\Phi_R+2\Phi_b)}
\end{aligned}
\tag{C.11}
$$

$M =$

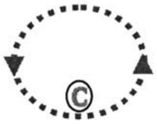

$$
\begin{aligned}
&= \underset{c}{O} \\
&= (jt_c\, e^{i\vartheta_c})e^{i\Phi_R}
\end{aligned}
\tag{C.12}
$$

$N =$

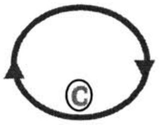

$$= \underset{c}{O} = M \tag{C.13}$$

$$
\begin{aligned}
H &= H_1 + 2H_2 \sum_{m=0}^{\infty} M^m + H_4 \sum_{m=0}^{\infty} M^n \sum_{n=0}^{\infty} N^n = H_1 + (2H_2 + H_4 \sum_{m=0}^{\infty} M^m) \sum_{m=0}^{\infty} M^m \\
&= H_1 + \frac{2H_2}{1-M} + \frac{H_4}{(1-M)^2}
\end{aligned}
\tag{C.14}
$$

$$= e^{i2\Phi_b} r_b [\frac{t_c e^{-i\vartheta_c} - j(r_c{}^2 + t_c{}^2)e^{i\Phi_R}}{1 - j\, t_c e^{i\vartheta_c} e^{i\Phi_R}}]^2\; a \tag{C.15}$$

$$Ref_R = \frac{H\ H^*}{a\ a^*} \tag{C.16}$$

Bibliography

[1] Dieter Bäuerle, *Laser processing and chemistry,* 3rd Ed., Springer-Verlag, New York, 2000.

[2] E. Dupont, X. Zhu, S. Chiu, S. Moisa, M. Buchanan, M. Gao, H. C. Liu, and P. B. Corkum, "*In Situ* repair of optoelectronic devices with femtosecond laser pulses," *Semicond. Sci. Technol.* **15**, L15-L18 (2000).

[3] E. Pennings, G-D Khoe, M. K. Smit, and T. Staring, "Integrated-optic versus microoptic devices for fiber-optic telecommunication systems: A comparison," *IEEE Sel. Top. Quantum. Electron.* **2**, 151-164 (1996).

[4] Stewart E. Miller, "Integrated Optics: An Introduction," *Bell Sys. Tech. J.* **48**, 2059 (1969).

[5] R. Kaiser and H. Heidrich, "Optoelectric/Photonic integrated circuits on InP between technological feasibility and commercial success," *IEICE Trans. Electron. E,* **85**, 970-981 (2002).

[6] G. P. Agrawal and N. K. Dutta, *Semiconductor Lasers.* New York: Van Nostrand Reinhold, 1993.

[7] B. E. Little and S. T. Chu, "Toward very large-scale integrated photonics," *Optics and Photonics News,* **24**, November (2000).

[8] Wayne H. Knox, "Ultrafast technology in telecommunications," *IEEE Sel. Top. Quan. Electron.* **6**, 1273-1278 (2000).

[9] Paras N. Prasad, Introduction to Biophotonics, John Wiley & Sons Inc., New Jersey, 2003.

[10] K. M. Davis, K. Miura, N. Sugimoto, and K. Hirao, "Writing waveguides in glass with a femtosecond laser," *Opt. Lett.* **21**, 1729-1731 (1996).

[11] D. Homoelle, S. Wieldandy, A. L. Gaeta, N. F. Borrelli, and C. Smith, "Infrared photosensitivity in silica glass exposed to femtosecond laser pulses," *Opt. Lett.* **24**, 1311-1314 (1999).

[12] C. B. Schaffer, N. Nishimura, and E. Mazur, "Microscopic bulk damage in dielectric materials using nanajoule femtosecond laser pulses," *Conference on Lasers and Electro-Optics*, 232 (1999).

[13] S. H. Cho, K. Minoshima, E. P. Ippen, and J. G. Fujimoto, "Waveguide device fabrication using nonlinear materials processing with a 4.2 MHz femtosecond Ti:Al_2O_3 Laser oscillator," in *Optical Society of America Annual Meeting*, Rhode Island, Oct 22-26, 2000.

[14] A. M. Streltsov and N. F. Borrelli, "Fabrication and analysis of a directional coupler written in glass by nanojoule femtosecond laser pulses," *Opt. Lett.* **26**, 42-45 (2001).

[15] L. Xu, G. Tempea, A. Poppe, M. Lenzner, C. Spielmann, F. Krausz, A. Stingl, and K. Ferencz, "High power sub-100-fs Ti:Sapphire oscillator," *App. Phys. B.* **65**, 175-188 (1997).

[16] M. S. Pshenichnikov, W. P. de Boeii, and D. A. Wiersma, "Generation of 13-fs, 5-MW pulses from a cavity dumped Ti:sapphire laser," *Opt. Lett.* **19**, 572-574 (1994).

[17] Phillpe Bado, "Micromachining: Ultrafast pulses create waveguides and microchannels," *Laser Focus World*, 73-75, April, 2000.

[18] T. L. Koch and U. Koren, "Semiconductor photonic integrated circuits," *IEEE J. Quantum. Electron*, **27**, 641-653 (1991).

[19] R. C. Alferness, U. Kore, L. L. Buhl, B. I. Miller, M. G. Young, T. L. Koch, G. Raybon, and C. A. Burrus, "Broadly tunable InGaAsP/InP laser based on vertical coupler filter with 57 nm tuning range," *Appl. Phys. Lett.* **60**, 3209-3211 (1992).

[20] John H. Marsh, "Quantum well intermixing," *Semicond. Sci. Technol.* **8**, 1136-1155 (1993).

[21] Nick Holonyak, Jr., "Impurity-induced layer disordering of quantum-well heterostructures: Discover and prospects," *IEEE Sel. Top. Quantum. Electron.* **4**, 584-594 (1998).

[22] D. G. Deppe and N. Holonyak, Jr., "Atom diffusion and impurity-induced layer disordering in quantum well III-V semiconductor heterostructures," *J. Appl. Phys.* **64**, R93-R113 (1988).

[23] A. C. Bryce, F. Camacho, P. Cusumano, and J. H. Marsh, "CW and mode-locked integrated extended cavity lasers fabricated using impurity free vacancy disordering," *IEEE Sel. Top. Quantum. Electron.* **3**, 885-892 (1997).

[24] S. K. Si, D. H. Yeo, K. H. Yoon, and S. J. Kim, "Area selectivity of InGaAsP-InP multiquantum-well intermixing by impurity-free vacancy diffusion," *IEEE Sel. Top. Quantum. Electron.* **4**, 619-623 (1998).

[25] S. Charbonneau, E. S. Koteles, P. J. Poole, J. J. He, G. C. Aers, J. Haysom, M. Buchanan, Y. Feng, A. Delage, F. Yang, M. Davies, R. D. Goldberg, P. G. Piva, and I. V. Mitchell, "Photonic integrated circuits fabricated using ion implantation," *IEEE Sel. Top. Quantum. Electron.* **4**, 772 (1998).

[26] J. P. Reithmaier and A. Forchel, "Focused ion-beam implantation induced thermal quantum-well intermixing for monolithic optoelectronic device integration," *IEEE Sel. Top. Quantum. Electron.* **4**, 595-605 (1998).

[27] E. J. Skogen, J. S. Barton, S. P. DenBaars, and L. A. Coldren, "Tunable sampled-grating DBR lasers using quantum well-intermixing, *IEEE Photon. Technol. Lett.* **14**, 1243-1245 (2002).

[28] C. J. McLean, J. H. Marsh, R. M. De La Rue, A. C. Bryce, and R. W. Glew, "Layer selective disordering by photoabsorption-induced thermal diffusion in InGaAs/InP based multiquantum well structure," *Electron. Lett.* **28**, 1117-1118 (1992).

[29] J. J. Dubowski, S. Charbonneau, A. P. Roth, P. J. Poole, C. Lacelle, and M. Buchanan, "A comparative study of laser- and ion implantation-induced quantum well intermixing in GaInAsP/InP microstructures," *SPIE* **2991**, 113 (1997).

[30] T. K. Ong, O. Gunawan, B. S. Ooi, Y. L. Lam, Y. C. Chan, Y. Zhou, A. S. Helmy, and J. H. Mash, "High-spatial-resolution quantum-well intermixing process in GaInAs/GaInAsP laser structure using pulsed-photoabsorption-induced disordering," *J. Appl. Phys.* **87**, 2775-2779 (2000).

[31] S. H. Cho and R. J. Ram, "Pulsed Light Absorption Induced Quantum Well Intermixing on InGaAsP/InGaAsP MQW using 532 nm Irradiation," submitted to *Conference on Lasers and Electro-Optics*, 2004.

[32] L. A. Coldren, S. W. Corzine, *Diode Lasers and Photonic Integrated Circuits*, in Wiley Series in Microwave and Optical Engineering, eds. Kai Chang. New York: John Wiley & Sons Inc. 1995.

[33] Ari Tervonen, "Challenges and opportunities for integrated optics in optical networks," in *Integrated Optics Devices III* (Proc. SPIE), 2-11 (2000).

[34] D. D. Lofgreen, R. L. Naone, and J. Ko, *Heterogeneous Optoelectronics Integration*, eds. Elias Towe. Washington: SPIE press, 2000.

[35] J. P. Hohimer, G. A. Vawter, and D. C. Craft, "Unidirectional operation in a semiconductor ring diode laser," *App. Phys. Lett.* **63**, 2457-2459 (1993).

[36] J. J. Liang, S. T. Lau, M. H. Leary, and J. M. Ballantyne, "Unidirectional operation of waveguide diode ring lasers," *App. Phys. Lett.* **70**, 1192-1194 (1997).

[37] W. Drexler, U. Morgner, C. Prtris, S. A. Boppart, F. X. Kartner, X. Li, S. H. Cho, E. P. Ippen, M. E. Brenzinski, and J. G. Fujimoto, " Subcellular optical coherence tomography with a kerr lens mode-locked Ti:Al_2O_3 laser," *International Symposium on Biomedical Optics*, San Jose, California, 1999.

[38] U. Morgner, F. X. Kärtner, S. H. Cho, Y. Chen, H. A. Haus, J. G. Fujimoto, E. P. Ippen, V. Scheuer, G. Angelow, and T. Tschudi, "Sub-two-cycle pulses from a Kerr-lens mode-locked Ti:sapphire laser," *Opt. Lett.* **24**, 411-413 (1999)

[39] D. H. Sutter, G. Steinmeyer, L. Gallmann, N. Matuschek, F. Morier-Genoud, U. Keller, V. Scheuer, G. Angelow, and T. Tschudi, "Semiconductor saturable-absorber mirror assisted Kerr-lens mode-locked Ti:Sapphire laser producing pulses in the two-cycle regime," *Opt. Lett.* **24**, 631-633 (1999).

[40] M. Nisoli, S. De Silvestri, O. Svelto, R. Szipocs, K. Ferencz, Ch. Spielmann, S. Sartania, and F. Krausz, "Compression of high-energy laser pulses below 5 fs," *Opt. Lett.* **22**, 522-524 (1997).

[41] A. Baltuska, Z. Wei, M. S. Pshenichnikov, D. A. Wiersma, and R. Szipocs, "All-solid-state cavity-dumped sub-5-fs laser," *Appl. Phys. B* **65**, 175-177 (1997).

[42] B. E. Bouma and J. G. Fujimoto, "Compact Kerr-lens mode-locked resonators," *Opt. Lett.* **21**, 134-136 (1996); B. E. Bouma, M. Ramaswamy-Paye, and J. G. Fujimoto, "Compact resonator designs for mode-locked solid-state lasers," *Appl. Phys. B* **65**, 213-215 (1997).

[43] M. Ramaswamy, M. Ulman, J. Paye, and J. G. Fujimoto, "Cavity-dumped femtosecond Kerr-lens mode-locked Ti:Al_2O_3 laser," *Opt. Lett.* **18**, 1822-1824 (1993)

[44] S. H. Cho, B. E. Bouma, E. P. Ippen, and J. G. Fujimoto, "A low repetition rate high peak power KLM Ti:Al_2O_3 laser using a multiple pass cavity," *Opt. Lett.* **24**, 417-419 (1999).

[45] M. Fe H. Tarroja, M. Sharafi, and L. W. Casperson, "Spontaneous mode locking in long-cavity Xenon lasers," *J. Opt. Soc. Am. B* **6**, 1564-1573 (1989).

[46] J. B. Deaton Jr., A. D. W. Mckie, J. B. Spicer, and J. W. Wagner, "Generation of narrow-band ultrasound with a long cavity mode-locked Nd:YAG laser," *Appl. Phys. Lett.* **56**, 2390-2392 (1990).

[47] D. Herriott, H. Kogelnik, and R. Kompfner, *"Off-axis in spherical mirror interferometers," Appl. Opt.* **3**, 523-526 (1964).

[48] B. Perry, R. O. Brickman, A, Stein, E. B. Treacy, and P. Rabinowitz, "Controllable pulse compression in a multiple-pass-cell Raman laser," *Opt. Lett.* **5**, 288-290 (1980).

[49] H. A. Haus, *Waves and Fields in Optoelectronics*, Prentice-Hall, pp128, 1984.

[50] *Handbook of Chemistry and Physics*, 61st Ed., CRC Press, Inc. Boca Raton, FL, USA 1980.

[51] S. Tsuda, W. H. Knox, S. T. Cundiff, W. Y. Jan, and J. E. Cunningham, "Mode-locking of ultrafast solid-state lasers with saturable Bragg reflectors," *IEEE J. Sel. Top. in Quant, Electron.* **2**, 454-464 (1996).

[52] S. H. Cho, U. Morgner, F. X. Kärtner, J. G. Fujimoto, J. E. Cunningham, and W. H. Knox, "Generation of 90-nJ pulses with a 4-MHz repetition-rate Kerr-lens mode-locked Ti:Al_2O_3 laser operating with net positive and negative intracavity dispersion," *Opt. Lett.* **26**, 560-562 (2001).

[53] Hermann. A. Haus, "Gaussian pulse wings with passive modelocking," *Opt. Comm.* **97**, 215-218 (1993).

[54] Y. Chen, F. X. Kärtner, U. Morgner, S. H. Cho, H. A. Haus, E. P. Ippen, and J. G. Fujimoto, "Dispersion-managed mode locking," *J. Opt. Soc. Am. B* **16**, 1999-2004 (1999).

[55] Y. Chen and H. A. Haus, "Dispersion-managed solitons with net positive dispersion," *Opt. Lett.* **23**, 1013-1015 (1998); H. A. Haus and Y. Chen, "Dispersion-managed solitons as nonlinear Bloch waves," *J. Opt. Soc. Am. B* **16** 889-894 (1999).

[56] H. A. Haus, J. G. Fujimoto, and E. P. Ippen, "Structures for additive pulse modelocking," *J. Opt. Soc. Am. B* **8**, 2068-2076 (1991).

[57] P. Marcq, H. Chaté, and R. Conte, "Exact solutions of the one-dimensional quaintic complex Ginzburg-Landau equation," *Physica D* **73,** 305-317 (1994).

[58] J. M. Soto-Crespo, N. N. Akhemediev, V. V. Afanasjev, "Algebraic pulse-like solutions of the quintic complex Ginzburg-Landau equation," *Opt. Comm.* **118**, 587-593 (1995).

[59] A. R. Libertun, R. Shelton, H. C. Kapteyn, and M. M. Murnane, "A 36 nJ-15.5 MHz extended cavity Ti:Sapphire oscillator," in *Conference on Lasers and Electro-Optics*, OSA Technical digest Series, 469-470, 1999; A. Poppe, M. Lenzner, F. Krausz, and Ch. Spielmann, "A sub-10 fs, 2.5-MW Ti:sapphire oscillator," Technical Digest in *Ultrafast Optics*, 154-157, 1999.

[60] H. A Haus and W. S. Wong, "Solitons in optical communications," *Rev. Mod. Phys.* **68**, 423-444 (1996).

[61] M, von Allmen and A. Blatter, *Laser-beam interactions with materials*, 2^{th} Ed. Springer, NewYork, 1995.

[62] M. D. Perry, B. C. Stuart, P. S. Banks, M. D. Feit, V. Yanovsky, and A. M. Rubenchik, "Ultrashort-pulse laser machining of dielectric materials," *J. Appl. Phys.* **85**, 6803-6810 (1999).

[63] K. K. Thornber, "Applications of scaling to problems in high-field electronic transport," *J. Appl. Phys.* **52**, 279-290 (1981).

[64] A. Tien, S. Backus, H. Kapteyn, M. M. Murnane, and G. Mourou, "Short-pulse laser damage in transparent materials as a function of pulse duration," *Phys. Rev. Lett.* **82**, 3833-3836 (1999).

[65] M. Lenzner, J. Krüger, S. Sartania, Z. Cheng, Ch. Spielman, G. Mourou, W. Kautek, and F. Krausz, "Femtosecond optical breakdown in dielectrics," *Phys. Rev. Lett.* **80**, 4076-4079 (1998).

[66] D. Du, X. Liu, G. Korn, J. Squier, and G. Mourou, "Laser-induced breakdown by impact ionization in SiO_2 with pulse widths from 7 ns to 150 fs," *Appl. Phys. Lett.* **64**, 3071-3073 (1994).

[67] C. B. Schaffer, A. Brodeur, and E. Mazur, "Laser-induced breakdown and damage in bulk transparent materials induced by tightly focused femtosecond laser pulses," *Meas. Sci. Technol.* **12**, 1784-1794 (2001).

[68] D. von der Linde and H. Schüler, "Breakdown threshold and plasma formation in femtosecond laser-solid interaction," *J. Opt. Soc. Am.* ***B*** **13,** 216-222 (1996).

[69] J. H. Marburger, "Self-focusing:theory," *Prog. Quant. Electron.* **4**, 35-110 (1975).

[70] M. J. Soileau, W. E. Williams, N. Mansour and E. W. van Stryland, "Laser-induced damage and the role of self-focusing," *Opt. Eng.* **28**, 1133-1144 (1989).

[71] C. B. Schaffer, A. Brodeur, J. F. García, and E. Mazur, "Micromachining bulk glass by

use of femtosecond laser pulses with nanojoule energies," *Opt. Lett.* **26**, 93-95 (1999).

[72] Amnon Yariv, *Optical electronics*, 4th Ed., Saunders College publishing, Fort Worth, 1991.

[73] C. Florea, K. A. Winick, Y. Sikorski, A Said, and P. Bado, "Optical waveguide amplifier in Nd-doped glass written with near-IR femtosecond laser pulses," in *Conference on Lasers and Electro-Optics*, OSA Technical digest Series, 128-129, 2000.

[74] J. H. Stricker and W. W. Webb, "Three-dimensional optical data storage in refractive media by two-photon excitation," *Opt. Lett.* **16**, 1780-1782 (1991).

[75] Y. Kawata, H. Ishitobi, and S. Kawata, "Use of two photon absorption in a photorefractive crystal for three-dimensional optical memory," *Opt. Lett.* **23**, 756-758 (1998).

[76] Y. Sikorski, A. A. Said, P. Bado, R. Maynard, C. Florea, and K. A. Winick, "Optical waveguide amplifier in Nd-doped glass written with near-IR femtosecond laser pulses," *Elect. Lett.* **36**, 226-227 (2000).

[77] W. D. Laidig, N. Holonyak, Jr., M. D. Camras, K. Hess, J. J. Coleman, P. D. Dapkus, and J. Bardeen, "Disoder of an Al-GaAs superlattice by impurity diffusion," *Appl. Phys. Lett.* **38**, 776-778 (1981).

[78] A. S. Helmy, N. P. Johnson, M. L. Ke, A. C. Brice, J. S. Aitchison, J. H. Marsh, I. Gontijo, G. S. Buller, J. Davidson, and P. Dawson, "A study of impurity-free vacancy disordering in GaAs-AlGaAs for improved modeling," *IEEE Sel. Top. Quantum. Electron.* **4**, 661-668 (1998); A. S. Helmy, J. S. Aitchison,and J. H. Marsh, "The kinetics of intermixing of GaAs/AlGaAs quantum confined heterostructure," *Appl. Phys. Lett.* **71**, 2998-3000 (1997).

[79] E. J. Skogen, J. S. Barton, S. P. DenBaars, and L. A. Coldren, "A quantum-well-intermixing process for wavelength-agile photonic integrated circuits, *IEEE Sel. Top. Quantum. Electron.* **8**, 863-869 (2002).

[80] B. S. Ooi, C. J. Hamilton, K. McIlvaney, A. C. Bryce, R. M. De La Rue, J. H. Marsh, and J. S. Roberts, "Quantum-well intermixing in GaAs-AlGaAs structure using pulsed laser irradiation," *IEEE Photon. Technol. Lett.* **9**, 587-589 (1997).

[81] A. McKee, C. J. McLean, G. Lullo, A. C. Bryce, R. M. De La Rue, J. H. Marsh, and C. Button, "Monolithic integration in InGaAs/InGaAsP multiple-quantum-well structures using laser intermixing," *IEEE J. Quantum. Electron.* **33,** 45-55 (1997).

[82] C. J. McLean, A. Mckee, J. H. Marsh, and R. M. De La Rue, "Lateral control of the bandgap in GaInAs/GaInAsP MQW structured using photoabsorption-induced disordering," *Electron. Lett.* **29**, 1657-1658 (1993).

[83] J. E Epler, R. D. Burnhan, R. L. Thornton, T. L. Paoli, and M. C. Bashaw, "Laser induced disordering of GaAs-AlGaAs superlattice and incorporation of Si impurity," *Appl. Phys. Lett.* **49**, 1447-1449 (1986).

[84] J. Ralston, A. L. Moretti, R. K. Jain, and F. A. Chambers, "Intermixing of $Al_xGa_{1-x}As$/GaAs superlattice by pulsed laser irradiation," *Appl. Phys. Lett.* **50**, 1817-1819 (1987).

[85] B. C. Qiu, A. C. Bryce, R. M. De La Rue, and J. H. Marsh, "Monolithic integration in InGaAs-InGaAsP multiquantum-well structure using laser processing," *IEEE Photon. Technol. Lett.* **10**, 769-771 (1998).

[86] A. McKee, C. J. McLEan, A. C. Bryce, R. M. De La Rue, J. H. Marsh, and C. Button, "High quality wavelength tuned multiquantum well GaInAs/GaInAsP lasers fabricated using photoabsorption induced disordering," *Appl. Phys. Lett.* **65**, 2263-2265 (1994).

[87] C. J. McLean, A. McKee, G. Lullo, A. C. Bryce, R. M. De La Rue, and J. H. Marsh, "Quantum well intermixing with high spatial selectivity using a pulsed laser technology," *Electron. Lett.* **31**, 1285-1286 (1995).

[88] J. J. Dubowski, Y. Feng, P. L. Poole, M. Buchanan, and S. Poirier, "Monolithic multiple wavelength ridge waveguide laser array fabricated by Nd:YAG laser-induced quantum well intermixing," *J. Vac. Sci. Technol.* **20**, 1426-1429 (2002); J. J. Dubowski, S. Charbonneau, P. J. Poole, A. P. Roth, C. Lacelle, and M. Buchanan, "Laser writing of quantum well intermixed GaInAsP/InP microstructures," *SPIE* **3274**, 53 (1998).

[89] T. K. Ong, Y. C. Chan, Y. L. Lam, and B. S. Ooi, "Wavelength tuning in GaAs/InGaAsP quantum well lasers using pulsed-photoabsorption-induced disordering," *Appl. Phys. Lett.* **78**, 2637-2639 (2001).

[90] P. Abraham, J. Piprek, S. P. Denbaars, and J. E. Bowers, "Study of temperature effects on loss mechanism in 1.55 μm laser diodes with InGaP electron stopper layer," *Semicond. Sci. Technol.* **14**, 419-424 (1999).

[91] H. C. Casey Jr. and M. B. Panish, *Heterostructure lasers I*, Academic Press, London, UK. 1978.

[92] H. S. Carslaw and J. C. Jaeger, *Conduction of heat in solids*, Oxford University Press, Oxford, UK, 1959.

[93] W. W. Duley, *CO_2 Lasers*, Academic Press Inc., London, UK, 1976.

[94] Semiconductors on NSM, http://www.ioffe.rssi.ru/SVA/NSM/Semicond/index.html.

[95] P. Bhattacharya, *Properties of lattice-matched and strained Indium Gallium Arsenide*, IEE, INSPEC, London, UK, 1993.

[96] *Properties of Indium Phosphide*, IEE, INSPEC, London, UK, 1991.

[97] M. R. Brozel and G.E. Stillman, *Properties of Gallium Arsenide*, 3rd Ed., IEE, INSPEC, London, UK, 1996.

[98] Robert Hull, *Properties of crystalline Silicon*, IEE, INSPEC, London, UK, 1988.

[99] T. Nakayama, M Okigawa, and N. Itoh, "Laser-induced sputtering of oxides and com-

pound semiconductors," *Instruments & Methods in Physics Research B*, 301-306 (1984).

[100] J. M. Moison and M. Bensoussan, "Laser-induced surface reconstruction of semiconductors and metals," *Surf. Sci.* **126** 294-300 (1983).

[101] A. Sakouri, Bin Liu, and J. E. Bowers, “Fused photonic integrated circuits for optical switching,” in Photonics in switching, *OSA trends in optics and photonics series*, 168-169, 2000.

[102] P. V. Studentkov, M. R. Gokhale, and S. R. Forrest, “Efficient coupling in integrated twin-waveguide lasers using waveguide tapers,” *IEEE Photon. Tech. Lett.* **11**, 1096-1198 (1999).

[103] C. R. Doerr, C. H. Joyner, L. W. Stulz, and J. Gripp, “Multifrequency laser having integrated amplified output coupler for high-extinction-ratio modulation with single-mode behavior,” *IEEE Photon. Tech. Lett.* **10**, 1374-1376 (1998).

[104] E. J. Skogen, J. S. Barton, S. P DenBaars, and L. A. Coldren, “Tunable sampled-grating DBR lasers using quantum-well intermixing,” *IEEE Photon. Tech. Lett.* **14**, 1243-1245 (2002).

[105] F. Mederer, R. Jäger, H. J. Unold, R. Michalzik, K. J. Eberling, S. Lehmacher, A. Neyer, and E. Griese, “3-Gb/s data transmission with GaAs VCSELs over PCB integrated polymer waveguides,” *IEEE Photon. Tech. Lett.* **13**, 1032-1034 (2001).

[106] J. P. Hohimer and G. A. Vawter, “Passive mode-locking of monolithic semiconductor ring lasers at 86 GHz,” *App. Phys. Lett.* **62**, 1185-1187 (1993).

[107] B. E. Little, S. T. Chu, H. A. Haus, J. Foresi, and J. -P Laine, “Microring resonator channel dropping filters,” *J. Lightwave. Technol.* **15**, 998-1005 (1995).

[108] T. A. Ibrahim, V. Van, and P. –T. Ho, “All-optical time-division demultiplexing and spatial pulse routing with GaAs/AlGaAs microring resonator,” *Opt. Lett.* **27**, 803-805 (2002).

[109] P. B. Hansen, G. Raybon, M.-D. Chien, U. Koren, B. I. Miller, M. G. Young, J.-M. Verdiell, and C. A. Burrus, “A 1.54-um monolithic semiconductor ring laser: CW and mode-locked operation,” *IEEE Photon. Tech. Lett.* **4**, 411-413 (1991).

[110] S. Yu, T. F. Krauss, and P. J. R. Laybourn, “Mode locking in large monolithic semiconductor ring lasers,” *Opt. Eng.* **37**, 1164-1168 (1998).

[111] H. Han, D. V. Forber, and J. J. Coleman, “InGaAs-AlGaAs-GaAs strained layer quantum-well heterostructure square ring lasers,” *IEEE J. Quantum. Electron.* **31**, 1994-1997 (1995).

[112] Z. J. Fang, G. M. Smith, D. V. Forbes, and J. J. Coleman,” An InGaAs-GaAs strained layer single quantum-well ring laser with a reactive ion-etched tetragonal cavity,” *IEEE J. Quantum. Electron.* **31**, 44-48 (1995).

[113] M. F. Booth, A. Schremer, and J. M Ballantyne, "Spatial beam switching and bistability in a diode ring laser," *Appl. Phys. Lett.* **76**, 1095-1097 (2000).

[114] T. F. Krauss, R. M. De La Rue, and P. J. R. Laybourn, "Impact of output coupler configuration on operating characteristics of semiconductor ring lasers," *J. Lightwave. Technol.* **13**, 1500-1506 (1995).

[115] R. van Roijen, E. C. M. Pennings, M. J. N. van Stalen, T. van Dongen, B. H. Berbeek, and J. M. M. van der Heijden, "Compact InP-based ring lasers employing multimode interference couplers and combiners," *App. Phys. Lett.* **64**, 1753-1755 (1994).

[116] G. Grieffel, J. H. Abeles, R. J. Menna, A. M. Braun, J. C. Connolly, and M. King, "Low-threshold InGaAs ring lasers fabricated using bi-level dry etching," *IEEE Photon. Tech. Lett.* **12**, 146-148 (2000).

[117] K. Djordiev, S. J. Choi, S. J. Choi, and P. D. Dapkus, "Vertically coupled InP microdisk switching devices with electroabsorptive active regions," *IEEE Photon. Tech. Lett.* **14**, 1115-1117 (2002).

[118] S. Oku, M. Okayasu, and M. Ikeda, "Control of unidirectional oscillation in semiconductor orbiter lasers," *IEEE Photon. Tech. Lett.* **3**, 1066-1068 (1991).

[119] J. J. Liang, S. T. Lau, M. H. Leary, and J. M. Ballantyne, "Unidirectional operation of waveguide diode ring lasers," *App. Phys. Lett.* **70**, 1192-1194 (1997).

[120] S. H. Cho and R. J. Ram, "High counter-mode suppression-ratio semiconductor ring lasers," in Integrated Photonics Research, OSA, Vancouver, Canada, 2002; S. -H. Cho and R. J. Ram, "Unidirectionality of semiconductor ring lasers: Theory and experiment," in *18th IEEE International semiconductor laser conference*, Garmisch, Germany, 2002.

[121] M. Sorel, P. J. R. Laybourn, G. Giuliani, and S. Donati, "Unidirectional bistability in semiconductor waveguide ring lasers," *App. Phys. Lett.* **80**, 3051-3053 (2002).

[122] F. R. Foxvog, "Modes of a unidirectional ring laser," *Opt. Lett.* **5**, 285-287 (1980).

[123] W. S. Pelouch, P. E. Powers, and C. L. Tang, "Self-starting mode-locked ring-cavity Ti:sapphire laser," *Opt. Lett.* **17**, 1581-1583 (1992).

[124] A. Barlels, T. Dekorsy, and H. Kurz, "Femtosecond Ti:sapphire ring laser with a 2-GHz repetition rate and it's application in time-resolved spectroscopy," *Opt. Lett.* **24**, 996-998 (1999).

[125] E. Winter and E. P. Ippen, "Nonlinear carrier dynamics in $Ga_xIn_{1-x}As_yP_{1-y}$ compounds," *Appl. Phys. Lett.* **44**, 999-1001 (1984).

[126] S. Wang, H. K. Choi, and I. H. A. Fattah, "Studies of semiconductor lasers of the interferometric and ring types," *IEEE J. Quantum. Electron.* **18**, 610-617 (1982).

[127] R. h. Rediker and F. J. Leonberger, "Analysis of integrated-optics near 3dB coupler and Mach-Zehnder interferometric modulator using four-port scattering matrix," *IEEE J.*

Quantum. Electron. **18**, 1813-1816 (1982).

[128] L. F. Stokes, M. Chodorow, and H. J. Shaw, "All-single-mode fiber resonator," *Opt. Lett.* **7**, 288-290 (1982).

[129] A. L. Fetter and J. D. Walecka, *Quantum theory of many-particle systems*, New York, NY: McGraw-Hill, 1997.